MICROFLUIDIC PLATFORMS FOR HEMORHEOLOGY AND COAGULATION TIME ANALYSIS

A DISSERTATION SUBMITTED TO
THE GRADUATE SCHOOL OF ENGINEERING AND SCIENCE
OF BILKENT UNIVERSITY
IN PARTIAL FULFILLMENT OF THE REQUIREMENTS FOR
THE DEGREE OF
DOCTOR OF PHILOSOPHY
IN
MATERIALS SCIENCE AND NANOTECHNOLOGY

By
Ziya Işıksaçan
January 2020

MICROFLUIDIC PLATFORMS FOR HEMORHEOLOGY AND COAGULATION TIME ANALYSIS

By Ziya Işıksaçan

January 2020

We certify that we have read this dissertation and that in our opinion it is fully adequate, in scope and in quality, as a dissertation for the degree of Doctor of Philosophy.

Çağlar Elbüken(Advisor)

Bülend Ortaç

Hamza Kurt

Mehmet Selim Hanay

Kıvanç Azgın

Approved for the Graduate School of Engineering and Science:

Ezhan Karaşan
Director of the Graduate School

ABSTRACT

MICROFLUIDIC PLATFORMS FOR HEMORHEOLOGY AND COAGULATION TIME ANALYSIS

Ziya Işıksaçan
Ph.D. in Materials Science and Nanotechnology
Advisor: Çağlar Elbüken
January 2020

Blood is a non-Newtonian fluid consisting of plasma and cells that uninterruptedly circulate the body. Erythrocytes are deformable anucleated discoid blood cells with a viscoelastic membrane, constituting around half of blood volume. Hemorheology investigates blood flow characteristics determined by hemorheological properties comprising aggregation, sedimentation, and deformation of erythrocytes as well as blood/plasma viscoelasticity. These hemorheological properties are intricately interdependent. Hence, acquired or hereditary disorders affecting one hemorheological property (malaria, diabetes, anemia) lead to alterations in other properties. Available techniques lack the ability to measure these properties all-at-once and in physiologically relevant conditions. Blood coagulation is as essential as a healthy blood flow. This is a body defense mechanism involving the interplay of blood constituents for stable clot formation to stop bleeding. Sensitive and periodic measurement of coagulation time is critical for individuals who are under the risk of excessive bleeding or thrombus-originated vessel obstruction. Today, these conditions are responsible for 25 percent of all deaths worldwide. Unfortunately, the conventional practice for coagulation monitoring is fixed-interval hospital visits by patients.

In this thesis, we present novel microfluidic platforms and measurement methods for the analysis of hemorheological properties and coagulation time parameters. The assays are based on optical quantification of erythrocyte dynamics inside miniaturized channels. The measurements require only 50 μl undiluted blood and are completed in less than 5 min. Firstly, we demonstrate optical measurement of erythrocyte aggregation and rapid measurement of erythrocyte sedimentation rate (ESR) using aggregation dynamics. Secondly, we present the

results of clinical ESR tests performed in a local hospital and compare the performance of the developed platform with the conventional 1-hour test. Simultaneously obtained optical transmission signals and real-time microscopic observations of erythrocytes in custom-developed cartridges validate the proposed measurement principle. Thirdly, we present a method offering a holistic approach to blood flow characterization. The method enables simultaneous analysis of multiple hemorheological properties by optically investigating collective erythrocyte dynamics, primarily deformation, in a channel during unique damped oscillatory sample motion. We create a fluidic environment mimicking in vivo flow: confined, directional, and pulsatile movement of blood at flow rates and hematocrit comparable to physiological levels. Fourthly, we present a method for blood coagulation time measurement by optical quantification of erythrocyte aggregation. We demonstrate the fundamental relationship between aggregation and coagulation. Finally, we present an alternative, entirely disposable microfluidic platform for hemorheology and coagulation time analysis based on migration analysis of blood sample in microfluidic channels. Overall, the microfluidic platforms and measurement methods presented here will potentially initiate routine hemorheological and coagulation time analysis even in resource-poor setting.

Keywords: Erythrocyte, Red blood cell, Blood, Microfluidics, Hemorheology, Coagulation.

ÖZET

HEMOREOLOJİ VE PIHTILAŞMA ZAMANI ANALİZİ İÇİN MİKROAKIŞKAN PLATFORMLAR

Ziya Işıksaçan
Malzeme Bilimi ve Nanoteknoloji, Doktora
Tez Danışmanı: Çağlar Elbüken
Ocak 2020

Kan, vücudu sürekli olarak dolaşan plazma ve hücrelerden oluşan non-Newtonian bir sıvıdır. Eritrositler, viskoelastik zara sahip, deforme olabilen, çekirdeksiz, disk şeklinde ve kanın hacimsel olarak yarısını oluşturan kan hücreleridir. Hemoreoloji, kanın akış karakteristiğini inceler. Bu karakteristiği belirleyen hemoreolojik özellikler, eritrositlerin topaklanması, çökelmesi ve deformasyonuyla birlikte kan/plazma viskoelastikiyetidir. Hemoreolojik özellikler karmaşık şekilde birbirlerine bağlıdırlar. Bu yüzden, hemoreolojik özelliklerden birini etkileyen, sonradan edinilen veya kalıtsal sorunlar (sıtma, diyabet, anemi) diğer özelliklerde de değişime neden olur. Mevcut teknikler, bu özellikleri eş zamanlı ve vücuda benzer şartlar altında ölçme konusunda yetersizdirler. Kanın pıhtılaşması, sağlıklı bir kan akışı kadar öneme sahiptir. Pıhtılaşma, kan elemanlarının etkinliğiyle kan kaybını önlemek amacıyla kararlı pıhtı yapısı oluşturan bir vücut savunma mekanizmasıdır. Pıhtılaşma zamanının hassas ve periyodik ölçümü, kan kaybı ve damar tıkanıklığı riski olan bireyler için kritik bir öneme sahiptir. Günümüzde bu durumlar, dünya nüfusunun yüzde 25'inin ölümünden sorumludur. Maalesef, geleneksel uygulama, hastaların belirli aralıklarla hastane ziyaretiyle pıhtılaşma değerlerini izletmesidir.

Bu tezde, hemoreolojik özelliklerin ve pıhtılaşma zamanı parametrelerinin analizi için yeni mikroakışkan platformlar ve ölçüm yöntemleri sunuyoruz. Testler, eritrositlerin küçük kanallar içerisinde optiksel ölçümü temellidir. Ölçümlerde sadece 50 μl kana ihtiyaç vardır ve toplam ölçüm süresi 5 dakikadan daha azdır. İlk olarak, eritrosit topaklanmasının ve topaklanma dinağini kullanarak eritrosit çökelme oranının (sedim) optiksel ölçümünü gösteriyoruz. İkinci olarak, hastanede yaptığımız sedim ölçüm sonuçlarını veriyoruz ve geliştirilen platform ile geleneksel ölçümün performanslarını karşılaştırıyoruz. Optiksel transmisyon sinyalleri ile eş zamanlı olarak eritrositlerin mikroskop altında gerçek zamanlı gözlenmesi, önerdiğimiz ölçüm yöntemini doğrulamaktadır. Üçüncü olarak,

kan akış karakterizasyonuna bütüncül bir yaklaşım sunan bir yöntem sunuyoruz. Bu yöntem, birkaç hemoreolojik özelliğin eş zamanlı ölçümünü mümkün kılmaktadır. Bunu, örneğin bir kanal içerisinde sönümlenen salınımlı hareketi esnasında, eritrositlerin toplu hareketlerini optiksel olarak analiz ederek yapıyoruz. Vücut içerisindeki akışa benzer bir akış ortamı oluşturuyoruz. Dördüncü olarak, eritrosit topaklanmasının optiksel olarak incelenmesiyle pıhtılaşma zamanının elde edildiği bir yöntem sunuyoruz. Pıhtılaşma ve eritrosit topaklanması mekanizmalarının temel bağlantısını ortaya çıkartıyoruz. Son olarak, örneğin mikroakışkan kanallar içerisinde aldığı mesafeyi inceleyerek hemoreoloji ve pıhtılaşma analizi yapabilen alternatif, tek kullanımlık bir mikroakışkan platform sunuyoruz. Sonuç olarak, burada gösterdiğimiz platformlar ve ölçüm yöntemleri, hemoreoloji ve pıhtılaşma zamanı analizlerinin, kaynak sıkıntısı çeken bölgelerde bile yapılabilmesini mümkün kılma potansiyeline sahiptir.

Anahtar sözcükler: Eritrosit, Kırmızı kan hücresi, Mikroakışkan, Hemoreoloji, Pıhtılaşma.

Acknowledgement

Yunus Emre emphasizes love by saying “let us be lovers and loved ones; the earth shall be left to no one”. This humble piece of work is the product of such a love – the one that I constantly receive from the dear people around me.

I met Prof. Çağlar Elbüken first back in 2012 at Koç University, and since then, he has become an excellent mentor, role-model, and life-long friend for me. Not only has he helped me improve myself academically, but also supported me wisely at every aspect of life. I would like to thank him for being my Ph.D. advisor, confidently giving me the responsibility of such a promising project, and providing me with an intellectual environment. I am deeply indebted to him for his patience, understanding, and guidance. I would also like to thank his parents Zehra-İbrahim Elbüken with whom I am fortunate to spend time.

I was very lucky to have Dr. M. Tahsin Güler and Dr. İsmail Bilican around me. They are the funniest people I have ever met. I will never forget our Izmir trip.

Dr. Murat Serhatlıoğlu, Dr. Talha Masood Khan, and Dr. Ali Haider have become my closest friends who made Ankara a more liveable place for me. We have shared many unforgettable moments and had fruitful conversations.

A research lab is indeed a peaceful home if you have colleagues like Ali Kalantarifard, Mohammed Asghari, Abtin Saateh, Dr. Elnaz Alizadeh Haghighi, Resul Sarıtaş, and Dr. Pınar Beyazkılıç who were very polite, supportive, friendly to me. I have the same feelings for Dr. Hasan Güner, Bartu Şimşek, Yakup Midilli, Lütfiye Hallıoğlu, Dr. Nuray Gündüz, Nurcan Hastar, Prof. Engin Durgun, and Dr. Petro Deminskyi.

I am grateful to Prof. Özcan Erel for opening the doors of his lab. He was more than a collaborator for me with his knowledge, modesty, hospitality, and public spirit. I thank Dr. Amir Hossein Raffiee and Dr. Daiki Matsunaga for our scientific discussions. I am grateful to Dr. Remzi Özgür Özer and Dr. Çağla Şeşen for their friendly helps.

I would like to thank the thesis jury members Prof. Bülend Ortaç, Prof. Hamza Kurt, Prof. M. Selim Hanay, and Prof. Kıvanç Azgın to support my thesis with their invaluable comments and suggestions. I thank staff at UNAM, Yıldırım

Beyazıt University Biochemistry Lab, and Bayındır Söğütözü Hospital. I owe thanks to Prof. İhsan Doğramacı, Prof. Salim Çıracı, Prof. Mehmet Bayındır, and Prof. H. Volkan Demir for their tremendous contributions to the Bilkent community and UNAM.

I would like to acknowledge ASELSAN for the ASELSAN Graduate Scholarship for Turkish Academicians. I feel fortunate to have Prof. Mustafa Yorulmaz as my scholarship advisor.

I am grateful to Prof. Oğuz Başkurt who was a pioneer in the field of hemorheology. His books and articles have been very helpful for me.

Education is a long process. I express my gratitude to my teachers at Kardelen School, Nevşehir Science High School, Koç University, Edinburgh University, and Bilkent University including Prof. İrşadi Aksun, Prof. Varga Kalantarov, Prof. Adam A. Stokes, Prof. Anthony Walton, Prof. Yifan Li, Prof. Colin Campbell, Alparslan Aydar, Gökhan Metin, Mustafa Usta, and Mehmet Alper.

Family is everything.

Whatever I have achieved in life, it is all thanks to my parents Nilgün-Ali Işıksaçan who give me endless love and support. They deserve the best. I thank my brothers Mehmet Akif and Salih for being so nice and close to me. I have always tried to do the righteous deeds to be a role model for them. I hope I am doing well.

I cannot underestimate the contributions of my grandparents Saliha-Ziya Işıksaçan and Mükerrem-Ercan Ekmekçioğlu. I am privileged to live with and learn from them. I lost my grandfather Ziya in the third year of my Ph.D. studies. I wish he could witness this small step forward. May he rest in peace.

I express warmest thanks to my mother-, father-, and brothers-in-law for accepting me to their fun family.

Last but not least, I owe infinite thanks and gratitude to my lovely wife Hazal for beautifying my life. Her smiles are the most precious treasure on earth. Her existence has brought me an endless spring and colorful flowers.

"If you can fill the unforgiving minute with sixty seconds' worth of distance run, yours is the Earth and everything that is in it; And–which is more–you'll be a Man, my son!" Rudyard Kipling

dedicated to my wife, mum, dad, brothers, and advisor

Contents

1 Introduction **1**

1.1 Microfludics 1
1.2 Microfluidic Platforms 4
1.3 Physics of Microfluidics 8
1.4 Blood Circulation 11
1.5 Erythrocytes 13
1.6 Blood Rheology 15
1.7 Viscoelasticity 18
1.8 Optics Concepts 21
1.9 Thesis Outline 23

2 Erythrocyte aggregation and sedimentation rate measurement using dextran-mediated blood **26**

2.1 Introduction 27
2.2 Experimental 28
2.2.1 Sample Preparation 28
2.2.2 Particle Sedimentation Theory 29
2.2.3 Microfluidic Cartridge Fabrication 30
2.2.4 Measurement Platform 31
2.3 Results and Discussion 35
2.3.1 EA and ESR Measurement using Dextran-mediated Blood 35
2.3.2 Effect of Measurement Conditions 39
2.3.3 Effect of Shear Rate on Erythrocyte Disaggregation 41
2.4 Conclusion 45

3 Clinical erythrocyte sedimentation rate measurement from erythrocyte aggregation 47
3.1 Introduction . . . 48
3.2 Experimental . . . 50
3.2.1 Sample Preparation . . . 50
3.2.2 Microfluidic Cartridge Fabrication . . . 50
3.2.3 Measurement Platform . . . 52
3.3 Results and Discussion . . . 54
3.3.1 Quantifying the Aggregation of Erythrocyte . . . 54
3.3.2 ESR Measurement with the Microfluidic Platform . . . 55
3.3.3 Precision and Repeatability . . . 57
3.3.4 Simultaneous ESR Measurement and EA Monitoring . . . 59
3.4 Conclusion . . . 63

4 Determination of hemorheological properties using erythrocyte movements in a channel under damped oscillatory flow 64
4.1 Introduction . . . 65
4.2 Experimental . . . 67
4.2.1 Materials and Characterization . . . 67
4.2.2 Measurement Platform . . . 69
4.3 Results and Discussion . . . 70
4.3.1 Optical Analysis of Collective Erythrocyte Movements in a Fluidic Channel . . . 70
4.3.2 Change in Medium Properties . . . 74
4.3.3 Change in Erythrocyte Membrane Stiffness . . . 78
4.4 Conclusion . . . 79

5 Coagulation time measurement from erythrocyte aggregation 81
5.1 Introduction . . . 82
5.2 Experimental . . . 85
5.2.1 Sample Preparation . . . 85
5.2.2 Cartridge Fabrication and Measurement Platform . . . 86
5.3 Results and Discussion . . . 87
5.3.1 Optical Analysis of Erythrocyte Aggregation . . . 87

5.3.2 Role of Fibrinogen in Coagulation and Aggregation 89
5.3.3 Comparative Coagulation Time Measurements 92
5.3.4 Simultaneous Optical Measurement and Microscopic Observation 94
5.4 Conclusion 96

6 Low-cost approach to prothrombin time measurement 97
6.1 Introduction 98
6.2 Experimental 101
6.2.1 Sample Preparation 101
6.2.2 Cartridge Fabrication 101
6.2.3 Effervescent Pump Fabrication 102
6.2.4 Measurement Platform 104
6.3 Results and Discussion 108
6.3.1 Effervescent Pump Characterization 108
6.3.2 Quantitative Distance Measurement 110
6.3.3 Comparative Prothrombin Time Tests 112
6.3.4 Personal Prothrombin Time Measurement 114
6.4 Conclusion 116

7 Conclusion and Future Directions 118
7.1 Concluding Remarks 118
7.2 Future Directions 119

A Estimating Relaxation Time for Suspending Mediums 145

B Publication List 147

List of Figures

1.1 An examplary PDMS-on-glass microfluidic device 3
1.2 Parabolic flow profile 9
1.3 Pressure and velocity distribution in vessels with different diameters 12
1.4 Blood components 13
1.5 Erythrocytes and membrane proteins 14
1.6 Viscosity of blood and plasma as a function of shear rate 16
1.7 Schematic of blood flow in a vessel network 17
1.8 Maxwell and Kelvin-Voigt models of viscoelastic materials 19
1.9 Creep-recovery response of viscous, elastic, and viscoelastic materials 21
1.10 Molar extinction coefficients for oxy- and deoxy- hemoglobin . . . 23

2.1 Comparison of ESR depending on erythrocyte aggregability . . . 30
2.2 Top-view photography of the analyzer 32
2.3 Side-view photography of the analyzer 33
2.4 Schematic representation of the platform 33
2.5 Schematic representation of the platform 34
2.6 Transmission spectrum of whole blood 34
2.7 Blood samples with different dextran concentrations tested with the microfluidic system 36
2.8 Hematocrit tubes filled with different blood samples for ESR analysis 37
2.9 Comparison of the conventional ESR measurement and the microfluidic measurement 38
2.10 Investigation of the effect of vibration on the optical measurements 41
2.11 Finite element model results showing the shear rate distributions applied to erythrocytes in the channels 44

2.12 Visual observation of erythrocytes just after the pinch valves stopped operating 45

3.1 Photography of the platform 53
3.2 Aggregation indices calculated for the ESR measurement 55
3.3 Comparison of the microfluidic system test results with the gold standard Westergren method 56
3.4 Precision tests for the microfluidic system 58
3.5 Repeatability performance of the microfluidic system 59
3.6 Schematic representation of the cartridge and simultaneous measurement method 60
3.7 Simultaneous ESR measurement and EA monitoring with the microfluidic system 61

4.1 Suspending medium viscosity measured by the rotational rheometer 68
4.2 Characterization of pump pressure and optical signal during flow . 71
4.3 Customized microscopy setup to get side-view video recording . . 72
4.4 Effect of suspending medium viscoelasticity on optical transmission signals for healthy erythrocytes 75
4.5 Comparing optical signal amplitudes to medium properties 77
4.6 Effect of suspending medium viscoelasticity on optical transmission signals for stiffened erythrocytes 78
4.7 Comparing optical signal amplitudes of an H-sample and S-sample at a fixed medium property 79

5.1 Coagulation cascade 83
5.2 Channel with constriction regions 87
5.3 Measurement of the transmitted signal intensity without an activator reagent and with PT reagent 88
5.4 The role of fibrinogen in coagulation and aggregation 91
5.5 The employment of dextran to facilitate the aggregation process . 92
5.6 Comparison of the platform with the conventional equipment for PT measurement 93
5.7 Simultaneous optical measurement and microscopic observation . 95

6.1 Schematic drawing of the effervescent pump layers and their assembly 103
6.2 Schematic representation and photograph of the device 105
6.3 Schematic representation of the device and the channels during test 107
6.4 Characterization of the effervescent pump 110
6.5 Grid design for quantitative distance measurement 112
6.6 Comparing the device with the conventional benchtop PT analyzer for PT measurement 113
6.7 Photograph of the device after the PT measurement 115

B.1 Lab on a Chip cover 148

List of Tables

1.1 Values of cross-sectional area, flow velocity, and Reynolds number for different vessel types. 12

4.1 Summary of the rheological properties (η: viscosity and λ: relaxation time) of the suspending mediums. 67

Chapter 1

Introduction

In this chapter, a general background and overview of the main contents of the thesis are provided. First of all, an introduction to microfluidics, microfluidic platforms in the literature, and theoretical basis of microfluidics are reported. This is followed by brief explanations of blood circulation, erythrocytes, blood flow characteristics, optics concepts and viscoelasticity. Finally, the outline of the rest of the thesis is given.

A portion of the content of this chapter was published in [1] as;

Z. Isiksacan, M. T. Guler, A. Kalantarifard, M. Asghari, and C. Elbuken, Lab-on-a-chip platforms for disease detection and diagnosis, Biosensors and Nanotechnology: Applications in Health Care Diagnostics, pp. 155-181, 2018.

1.1 Microfludics

The roots of understanding liquid behaviors date back to centuries ago. Initial examples cover the studies by Hippocrates (400 BC) and Galen (200 AD) who performed colorimetric analysis of body fluids like urine to monitor human physiology [2]. The adaptation of silicon electronics fabrication technologies to

other materials such as glass or polymers led to the birth of microfluidic systems. These systems allow investigation and control of fluids at micrometer scale under mostly laminar flow conditions in contrast to macroscale flow like that of rivers where turbulence is observed. Due to the wide variety of applications of microfluidics, several research groups have been involved in the development of basic microfluidic components. With advancement of microfabrication methods and tools, dexterous handling of liquids in small quantities and development of small fluidic components (valves, pumps, etc.) were witnessed after 1950s. Seminal studies include the development of miniaturized gas chromatography chip [3] and ink-jet printing technology [4]. In 1990, Andreas Manz proposed the concept of the micro total analysis systems (μTAS), addressing the possibility that miniaturized integrated systems can be developed to perform biochemical analysis with much lower sample volumes [5]. Then, microfluidics has emerged as a discipline where very low volumes of fluids are manipulated and studied, employing structures in micron length scales. Conventional photolithographic techniques used for silicon and glass wafers in microelectronics and MEMS have been inherited for the fabrication of microfluidic chips.

PDMS, polydimethylsiloxane, was utilized by George Whitesides for soft lithography introducing rapid fabrication of microfluidic devices [6]. Years of research have shown that this elastomeric, optically transparent, porous, and biocompatible material is suitable for many microfluidic applications. Overall, replica molding, 3D printing, imprint lithography, and micro injection molding are the most popular fabrication techniques [7]. Among all, injection molding stands ahead in terms of automation and high-throughput [8]. In this process, a liquid thermoplastic material such as polycarbonate is poured in a CNC-milled metal mold and cooled down to form the device.

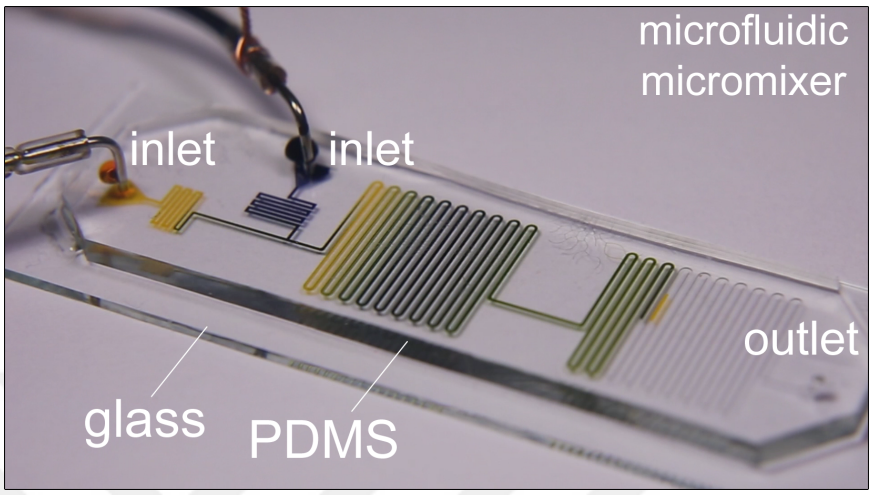


Figure 1.1: An examplary PDMS-on-glass microfluidic device for mixing of two fluids along the channel.

The utmost goal of μTAS is to integrate laboratory tasks on a single chip, namely lab-on-a-chip (LOC). Engineering of microfluidic systems has led to lab-on-a-chip (LOC) systems that can be used for biomedical applications whether at the point-of-care as portable systems or at clinical settings as advanced detection systems. The increasing awareness on personalized treatments proves the importance of such democratizing technologies. The LOC systems, once successfully established, have the benefits of cost, automation, high throughput, multiplexing and portability. It is also critical to minimize the number of off-chip components such as power sources and pumps to turn microfluidic systems into truly LOC systems. This distinction is especially noteworthy for biomedical diagnostics and monitoring at the point of care (POC) as outlined in the ASSURED criteria proposed by the World Health Organization (WHO) [9, 10]. The acronym stands for "Affordable, Sensitive, Specific, User-friendly, Rapid and robust, Equipment free, and Deliverable to end-user". The increasing market share of microfluidic platforms in nearly all sectors is an indication of, hopefully, the bright future of lab-on-a-chip systems. Various bodily fluids such as blood, urine, or saliva can be used to look for specific biomarkers. The most commonly investigated biomarkers include proteins (especially for immunoassays), cells (erythrocytes, circulating tumor cells, platelets, etc.), nucleic acids (DNA, RNA, etc.), metabolites (glucose,

lactate, etc.), and ionic chemicals (sodium, potassium, etc.) [11]. Depending on the type of biomarker as well as the working mechanism of the platform, a number of detection principles can be proposed. The most preferred ones include optical detection (colorimetric, spectroscopic, plasmonic, fluorescence) and electrical detection (electrochemical, piezoelectric, impedimetric, potentiometric). The microfluidic platforms are conventionally categorized into five groups: continuous flow, paper-based, microdroplets, compact disk-based, and wearable platforms.

1.2 Microfluidic Platforms

Continuous flow microfluidic platforms are the conventional microfluidic diagnostic systems where single phase fluid flow is controlled inside microfluidic channels. The initial examples of continuous flow systems were fabricated on glass using conventional microfabrication techniques. The patterned glass layer is bonded with another glass piece forming micrometer scale delicate structures. After the adaptation of polymers, mostly PDMS, by the microfluidics community, the field witnessed an explosion of research output all across the world. The integrated platforms require on-chip pumps, valves, mixers, and sensors [12–16]. With the wide use of PDMS in microfluidics community, the number of continuous flow diagnostic microfluidic systems has inflated. A cornerstone for PDMS related devices was the development of elastomeric valve. Later, these microvalves have been integrated on a single device at a highly scalable level which led to very-large-scale integrated valve based PDMS microfluidic devices [17]. The continuous microfluidic platforms also resulted in several commercial products for disease diagnosis which are remarkable success stories in the field. One of the earliest examples of such systems is Agilent's on-chip gel capillary electrophoresis system. The system is composed of a benchtop analyzer unit and single use cartridges for DNA, RNA, and protein studies [18]. The system works with 1-5 μl of samples and dramatically reduces the sample and reagent consumption. Another seminal example of continuous microfluidic platforms is i-STAT whole blood analysis system. This handheld unit provides a platform for measurement of blood gases, electrolytes, cardiac markers, and coagulation factors in whole blood. The

disposable cartridges require only a drop of whole blood and perform amperometric/potentiometric measurement using microfabricated electrodes fabricated on silicon chips and integrated with polymer microfluidic channels. The latest generation of i-STAT's cartridges performs ELISA assays on cartridges containing washing/labeling fluids, which proves a very strong platform for detection of biomarkers for rapid diagnosis of myocardial infarction.

The intrinsic properties of paper make it a unique choice for microfluidic platforms designed for diagnosis. Paper is composed of entangled cellulose fibers forming a porous structure which makes it hydrophilic. By capillary force, paper can be used as a transport medium without any external power source. Besides, paper is ubiquitous, cheap, biodegradable, lightweight, and can be modified by chemicals, thus suits well for biomedical applications and diagnosis [19–24]. Paper-based platforms have existed even long before the birth of microfluidics due to the availability and remarkable benefits of paper. In order to control the fluid flow along paper, one needs to define channels on the paper. Development of hydrophobic regions on paper with paraffin and wax to obstruct fluid flow is not a new method and patented a century ago [25]. It is difficult to spot the earliest functional paper-based diagnostic device due to the lack of records. Yagoda's work in 1937 stands out since it demonstrates patterning of selected areas on paper using a paraffin stamping method [26]. Conventional paper-based devices are categorized as dipstick and lateral flow devices. The first examples of dipstick paper detection devices were developed by a French chemist, named Jules Maunmené, in 1850 for urine analysis. In order to measure pH of the blood, test strips were introduced in the 1920s and are still in the market. The introduction of lateral flow strips turned the simple dipstick assays into sample-in-result-out paper-based integrated devices that can perform ELISA tests. Recently, paper-based platforms have gained a momentum with the advancements in the field of microfluidics [27]. Democratization of diagnostic platforms is an increasing need all across the world, which constraints the complexity of microfluidic components on a single device when cost per test is a major concern. Therefore, researchers moved to paper-based devices, and the field has experienced the resurrection

of 100 year-old paper-based systems with advanced functionalities. The developments in low-cost microfabrication, printing methods, microelectronics, and microfluidics opened new avenues for paper-based platforms that allow high scale integration with improved sensitivity and multiplexing [27].

Droplet-based platforms are based on the generation and control of minute volumes of microdroplets (dispersed phase) within carrier liquids (continuous phase) inside microchannels. Individual droplets with low volumes allow very precise control over the concentration of the samples of interest as well as the reaction times. In addition, rapid and extremely repeatable generation of monodisperse droplets makes these systems suitable for high-throughput biochemical applications [28, 29]. Basic microfluidic operations that can be carried out using these platforms include transporting, splitting, and mixing of the droplet contents. In addition to the basic operations, manipulations that change the phase of the droplets can be performed. Some examples include chemical polymerization [30], cell / protein / DNA encapsulation [31, 32], and particle synthesis [33].

Compact Disc (CD) based microfluidic systems function based on the rotational motion of CD that creates an outward centrifugal force. Also known as lab-on-a-disc systems, they benefit from the absence of pumps, bubble-free liquid motion, elimination of residual volume, and ease of parallelization [34, 35]. These systems are composed of microfluidic CDs that house the fluids and a CD-player-like device that regulates the centrifugal force by controlling the rotation rate (rpm). The channels are mostly constructed using transparent plastics that enables optical detection using a hardware that is similar to the read-out units of CD-players [36]. The sample is introduced to the center of the CD and carried axially outward using centrifugal force. Not too surprisingly, optical detection is the most commonly used detection mechanism for CD-based LOC systems.

Wearable microfluidic platforms have received growing interest from both academia and industry due to their capacity for reliable health monitoring of wearers. They enable us to obtain information regarding an individual's state of health in a real-time, continuous, and non-invasive manner [37]. Thus, what is

aimed is an increase in the quality of life as well as reduction in medical costs associated with diagnostics and therapy [38, 39]. The detection principle is mostly based on electrochemical sensing that provides vital information by measuring physiological analytes from sweat, saliva, or tear. In particular, glucose and lactate are targeted for real-time disease monitoring. Whole blood, serum, or urea, which are mostly used by other microfluidic platforms, provide higher concentrations and more precise measurements. On the flip side, it is very challenging to make continuous analysis using these fluids. Sweat, saliva, and tear are relatively easy to continuously sample and therefore can be potentially used for continuous, non-invasive monitoring of analytes using wearable platforms. For example, concentrations of the electrolytes (pH, sodium, calcium) and metabolites (glucose, lactate) in sweat provide vital health information [39]. Moreover, thanks to their printed embodiments, these platforms do not have to employ optical or microelectromechanical components, leading to inexpensive and robust sensing systems.

The microfluidic platforms are promising alternatives to the bulky, lab-based diagnostic equipment. So far, these systems have been mostly adapted at the developed world for rapid diagnostic needs at emergency settings or for advanced biochemical analysis. At the developing world, the driving force for the use of microfluidic diagnostic platforms was their low-cost and simplicity. In spite of the diversity of LOC platforms and their ability to tap into different markets, the number of commercial technologies that made it to the market are still limited considering the wide variety of applications demonstrated in academic publications. It is mainly due to the fact that engineering of these platforms requires multi-disciplinary teams and considerable budget to allow the technologies move beyond clinical trials successfully. In order to compete with the status quo, microfluidic platforms have to either demonstrate advanced functionalities or significant reduction in cost.

The twenty-first century is witnessing a shift in the healthcare services. With the increasing awareness of individuals on personal health conditions and healthcare technologies that allow continuous monitoring, our conception of diagnostics will evolve radically. The increasing interest on personalized medicine and

telemedicine are some of the indicators of this upcoming transition. Real-time investigation of the health status of a person without interfering with daily activities holds great promise for early detection of a wide variety of abnormalities. This early detection, and therefore early medical intervention, has the potential to dramatically decrease the burden of life-threating diseases. Wearable LOC platforms aim for this functionality. In the near future, rather than using textile or tattoo as a substrate, these platforms can be implanted into the body for continuous monitoring of physicochemical conditions.

When microfluidics and lab-on-a-chip systems were first introduced in 1990s, we have seen studies focusing on investigating individual cells in order to understand the building blocks of tissues, organs, and organisms. More recently, a collective approach has gained traction which aims to study interaction of cells and mimic the functionalities of organs on microfluidic platforms. These systems are called organ-on-a-chip platforms [40]. The ultimate aim of these studies is to create a human-on-a-chip by constructing each organ on the same platform. The human-on-a-chip will simulate the activities of individual organs as well as their collective behaviors. This will revolutionize the position of microfluidic platforms against conventional systems and the methods used for disease diagnosis as well as personalized treatment.

1.3 Physics of Microfluidics

The Navier-Stokes equation for a Newtonian fluid states that

$$\rho[\frac{\partial \vec{U}}{\partial \vec{t}} + (\vec{U}\cdot\vec{\nabla})\vec{U}] = -\vec{\nabla}P + \eta\nabla^2\vec{U} + \vec{f} \tag{1.1}$$

where U, P, ρ, and η are the velocity field, pressure, density, and viscosity of the fluid, respectively while f is body force densities. For a laminar, steady, unidirectional Parabolic flow of a Newtonian, incompressible fluid, the Navier-Stokes equation can be written as

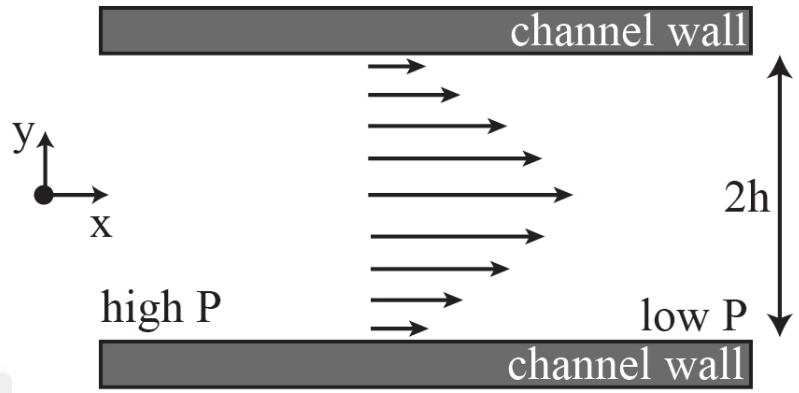


Figure 1.2: Parabolic flow profile.

$$\frac{dP}{dx} = \eta \frac{d^2U}{dy^2} \tag{1.2}$$

Integrating both sides of equation (1.2) gives

$$U = \frac{1}{2\eta}\frac{dP}{dx}y^2 - c_1 y - c_2 \tag{1.3}$$

where c_1 and c_2 are constants. Given that the flow velocity is zero at channel sidewalls, i.e. $U(y = h) = U(y = -h) = 0$, the maximum velocity at the center can be written as

$$U_{max}(y = 0) = \frac{1}{2\eta}\frac{dP}{dx}y^2(-h^2) \tag{1.4}$$

The mean velocity is then calculated by

$$U_{mean} = \frac{1}{2h}\int_{y=-h}^{y=+h} U(y)dy \tag{1.5}$$

where $2h$ is the width of the channel. Solving equation (1.5), the mean velocity becomes

$$U_{mean} = \frac{1}{3\eta}\frac{dP}{dx}(-h^2) \tag{1.6}$$

Volumetric flow rate (Q) is calculated using

$$Q = \frac{U}{A} \tag{1.7}$$

where A is the cross-sectional area of the channel that is πr^2 for a circular channel. Hence, putting equation (1.6) into equation (1.7), pressure drop ΔP across a channel length L becomes

$$\Delta P = Q\frac{8\eta L}{\pi r^4} \tag{1.8}$$

Equation (1.8) is the Hagen-Poiseuille equation named after Jean Léonard Marie Poiseuille and Gotthilf Heinrich Ludwig Hagen. In this equation, the hydrodynamic resistance R is

$$R = \frac{8\eta L}{\pi r^4} \tag{1.9}$$

which eventually gives a general equation relating the pressure difference, volumetric flow rate, and hydrodynamic resistance as

$$\Delta P = QR \tag{1.10}$$

For rectangular channel profile, the hydrodynamic resistance is

$$R = \frac{12\eta L}{wh^3} \tag{1.11}$$

where w is the channel width and h is the channel height. Therefore, equation (1.10) becomes

$$\Delta P = Q\frac{12\eta L}{wh^3} \tag{1.12}$$

Microfluidic channels can be modeled as electrical circuits, and electrical equivalent of equation (1.10) gives the famous Ohm's law

$$V = IR \tag{1.13}$$

where V is voltage, I is current, and R is resistance.

Numerous dimensionless numbers are used to investigate fluid flow characteristics. Reynolds number (Re) gives the ratio of inertial forces to viscous forces to determine the flow regime as

$$Re = \frac{\rho U l}{\eta} \tag{1.14}$$

where l is the characteristic length. When Re is below 2000, the system enters the laminar flow regime. Larger Re ($Re > 4000$) implies turbulent regime that implies unpredictable flow. Most microfluidic systems work in laminar flow regime.

1.4 Blood Circulation

Cardiovascular system is responsible for the transport of blood throughout the body and consists of heart and a network of vessels that sums up to 100,000 km. Heart works autonomously to transport 4-6 liters of blood. It acts as a pump to feed body with oxygenated blood and to convey venous blood to lungs for its oxygenation. These processes take place when heart rhythmically contracts and relaxes. Lungs convert dirty blood to oxygenized blood. With the contraction of heart, oxygenized blood is directed to aorta which splits into three paths. The first path feeds the heart itself, the second path feeds the upper part of heart including brain, and the third part feeds the lower part of heart [41]. Arteries transport clean blood, and veins carry dirty blood coming from the tissues and organs. The exchange of oxygen, carbon dioxide, and nutrients between body parts and blood is carried out by capillaries that have diameters of a few microns. In contrast, arteries and veins have diameters in the range of cm to mm. The connections between these large and small vessels are made by arterioles and venules. The velocity of blood flow decreases as blood flows from larger to small vessels [42, 43]. Hence, the velocity is highest at the arteries. Pressure fluctuation between 120 mmHg (systolic) and 80 mmHg (diastolic) at heart drives blood to the body. The fluctuation decreases away from heart, and pressure is around 35 mmHg with almost no fluctuations at the capillaries [41]. Pressure is determined by cardiac output, compliance, blood volume, blood viscosity, and vessel length/diameter. In large blood vessels, inertial effects are of importance. However, in microcirculation, inertial effects are negligible, and laminar flow is observed ($Re<1$). For example, Re is around 0.002 in a capillary with a diameter of 5 μm and velocity of 1 mm/s [42, 43].

Table 1.1: Values of cross-sectional area, flow velocity, and Reynolds number for different vessel types.

Vessel	Total cross-sectional area (cm^2)	Velocity (cm/s)	Re
Aorta	2.5	33	3000
Small arteries	20	4.12	80
Arterioles	40	2.05	0.5
Capillaries	2500	0.033	0.05

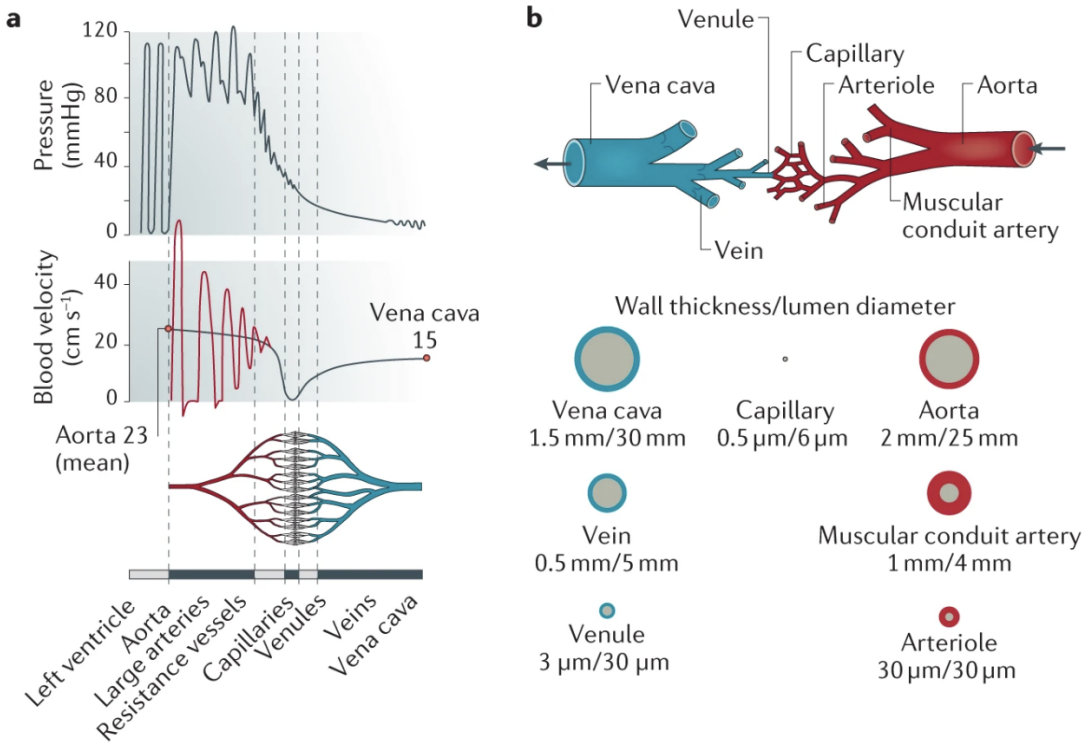


Figure 1.3: **a.** Pressure and velocity distribution in vessels. **b.** Vessel diameters [44]. Reproduced with permission from Springer Nature.

1.5 Erythrocytes

Blood consists of cellular elements (erythrocytes, leukocytes, and platelets) and a suspending medium (plasma). Plasma is 92% water in addition to 7% plasma proteins including albumin, globulins, and fibrinogen. Erythrocytes are the most abundant cells in blood comprising 99% of cellular elements and 45% of blood volume. This makes an erythrocyte count of 20-30 trillion in a healthy human at any time [44, 45].

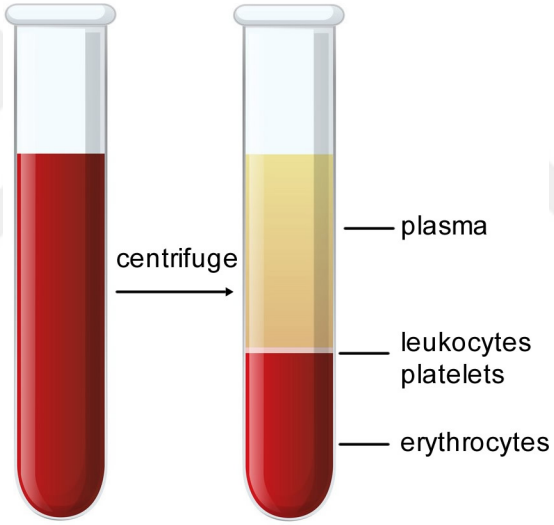


Figure 1.4: Blood consists of cells (erythrocytes, leukocytes, and platelets) and plasma.

Erythrocytes were first discovered from frog blood under a microscope in 1658 by Jan Swammerdam They are produced in bone marrow from stem cells in around 7 days. Around 2.5 millions of these cells are produced in a second. A cell completes a cycle in the body in 20 seconds [41]. In normal conditions, erythrocytes have biconcave shapes with a diameter of 8 μm and thickness of 2 μm. This represents a surface area of around 140 μm^2 which is higher than the surface area of a sphere (97 μm^2) with identical volume (90 fl) [45]. This allows the cells to have more room for oxygen delivery.

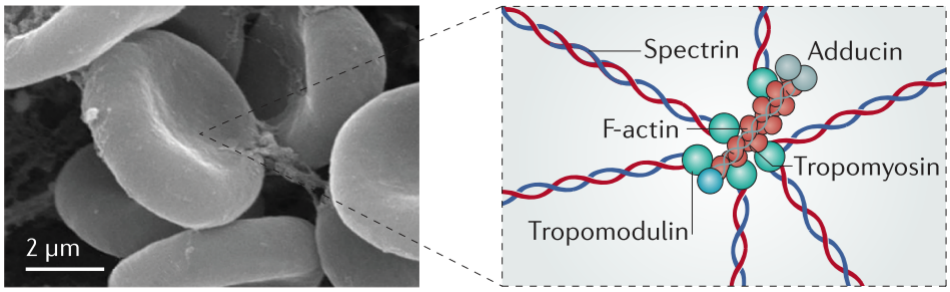


Figure 1.5: Erythrocytes and membrane proteins [44]. Reproduced with permission from Springer Nature.

10-nm cell membrane consists of three layers: outer carbohydrate-rich glycocalyx, a middle lipid bilayer, and inner cytoskeleton. The unique dimple structure of cells is provided by the viscoelastic membrane proteins forming the cytoskeleton such as spectrin [46]. Erythrocytes lack a nucleus in the cytoplasm containing about 300 million hemoglobin molecules that are made up of proteins and iron [41]. Hemoglobin has four folded chains of a protein named globins, each of which is bound to a heme molecule containing an iron ion. Each ion can bind to one oxygen molecule. Hence, a single erythrocyte can transport 1.2 billion oxygen molecules during circulation. Oxygen carrying hemoglobin is named oxyhemoglobin that becomes deoxyhemoglobin when releasing oxygen [47]. Together with hemoglobin, cytoplasmic viscosity of an erythrocyte is around 7 mPa/s. The life time of a cell is 120 days. Following 120 days, cells are removed by macrophages. The general condition for the deficiency of erythrocyte or hemoglobin quantity is anemia that has more than 400 variations. As a result of abnormal production, destruction, or removal of erythrocytes, people suffer from insufficient oxygenation. Several well-known types include sickle cell anemia and iron deficiency anemia. My grandmother suffers from a genetic disorder named thalassemia; hence, she has to receive blood transfusion once in two months. Even though the sizes of erythrocytes are larger than capillaries, they can pass through these small vessels due to their cellular deformability provided by viscoelastic membrane proteins. The deformability of cells is essential for proper oxygen delivery and is a key determinant of blood flow [45]. Pathological alterations in deformability dramatically affect body oxygenation and result

in serious injuries. Popular diseases affecting deformability include malaria and diabetes. Malaria is caused by a virus named Plasmodium and claims 1-2 millions of lives per year. Virus causes around 50 membrane disorders and increases cell rigidity in such levels that cells block capillaries [48]. A variety of methods can be employed for deformability analysis: flow systems and single-cell systems. The former includes viscometers or laser diffractometers while the latter includes micropipette aspiration, optical tweezers, or atomic force microscopy. Microfluidic platforms are also used for this purpose including cell blockage, cell transit, optical stretching, and electrical impedance in microchannels [49]. Another major characteristics of erythrocytes is their aggregations at low shear rates ($< 0.01\ s^{-1}$) in the presence of appropriate molecules like plasma proteins fibrinogen and globulins. Erythrocyte aggregation is not observed in healthy circulation. However, disorders decreasing shear rate or increasing aggregation inducers' concentration cause aggregation that could block vessels. Other factors affecting aggregability include hematocrit, erythrocyte shape, and membrane properties (charge, elasticity). Aggregation is a reversible process. There are two models to explain the reason for this phenomenon: bridging and depletion. While the former assumes that the molecules act as a bridge by adsorption onto the surfaces to connect the cells, the latter claims that a depletion layer is created where cells form intimate contact to each other [50, 51].

1.6 Blood Rheology

Viscosity is a material's resistance to external deformation and is measured by rheometers/viscometers. Water is a Newtonian fluid for which viscosity does not change with applied shear rate. In contrast, blood is a shear-thinning non-Newtonian fluid [52]. Its viscosity drops with increasing shear rate. The main determinants of shear-thinning nature of blood are aggregation and deformation properties of erythrocytes. At low shear rates, blood viscosity is higher due to erythrocyte aggregation. As shear rate increases, erythrocytes disaggregate, deform, and eventually elongate to claim a minimum viscosity [53].

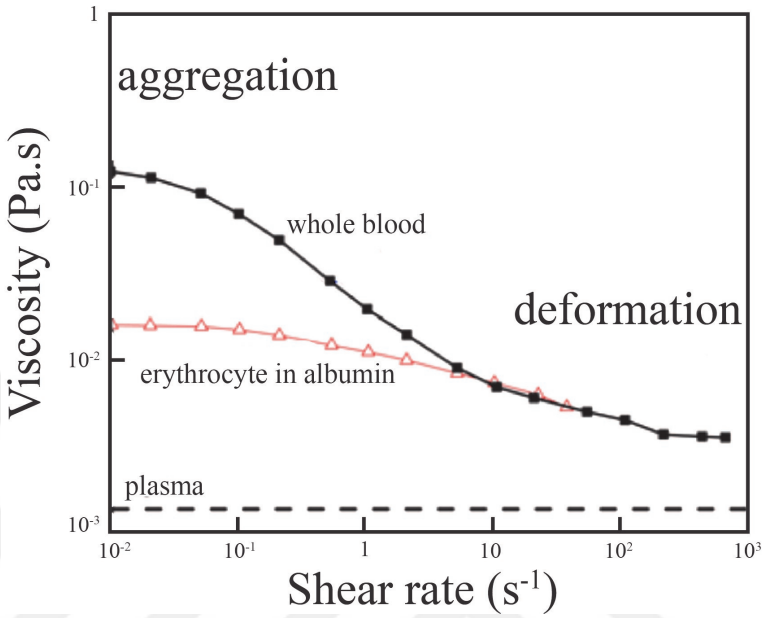


Figure 1.6: Viscosity of blood and plasma as a function of shear rate. Whole blood is a shear-thinning fluid [54]. Reproduced with permission from The American Association for the Advancement of Science.

Another important factor to decrease viscosity in circulation is the formation of cell-free layer near vessel walls named F*å*hraeus-Lindqvist effect following its discovery in 1931 [55]. In vessels with diameters between 10-300 μm, erythrocytes migrate away from the vessel walls and tend to get closer to center where flow velocity is higher. This forms a cell-free layer where plasma and other cellular components flow. In capillaries with diameters smaller than an erythrocyte, erythrocytes move in a single file [42, 53].

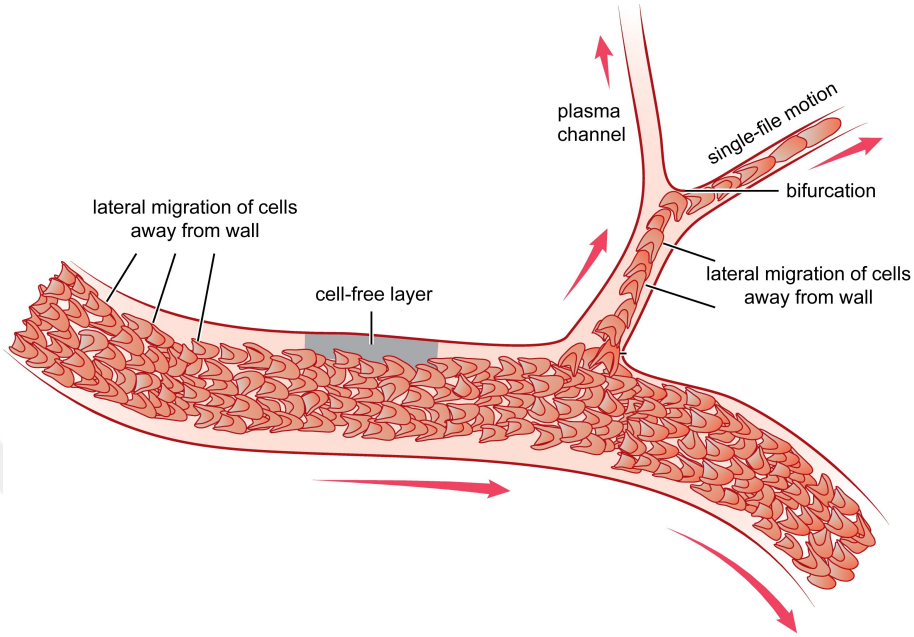


Figure 1.7: Schematic of blood flow in a vessel network [42]. Reproduced with permission from Annual Reviews.

The term rheology comes from the Greek word "rhein" that means "to flow". Hence, rheology literally means "flow science" [56]. However, rheology is interested in both flow behavior of liquids and deformation behavior of solids. Hemorheology is the study of flow characteristics of blood. The main hemorheological properties are deformation, aggregation, sedimentation, and volume fraction of erythrocytes as well as blood and plasma viscoelasticity [49, 50]. Together with hemodynamics properties (blood pressure, cardiac output, structure of vessels) [57], hemorheological properties determine blood flow in circulation. Whole blood and plasma demonstrate both Newtonian viscous and Hookean elastic behaviors. Blood viscoelasticity was first demonstrated by Thurston (1972) with stress measurements during oscillatory flow of blood [58]. Later in 2013, plasma was also demonstrated to be a viscoelastic fluid using elongational flow due to polymeric plasma proteins like fibrinogen [59]. Hemorheological properties are all interdependent to each other. For example, a decrease in erythrocyte deformation increases blood viscosity and decreases erythrocyte aggregation; an increase

in erythrocyte aggregation increases blood viscosity; an increase in plasma viscosity increases erythrocyte deformation. Also, external factors can affect multiple properties at the same time. For example, elevated fibrinogen concentration increases erythrocyte aggregation and plasma elasticity; increasing shear rate decreases erythrocyte aggregation and increases erythrocyte deformation.

1.7 Viscoelasticity

The two-plates model considers two identical plates with a distance h between them. The upper plate of area A is moved with a velocity v in response to an applied force F while the lower plate is stationary. The shear stress τ is then

$$\tau = \frac{F}{A} \tag{1.15}$$

The shear rate $\dot{\gamma}$, also called strain rate or rate of deformation, is

$$\dot{\gamma} = \frac{v}{h} \tag{1.16}$$

The ratio of shear stress to shear rate is a material constant, viscosity η, that is the material's resistance to deformation.

$$\eta = \frac{\tau}{\dot{\gamma}} \tag{1.17}$$

Ideally viscous fluids, Newtonian fluids, have a constant viscosity irrespective of applied shear rate. The behavior of a Newtonian fluid can be modeled as a dashpot. Under a constant force, the dashpot fluid flows with a constant velocity and deformation rate. Once the force is removed, the piston stops, and the fluid remains in the final deformation [56].

The two-plates model can also be used for solids. The lower plate is stationary, and the upper plate is deflected by a force F resuting in a deflection s. The shear deformation, also called shear strain, is then

$$\gamma = \frac{s}{h} \tag{1.18}$$

The rigidity of a material can be quantified as rigidity modulus (*shear*) G that is

$$G = \frac{\tau}{\gamma} \tag{1.19}$$

Modulus of elasticity (*tensile*) E is then

$$E = 2 \cdot G(1 + \mu) \tag{1.20}$$

where μ is Poisson's ratio. E is also defined as

$$E = \frac{\sigma}{\varepsilon} \tag{1.21}$$

where σ is the tensile stress and ε is the tensile strain/elongation. Ideally elastic solids, Hookean solids, have constant rigidity modulus irrespective of the degree and duration of shear force. The behavior of a Hookean solid can be modeled as a spring. Under a constant force, the spring deforms immediately and remains in the deformed state as long as the force is applied. Once the force is removed, the spring immediately returns to undeformed state [56].

Viscoelastic materials behave as viscous and elastic at the same time. They give a time-dependent and delayed response to applied/removed stress or strain. To summarize the previous notations, τ and σ are stresses; γ and ε are strains; $\dot{\gamma}$ and $\dot{\varepsilon}$ are strain rates. Therefore,

$$\varepsilon = \frac{1}{E}\sigma \tag{1.22}$$

$$\dot{\gamma} = \frac{1}{\eta}\tau \;\Rightarrow\; \dot{\varepsilon} = \frac{1}{\eta}\sigma \tag{1.23}$$

For viscoelastic materials, there are various mathematical models including the Maxwell and the Kelvin-Voigt [60].

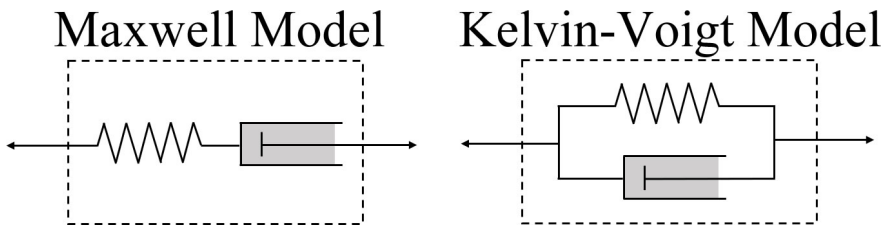


Figure 1.8: Maxwell and Kelvin-Voigt models of viscoelastic materials.

The Maxwell model is constructed by serial connection of a spring and a dashpot. These two components experience the same stress σ and share the total strain as ε_1 for the spring and ε_2 for the dashpot. In other words,

$$\varepsilon_1 = \frac{1}{E}\sigma \ , \ \dot{\varepsilon}_1 = \frac{1}{\eta}\sigma \ , \ \varepsilon = \varepsilon_1 + \varepsilon_2 \tag{1.24}$$

Hence,

$$\sigma + \frac{\eta}{E}\dot{\sigma} = \eta\dot{\varepsilon} \tag{1.25}$$

The Kelvin-Voigt model consists of a spring and a dashpot connected in parallel. Strain on both components is the same, but stresses are different being σ_1 for the spring and σ_2 for the dashpot.

$$\varepsilon = \frac{1}{E}\sigma_1 \ , \ \dot{\varepsilon}_1 = \frac{1}{\eta}\sigma_2 \ , \ \sigma = \sigma_1 + \sigma_2 \tag{1.26}$$

Hence,

$$\sigma = E\varepsilon + \eta\dot{\varepsilon} \tag{1.27}$$

If we apply a load σ_0, the stress is taken up by the dashpot since it is late to respond immediately. So, we have a creep curve with an initial slope of σ_0/η. Then, some strain occurs, and stress is shared by both elements, making the slope of the creep curve σ_2/η. When the stress in the dashpot approaches zero, all stress goes to the spring making the maximum strain σ_0/E. Solving equation 1.27 for $\varepsilon(0) = 0$, we obtain

$$\varepsilon(t) = \frac{\sigma_0}{E}(1 - e^{-(E/\eta)t}) \tag{1.28}$$

If we unload the material at $t = \zeta$, equation 1.27 becomes $0 = E\varepsilon + \eta\dot{\varepsilon}$. Solving this results in

$$\varepsilon(t) = C(e^{-(E/\eta)t}) \tag{1.29}$$

where C is a constant. At $t = \zeta$, equation 1.28 becomes

$$\varepsilon(\zeta) = \frac{\sigma_0}{E}(1 - e^{-(E/\eta)\zeta}) \tag{1.30}$$

Equation 1.30 can be considered as the initial condition such that $C = \varepsilon(\zeta)$. Hence, equation 1.29 for $t > \zeta$ is

$$\varepsilon(t) = \frac{\sigma_0}{E}(1 - e^{-(E/\eta)\zeta})(e^{-(E/\eta)t}) \tag{1.31}$$

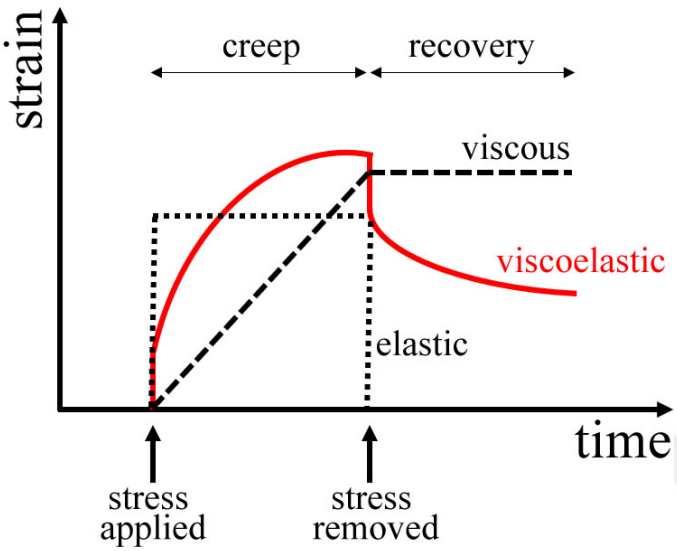


Figure 1.9: Creep-recovery response of viscous, elastic, and viscoelastic materials [61]. Reproduced with permission from Cambridge University Press.

1.8 Optics Concepts

Efforts in understanding light date back many centuries ago. The father of modern optics is considered to be Ibn Al-Haytham (965-1040) who had around 50 surviving-to-date key publications including *Book of Optics* and *Treatise on Light*. Progressing to relatively modern times, Willebrord Snell (1591-1626) experimentally demonstrated the refraction phenomenon, deflection of light passing from one medium to another. Later, two theories were proposed to explain the nature of light: the particle and wave theories. The former was pioneered by Descartes (1596-1650) and Isac Newton (1642-1727) proposing that light consisted of small particles. These particles are today named as photons that are changeless and massless. A photon carries energy calculated by $E = hc/\lambda$ where h is Planck's

constant, c is the speed of light (3x10^8 m/s), and λ is the wavelenght of light. The early contributors of the development and demonstration of the wave theory in the eighteenth-century were Christiaan Huygens, Augustin -Jean Fresnel, and Thomas Young, acclaimed for his double-slit experiment. In the nineteenth-century, theoretical and experimental findings of James Clerk Maxwell and Heinrich Hertz, respectively, demonstrated that light is an electromagnetic wave [62].

The distance where an electromagnetic wave with a speed v repeats itself is called the wavelength (λ). The period (T) is the calculated as $T = \lambda/v$. A more realistic 3D representation of an electromagnetic wave consists of electric and magnetic fields perpendicular to each other. Electromagnetic spectrum covers a range of wavelengths of electromagnetic radiation including the visible band between 350-750 nm. When the light interacts with a matter, absorption and scattering take place. Absorption is the transfer of energy from light to the matter. A green leaf is green because it absorbs all the colors but green. Scattering is, on the other hand, the change of direction of light following confrontation with the atoms/molecules of the matter [63].

Use of absorption, scattering, reflection, and transmission properties of biological tissues, and specifically blood, for biomedical investigation has a long history. Heart rate was first monitoring in 1937 by illuminating the toe of a person by two light sources of different wavelengths and analyzing the resulting intensity using a photocell [64]. Pulse oximetry is a similar measurement technique to measure oxygen saturation (SpO_2) quantifying the ratio of oxygenated (oxy-) and deoxygenated (deoxy-) hemoglobin. Absorption spectrum of blood in the visible and near-infrared range is dominated by erythrocytes. Leukocytes do not have any effect on optical properties [65]. Plasma and platelets are shown to affect the optical properties, but compared to erythrocytes, their effects are 100-1000 times lesser [65]. Erythrocytes' optical properties are determined by highly concentrated hemoglobin content. Around 30% of an erythrocyte and 95% of its dry matter is made up of hemoglobins. Absorption properties of hemoglobin depend on its oxygenation, but the general trend is that molar extinction coefficient decreases with increasing wavelength. Figure 1.10 demonstrates the optical absorption spectra of oxy- and deoxy- hemoglobin. Around 830 nm, the spectra

intersect and give a minimum absorption. We have used this wavelength in our studies to eliminate discrepancies in our results arising from hemoglobin oxygenation levels of blood samples. Erythrocyte aggregation and deformation are two important factors determining optical properties of blood. It is important to note that optical transmission through a blood sample is higher when the erythrocytes are (i) aggregated [66] or (ii) deformed [67], compared to the case where erythrocytes stay suspended in disaggregated, undeformed state.

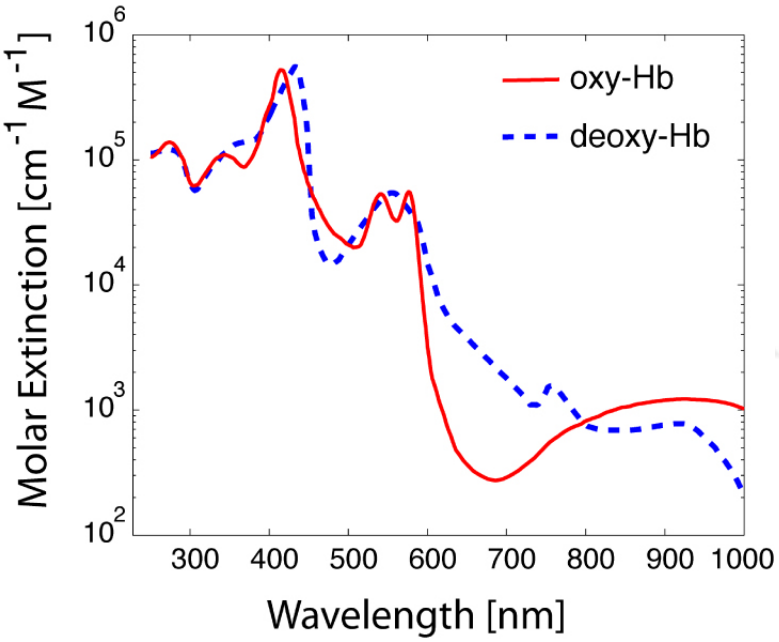


Figure 1.10: Molar extinction coefficients for oxy- and deoxy- hemoglobin. Reproduced with permission © 2010 Optical Society of America.

1.9 Thesis Outline

The ultimate aim of this study is to perform the measurement of all hemorheological properties and coagulation time parameters using a single microfluidic platform and measurement method. The significance of this study is that such a holistic measurement approach can bring benefits in terms of amount of sample volume, processing time, number of equipment, number of employees, laboratory

space, human errors, and cost to make the measurements accessible to all people. Our central hypothesis is that an optical transmission analysis of erythrocytes in a microfluidic channel can simultaneously quantify erythrocyte aggregation, erythrocyte sedimentation rate, erythrocyte deformation, blood viscoelasticity, and coagulation time using a single drop of whole blood. The innovation of this study is that there is, to date, no measurement method to address simultaneous measurement of the hemorheological properties and coagulation time parameters.

The rest of the thesis is organized as follows:

In Chapter 2, we describe and characterize the components and working principle of the microfluidic platform that performs optical transmission analysis of erythrocytes in a microfluidic channel. We demonstrate the measurement of erythrocyte aggregation and erythrocyte sedimentation rate using dextran-mediated blood samples.

In Chapter 3, we compare erythrocyte sedimentation rate measurement performance of the developed platform with the conventional equipment. We present the results of measurements carried out in a local hospital. We also present a novel channel design allowing simultaneous analysis of optical transmission through a blood sample and microscopic observation of erythrocyte aggregation process.

In Chapter 4, we present a novel assay for the determination of erythrocyte deformation and suspending medium viscoelasticity using optical transmission analysis. We introduce a four phase-oscillatory blood flow mechanism that allows application of four different shear rates in a 1 sec duration.

In Chapter 5, we present the measurement of coagulation time by optical investigation of erythrocyte aggregation process during the blood sample clotting. We present coagulation time measurement results carried out in a local hospital. We demonstrate the equally key role of fibrinogen proteins in erythrocyte aggregation and blood coagulation.

In Chapter 6, we present an alternative, entirely disposable microfluidic prothrombin time measurement platform that is based on migration analysis of blood

sample. An integrated effervescent pump mechanism is introduced. The platform is demonstrated to be suitable for both hospital and home use.

In Chapter 7, we give our concluding remarks and propose several future directions towards which this study could further proceed.

Chapter 2

Erythrocyte aggregation and sedimentation rate measurement using dextran-mediated blood

Erythrocyte aggregation (EA) is an intrinsic property of erythrocytes that form reversible stacked structures under low shear rates or at stasis. Erythrocyte sedimentation rate (ESR) is a frequently-performed clinical test. We propose a microfluidic platform and measurement method for optical measurement of EA and ESR from 50 μl blood. In this chapter, we describe the working principle of the platform and present proof-of-concept studies for employing EA dynamics for ESR measurement. We used an aggregation inducer, dextran polyglucose, for the preparation of multiple blood samples with different aggregation dynamics. Using these samples, we characterized the performance of the platform under varying experimental conditions. The detailed characterization presented in this chapter legitimates the feasibility of the system for ultrafast measurement of ESR in clinics and diverse off-laboratory settings.

The content of this chapter was published in [68] as;

Z. Isiksacan, M. Asghari, and C. Elbuken, A microfluidic erythrocyte sedimentation rate analyzer using rouleaux formation kinetics, Microfluidics and Nanofluidics, vol. 21, no. 3, p. 44, 2017.

2.1 Introduction

Erythrocytes form face-to-face linear or branched structures under static conditions or low shear rates in the presence of appropriate molecules [50]. This process is reversible, and cells can be dispersed individually when a disaggregating shear rate is applied to the cells [66]. In addition to (i) the shear forces applied to the cells [69] and (ii) the cellular factors (electrostatic repulsion, membrane strain) [70], the aggregation process is affected by the presence and concentrations of macromolecules in the suspending medium (dextran) [71–73]. Two hypotheses are proposed for the explanation of the aggregation dynamics, both without clear elucidation [50]: bridging and depletion [70, 73, 74]. The former claims that the cells clump due to the attractive forces caused by the adsorption of the macromolecules on the cell surfaces [75]. The latter proposes that aggregation occurs when macromolecule concentration near the cell surface is low [76].

Indirect screening of inflammatory conditions and some non-inflammatory disorders is carried out in clinics by a simple routine test named erythrocyte sedimentation rate (ESR). ESR expresses the separation rate of erythrocytes from plasma in a vertically positioned tube [77]. The plasma height, which is read after 1 h of sample introduction to the tube, gives the ESR value. ESR values above 30 mm/h are accepted to be in the clinical range and require further clinical investigation. In the clinical settings, the common techniques performed to determine ESR are Wintrobe [78] and Westergren [79] methods differing based on the tube size and anticoagulant type. The test is usually performed by a personnel in the clinics.

Stokes' Law states that the sedimentation velocity of particles is proportional to their sizes [80]. Since erythrocyte aggregates are larger in size compared to

individual cells, their sedimentation velocities are expected to be higher. In this chapter, this relationship was investigated for the realization of rapid ESR measurement from aggregation dynamics.

We used an aggregation inducer macromolecule (70 kDa Dextran) of different concentrations to change the aggregation dynamics of whole blood acquired from a single donor. We found a concentration interval where aggregation, thus ESR, increased linearly with dextran concentration. After finding the appropriate concentration levels, the performance of the microfluidic platform was successfully demonstrated. Disaggregation of the cells within microfluidic cartridges at the start of the test is critical, which is determined by the applied shear rate on the cells. We showed both computationally and experimentally that the choice/design of the mechanical unit, which was a pinch valve in this presented work, was critical to obtain adequate shear rate and therefore to perform a successful measurement. It was also shown that device orientation and vibrations did not alter the results of the ESR measurements.

2.2 Experimental

2.2.1 Sample Preparation

10 ml whole blood was obtained from a healthy male donor into a vacuum tube containing ethylenediamine-tetraacetic acid (EDTA; 1.5 mg/ml) to prevent coagulation. The blood was centrifuged three times at 4000 rpm for 4 min, and the plasma portion was replaced with 1x Phosphate-buffered saline (PBS) solution after each step. (i) After centrifugation, five micro centrifuge tubes (T1, ... T5) were filled with 500 μl of the PBS-suspended erythrocytes. Then, 70 kDa Dextran (Sigma-Aldrich) was added to the tubes at amounts of 0 mg, 2.5 mg, 5 mg, 7.5 mg, and 10 mg. Then, dextran was dissolved in the tubes by mixing the samples for 2 min with a pipette. (ii) For erythrocyte monitoring tests, after the centrifugation, a micro centrifuge tube was filled with 5 μl of the

PBS-suspended erythrocytes and 125 μl PBS. Then, 1 mg 70 kDa Dextran was added and dissolved by 2 min gentle mixing.

2.2.2 Particle Sedimentation Theory

Stokes' Law governs the settling velocity of a spherical particle suspended in a medium, where three forces act on the particle: gravitational (F_g), buoyancy (F_b), and drag (F_d) forces. Each can be written as follows:

$$F_g = \rho_{particle} V g \tag{2.1}$$

$$F_b = \rho_{medium} V g \tag{2.2}$$

$$F_d = 6\pi\eta r \upsilon \tag{2.3}$$

where ρ is density, V is particle volume, g is gravitational acceleration, η is medium dynamic viscosity, r is particle radius, υ is particle settling (termination) velocity. In a stationary system, no other force is effective on the system, thus yielding:

$$F_g = F_b + F_d \tag{2.4}$$

Plugging equations (2.1), (2.2), and (2.3) into (2.4), the particle velocity can be found as the following:

$$\upsilon = \frac{2g}{9} \frac{(\rho_{particle} - \rho_{medium})}{\eta} r^2 \tag{2.5}$$

For non-spherical particles, a correction factor called the dynamic shape factor, K, is applied to the drag force in equation (2.3), yielding:

$$F_d^{nonspherical} = 6\pi\eta r_e \upsilon K \tag{2.6}$$

where r_e is equivalent volume radius for a spherical particle that has the same volume as the non-spherical particle. By plugging equatians (2.1), (2.2), and (2.6)

into (2.4), the settling velocity valid for non-spherical particles can be found as follows:

$$v = \frac{2g}{9} \frac{(\rho_{particle} - \rho_{medium})}{\mu K} r_e^2 \tag{2.7}$$

According to equations (2.5) and (2.7), one can conclude that the sedimentation velocity of a particle in a medium is proportional to the square of the size of the particle. This expression is also valid for erythrocyte aggregates. For example, compared to a blood sample where all the erythrocytes are individually dispersed (case 1, Fig. 2.1), the settling of a blood sample with aggregated erythrocytes inside (case 2, Fig. 2.1) is more enhanced.

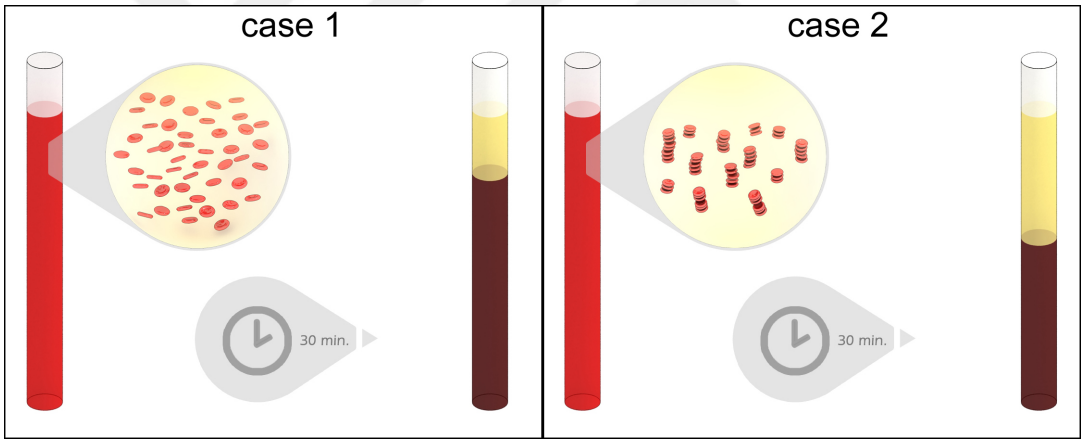


Figure 2.1: Schematic drawing of comparison of ESR depending on erythrocyte aggregability. Case 1 is when there are no aggregated erythrocytes.

2.2.3 Microfluidic Cartridge Fabrication

The material of choice for the microfluidic cartridges was polymethyl methacrylate (PMMA) since it is transparent, bio-compatible, and mass-producible. It was also easier to obtain channels on a PMMA cartridge with high aspect ratios, compared to polydimethylsiloxane (PDMS) [81]. The cartridge used for ESR measurements using dextran-mediated blood consisted of a 1 mm deep, 1 mm wide, and 50 mm long channel, with an inlet and outlet (single-channel cartridge). The cartridge patterns were drawn using a CAD software (Autodesk,

AutoCAD 2016) and fabricated by CNC machining.

For aggregation monitoring, channels with smaller depths were needed because of the high population and small size of erythrocytes (around 5-7 μm) that make their visualization challenging in deep channels. Therefore, a shallow PDMS microfluidic cartridge was designed for visualization of erythrocyte aggregation. The following equation should be satisfied to apply the same shear rates on cells in different channel segments when the same pressure is applied:

$$w_1 h_1^2 = w_2 h_2^2 \tag{2.8}$$

where w is the channel width and h is the channel height. Therefore, the width of the PDMS cartridge was defined according to the width (1 mm) and the height (1 mm) of the channel of the PMMA cartridge. The width was set to 150 μm for better cell visualization. The PDMS cartridge therefore consisted of a 150 μm deep, 44.5 mm wide, and 50 mm long channel. The PDMS cartridge was fabricated based on a modified version of a rapid fabrication method that we developed. Firstly, the patterns were drawn using a CAD software (Autodesk, AutoCAD 2016). Then, 150 μm thick double-sided tape was taped on a PMMA substrate, and the tape was laser-ablated using a 30 W CO_2 laser (Epilog, Zing) to obtain the desired patterns. After the ablation, the off-channel regions were peeled off from the substrate finalizing the mold. PDMS (Sylgard 184, Dow Corning), prepared at 10:1 ratio and debubbled, was poured onto the mold, and the mold was placed on a hotplate at 100 °C for 12 h for PDMS curing. Then, the cured PDMS was removed from the mold, inlet and outlet holes were punched, and the PDMS was bonded to a glass slide using O_2 plasma.

2.2.4 Measurement Platform

The developed platform consists of a disposable transparent cartridge and a portable analyzer. The analyzer consists of four modules: (I) cartridge fixation module, (II) shear force exertion module, (III) optical measurement module, and (IV) electronic control module (Fig. 2.2 and Fig. 2.3). The first module is a black PMMA based cartridge holder employed to tightly fix the cartridge once

inserted into the analyzer to prevent any vibration during the measurements. This holder also blocks the transmission of the background light to the photodetector, caused by ambient lighting. The second module is a solenoid pinch valve (EW-98302-06, Cole-Parmer, US) that is programmed to generate 10 s-long back and forth motion of the blood sample in the cartridge with a period of 2 s. The movements of the sample with a stroke distance of 5 mm exert a shear rate on the erythrocytes above the threshold for complete erythrocyte disaggregation.

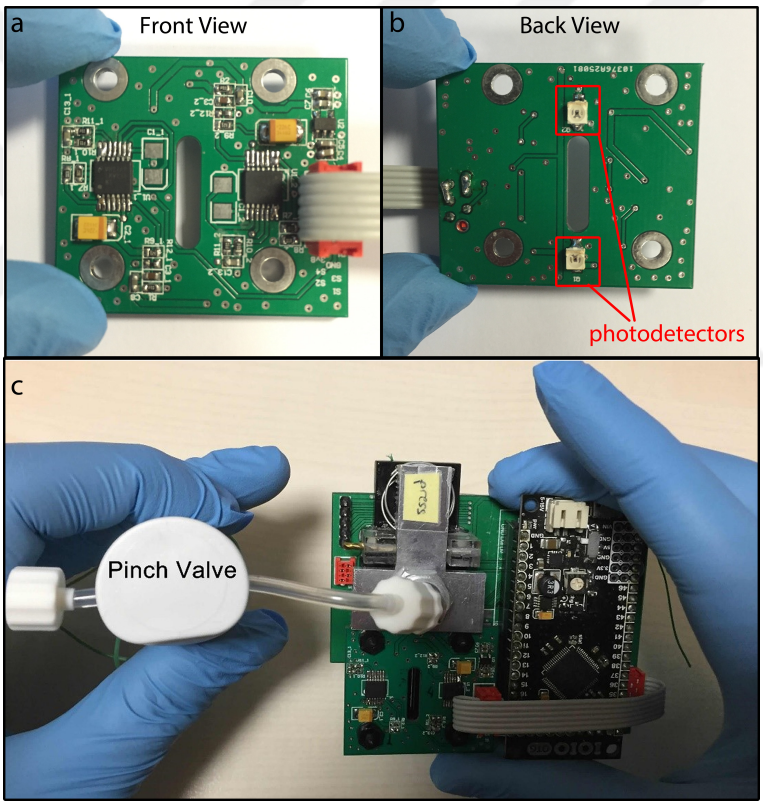


Figure 2.2: Top-view photography of the analyzer.

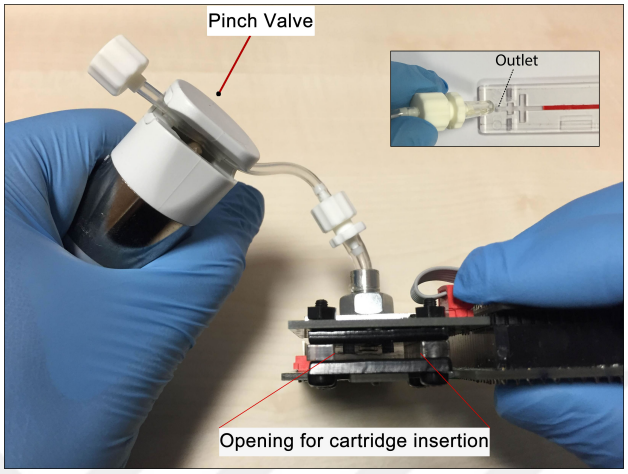


Figure 2.3: Side-view photography of the analyzer. Inset shows the cartridge outlet.

The measurement principle is based on the optical investigation of the erythrocyte aggregation. The optical measurement module consists of a light-emitting diode (LED) (VSMG2700, Vishay, US) and a photodetector (VEMT4700, Vishay, US) as schematically shown in Fig. 2.4. The LED illuminates the blood sample in the near-infrared band with 830 nm wavelength, at which hemoglobin and therefore WB absorption is minimum, whereas transmission of light is enhanced [82].

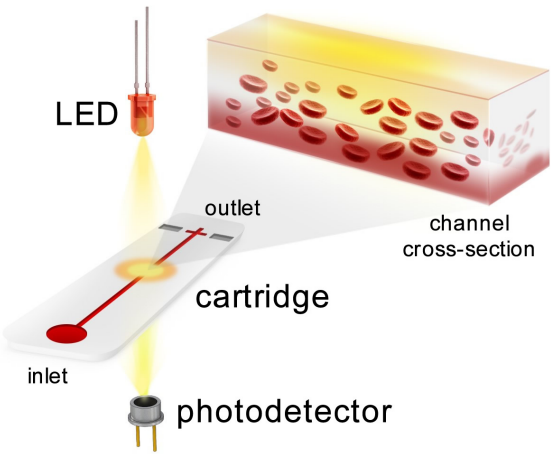


Figure 2.4: Schematic representation of the platform.

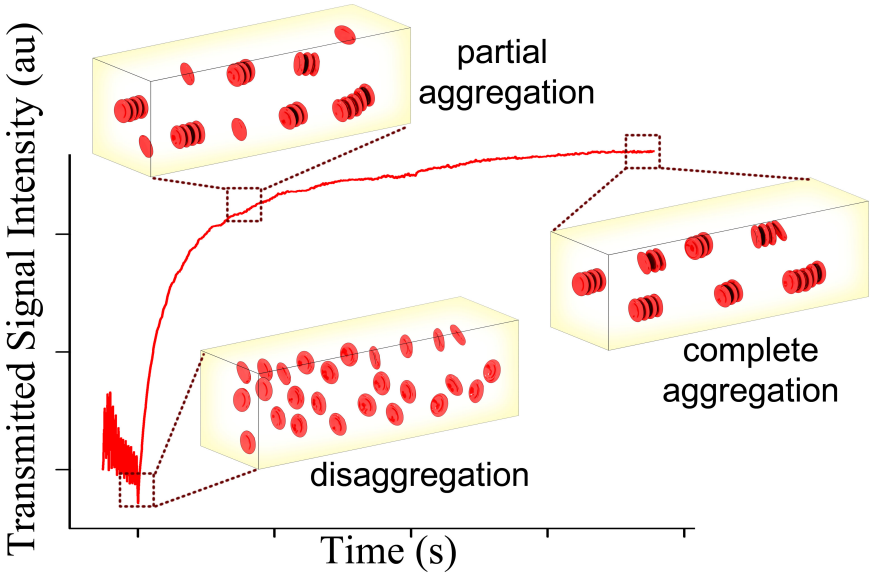


Figure 2.5: Typical transmitted signal intensity versus time curve.

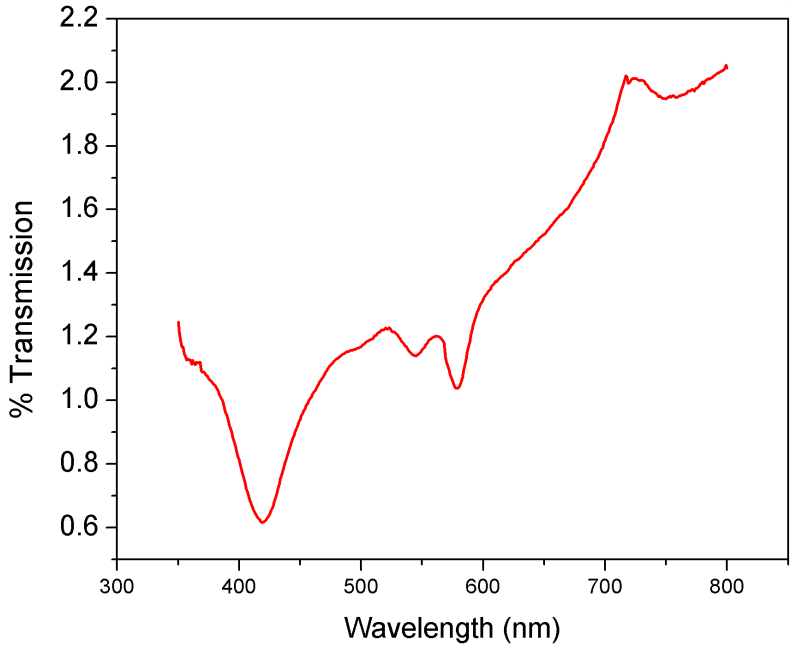


Figure 2.6: Transmission spectrum of whole blood.

The photodetector collects the light transmitted through the blood sample. The electronic control module consists of a printed circuit and a microprocessor

(IOIO-OTG, SparkFun, US). The circuit comprises a transistor functioning as a switch to control the pinch valve, a temperature controller to fix the test temperature at 37 °C, and a transimpedance amplifier – lowpass filter pair for the current-to-voltage conversion of the photodetector output. The microprocessor controls the assay parameters through a custom-developed Java-based software to set the LED intensity, shear force exertion time, temperature, and the total test duration.

2.3 Results and Discussion

2.3.1 EA and ESR Measurement using Dextran-mediated Blood

Five blood samples with different dextran concentrations were prepared: 0 mg/ml, 5 mg/ml, 10 mg/ml, 15 mg/ml, and 20 mg/ml. Since erythrocytes were suspended in PBS, all the macromolecules affecting the aggregation dynamics were out of play. Only consideration was the 70 kDa dextran that was known to alter the aggregation dynamics, by either inhibiting or enhancing it depending on the concentration. 50 μl of each sample was pipetted into a single-channel PMMA cartridge, and the optical transmission signal was collected for 150 s. Each sample was tested four times. Since the four signal profiles were almost the same, only one signal for each sample was presented in Fig. 2.7a. For the optical transmission signals, three sedimentation indices (SI_1, SI_2, and SI_3) were calculated for the quantification of aggregation (Fig. 2.7b). SI_1 was calculated by taking the ratio of the area under the signal curve (AUC) to the total area of the signal (AUC + AAC). SI_2 was the amplitude of the optical signal intensity, and SI_3 was the time when the intensity reached half of the maximum value. For a set of sedimentation index values, each value was also divided by the maximum value of the set. These indices were calculated at 30^{th}, 60^{th}, 90^{th}, and 120^{th} s of the optical transmission data. Fig. 2.7c shows the calculated SI_1 values at different dextran concentrations and at different analysis times. Similarly, Fig. 2.7d and

2.7e illustrate the SI_2 and SI_3 values, respectively. According to these results, it was evident that amplitude (SI_2) was the only index that increased almost linearly with the dextran concentration. In addition, at a given dextran concentration, SI_2 did not vary significantly as a function of analysis time. Therefore, SI_2 was accepted as the most legitimate index for the quantification of aggregation. 1) An increase in the concentration of dextran increased the amplitude of the transmitted signal intensity. 2) The increasing signal intensity implied the formation of larger aggregates. Therefore, we believe that dextran macromolecules are adsorbed onto the cell surfaces to enhance aggregation.

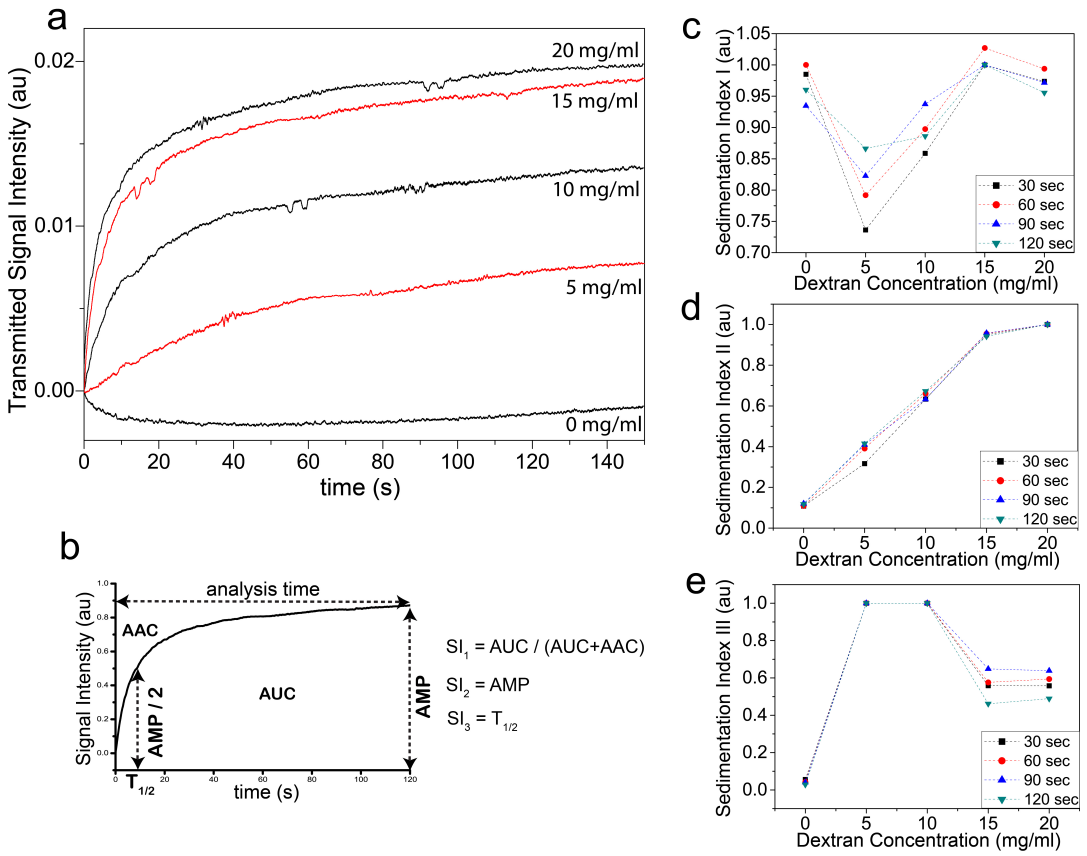


Figure 2.7: Blood samples with different dextran concentrations tested with the microfluidic system. **a.** Transmitted signal intensities of five samples were measured using the system. The signals are offset to zero initial intensity. **b.** Schematic drawing of a representative transmission signal and the sedimentation indices calculated from the signal. **c.** SI_1, **d.** SI_2, and **e.** SI_3 at different dextran concentrations and analysis times.

As the optical measurements were carried out using the microfluidic platform, 75 μl from each of the blood samples was taken into a hematocrit tube (inner diameter: 1 mm, length: 75 mm). Then, the tubes were placed vertically on a stationary rack to measure the sedimentation rates of the erythrocytes for each sample using the conventional method (Fig. 2.8, at the start of the test).

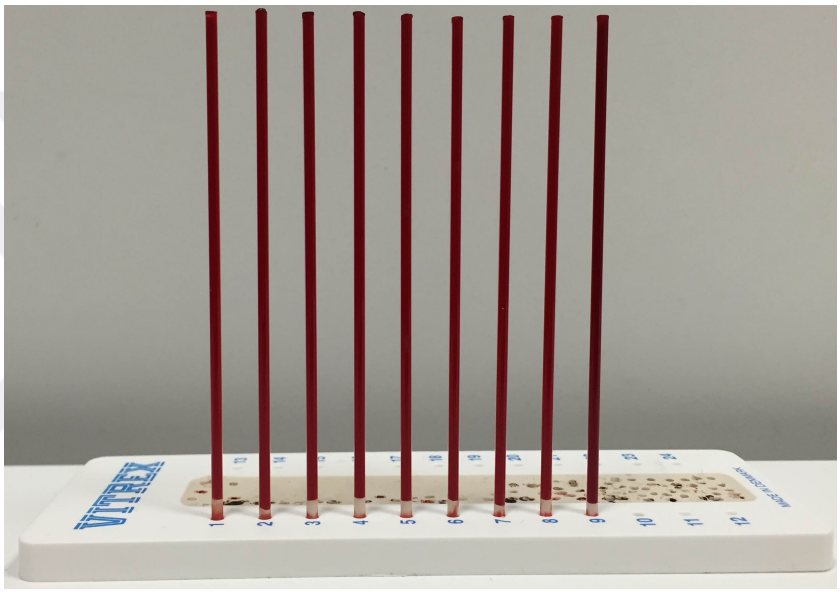


Figure 2.8: Hematocrit tubes filled with different blood samples for ESR analysis.

The five hematocrit tubes containing the samples of various concentrations were observed for a total of 4 h. At the end of the 1^{st}, 2^{nd}, 3^{rd}, and 4^{th} h, pictures of the tubes were taken, and ESR was calculated from these pictures. These values were used to compare the conventional measurement results and the microfluidic measurement results obtained using SI_2 at various analysis times (Fig. 2.9b). According to Fig. 2.9b, the correlation between the conventional measurement results and the microfluidic measurement results was above 80% for all the analysis times of the optical signal (30^{th}, 60^{th}, 90^{th}, and 120^{th} s) and at any reading time of the ESR from the hematocrit tubes (1^{st}, 2^{nd}, 3^{rd}, and 4^{th} h).

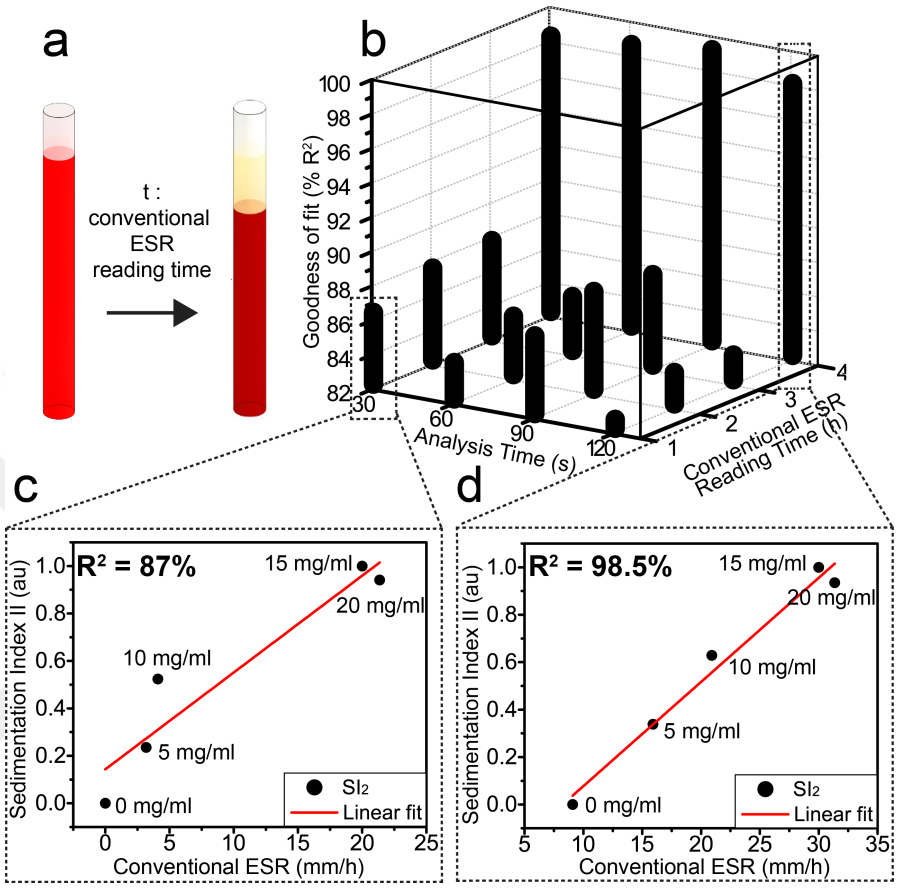


Figure 2.9: Comparison of the conventional and microfluidic measurement. **a.** Schematic representation of the conventional ESR measurement. **b.** Goodness of fit of the linear regression curve for conventional measurement result versus microfluidic measurement result at different signal analysis times and different hematocrit tube reading times. **c.** Comparison of the conventional ESR measurement read after 1 h of sample introduction and SI_2 of the optical transmission signal calculated at 30^{th} s analysis time. **d.** Comparison of the conventional ESR measurement read after 4 h of sample introduction and SI_2 of the optical transmission signal calculated at 120^{th} s analysis time.

Variations among correlation coefficient values for different optical signal analysis times and different ESR reading times were due to several internal factors including sample viscosity, ambient temperature, and cell deformability. These

factors might have different effects on cell sedimentation (conventional measurement) and cell aggregation (microfluidic measurement). Specifically, Fig. 2.9c gives correlation coefficient (%R^2) of 87% for 30^{th} s analysis time and 1^{st} h conventional ESR reading time using linear regression, and Fig. 2.9d gives correlation coefficient (%R^2) of 98.5% for 120^{th} s analysis time and 4^{th} h conventional ESR reading time using linear regression. This confirmed that the sedimentation rate of erythrocytes obtained from the conventional method and the aggregation rate of erythrocytes obtained from the microfluidic method have a direct relationship, proving the validity of the developed system for ESR measurement. From Fig. 2.9b, it is also clear that the analysis time of 90 s gives the highest correlation. Therefore, this analysis time was used at further studies.

2.3.2 Effect of Measurement Conditions

For point-of-care applications, microfluidic systems should endure off-laboratory use by non-specialists. Normally, similar diagnostic devices operate on a laboratory bench or a desk. On the other hand, handheld devices should be robust enough to handle a variety of the use scenarios during the operation. Therefore, we investigated the performance of the microfluidic system when the device orientation was varied, where the extreme condition was the vertical device orientation. In addition, such a comparison is critical to verify that the underlying effect, which yields the optical signal demonstrated in Fig. 2.7a, is the aggregation of erythrocytes, rather than their sedimentation.

For these experiments, we used the PBS-suspended and 10 mg dextran-added blood sample (T3 tube). The sample was tested 5 times in each of the two device orientations, horizontal and vertical, using single-channel cartridges. The optical transmission signals obtained from these 10 tests were analyzed to calculate SI_2 at 90^{th} s for each test. Following it, the mean and standard deviation of the results at the horizontal and vertical device orientation were calculated. When compared, the mean values of 0.98 (horizontal) and 0.99 (vertical) show that the results are independent of device orientation. The low standard deviation

values in both cases (horizontal SD = 0.01, vertical SD = 0.001) demonstrate the high repeatability of the rapid ESR measurement. These tests also verify that the developed system investigates the aggregation dynamics within the channel rather than the sedimentation effect of the cells that would otherwise have had different effects at the two device orientations.

For devices that utilize optical measurement/detection mechanism, vibrations can interfere with the measurement results by increasing the baseline noise level. Therefore, we also investigated the measurement performance of the system when the device is mechanically disturbed. Disturbance is created by harshly hitting with a plastic hammer at a region on the desk that was 20 cm far from the system. A total of six tests were performed. Each disturbance generated a mean instant force of 157 N (+/- 20 N) at the hitting region. Figure 2.10 shows the intensities of the transmission signals obtained from the tests using 10 mg dextran-added sample. The black squares in the plots denote the times at which the disturbance was created during the tests. After the tests, the SI_2 at 90^{th} s was calculated from the optical signals for each test. The mean of the SI_2 values of the six tests (mean = 0.91) as well as the standard deviation of the test results (SD = 0.046) were calculated. The standard deviation is in an acceptable range, implying that the mechanical disturbance did not affect the test performance.

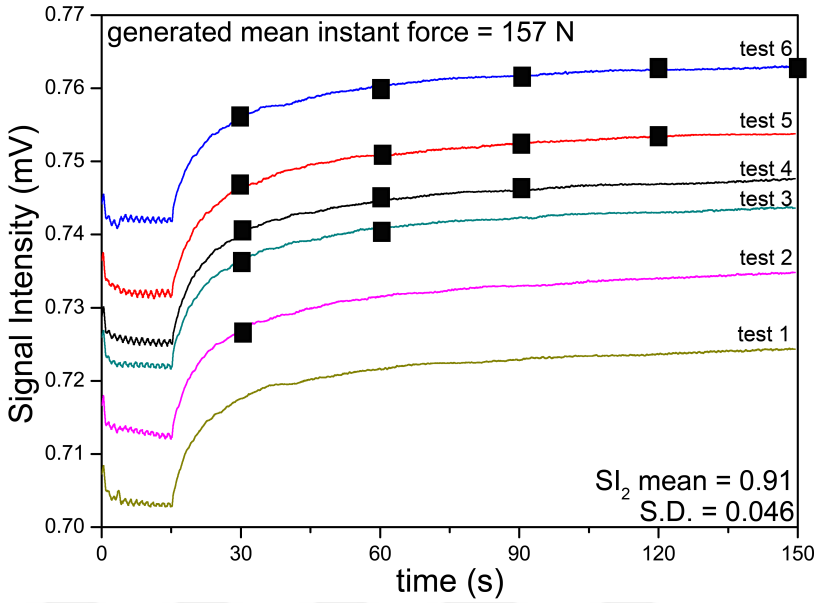


Figure 2.10: Investigation of the effect of vibration on the optical measurements. Six tests were performed using the same blood sample. Black squares denote the times for external disturbance of 157 N (+/- 20 N). Mean and standard deviation calculated from the SI_2 values at the 90^{th} s for each signal were given.

2.3.3 Effect of Shear Rate on Erythrocyte Disaggregation

One of the major issues of the presented microfluidic ESR system and the conventional Westergren assay is the dependence of the results to the initial condition of the sample, which is assumed to be complete disaggregation of erythrocytes. For the conventional assay, it is expected that operator disaggregates the blood sample by gentle upside down motion of the blood tube. Our system frees the user from this constraint by performing a sample shaking action for 15 s before initiating the optical measurement. However, complete disaggregation of the sample depends on the microfluidic channel design, sample amount, and the mechanical unit used for disaggregation. In this section, we evaluate the performance of the pinch valve in achieving the complete disaggregation state in order to develop a foolproof sample conditioning for our system.

Blood is a non-Newtonian fluid demonstrating shear-thinning behavior [83]. Different models, such as Cross [84], Walburn-Schnock [85], Carreau [86], have been developed to explain the non-linear shear rate and shear stress relation for non-Newtonian fluids. Among all, the Carreau-Gambaruto model has gained more attention due to the higher agreement between computational and experimental results for blood. According to the Carreau model, the viscosity of a non-Newtonian fluid can be given as:

$$\eta = \eta_{inf} + (\eta_0 - \eta_{inf})[1 + (\lambda\dot{\gamma})^2]^{(n-1)/2} \tag{2.9}$$

where η is viscosity, $\dot{\gamma}$ is shear rate, η_0 and η_{inf} are the zero and infinite shear rate limit viscosities, λ is the relaxation time constant, and n is the power law index. For blood, the constants were previously reported as $\eta_0 = 0.0456$ Pa.s, $\eta_{inf} = 0.032$ Pa.s, $\lambda = 10.03$ s, and $n = 0.344$.

Due to its low cost and ease of integration, we used a pinch valve in our system to achieve complete erythrocyte disaggregation before the onset of the optical measurement. We aimed to see the effect of the pinch valve on the disaggregation of erythrocytes using the Carreau-Gambaruto model. A finite element modeling software, COMSOL 5.0, was employed to study this effect. First, the PMMA channel with 1 mm width, 1 mm depth, and 50 mm length was drawn as shown in Fig. 2.11a. The laminar flow regime was applied with momentum balance and continuity equations using the shear parameters given in the Carreau-Gambaruto model for blood. There are several pinch valves that are commercially available. As an example, we compared two pinch valves designed for different tubing dimensions for their disaggregation performance: EW-98302-06 (Cole-Parmer) and EW-98302-00 (Cole-Parmer). When these pinch valves were employed in the microfluidic system, the flow rates of blood in the channel was measured as 5 mm^3/s and 0.6 mm^3/s, respectively. These flow rates were applied to the software for the inlets, and atmospheric pressure was used as the outlet boundary condition. The fluid was assumed to be fully developed. No slip boundary condition was used for the walls, and the fluid was assumed to be incompressible. Fine meshes were created that gave 1,002,047 elements. Mesh types for cross sections and along the channels were free triangular and swept, respectively. Figure 2.11a and 2.11b give the shear rate distributions along the channel for EW-98302-06 (PV-1)

and EW-98302-00 (PV-2) pinch valves, respectively. To further investigate the shear rates formed at different points in the channel, center lines were drawn along one of the identical side of the channel surfaces and the channel center. As shown in Fig. 2.11c, for the channel center line, PV-1 creates shear rates that vary between 2.5 – 4.5 s^{-1}, and PV-2 creates shear rate around 0.1 s^{-1} along the channel. Along the channel surfaces, shear rates applied to the cells by PV-1 and PV-2 are around 50 s^{-1} and 6 s^{-1}, respectively as shown in Fig. 2.11d. It was previously demonstrated that shear rates below 1 s^{-1} is not sufficient for erythrocyte disaggregation. An effective shear rate range for disaggregation was reported to be 1 $s^{-1} < \dot{\gamma} < 100$ s^{-1}. These results suggest that PV-2 fails to provide the threshold shear rate required for erythrocyte disaggregation, whereas PV-1 provides the required shear rate both at the channel surface and the center.

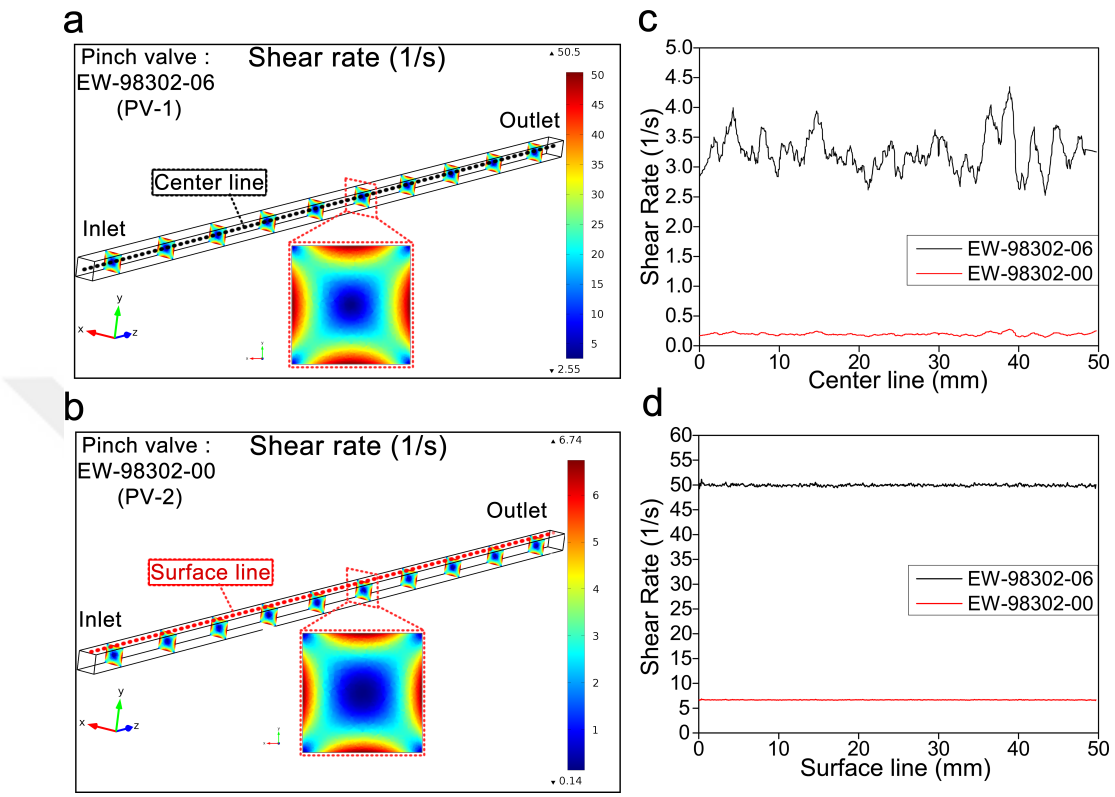


Figure 2.11: Finite element model results showing the shear rate distributions applied to erythrocytes in the channels for different pinch valves. **a.** Shear rate distribution when PV-1 pinch valve was employed. **b.** Shear rate distribution when PV-2 pinch valve was employed. **c.** Shear rate along the center line passing through the center of the channel. **d.** Shear rate along the line passing through the center of bottom/top/left/right surface, respectively.

To experimentally verify our computational results, two PDMS cartridges were fabricated for microscopic observation: one for PV-1 and the other for PV-2. We pipetted the dextran-added dilute blood samples into the cartridges. PV-1 and PV-2 were connected to the outlets of the cartridges. The pinch valves were operated for 15 s, and the cells were observed under microscope using 40x microscope objective (Axio Vert.A1, Zeiss) immediately after stopping the pinch valve action. As shown in Fig. 2.12a and 2.12b, there is a significant difference between the two cases. PV-1 can achieve complete disaggregation, whereas PV-2 falls short in applying enough shear rate to disaggregate the cells resulting in

large rouleaux after the pump stops as seen in Fig. 2.12b. It is important to note that Fig. 2.12a shows some small stacks of erythrocytes which formed after the cease of the valve's operation, confirming the rapid timescale of aggregation process reported in the literature.

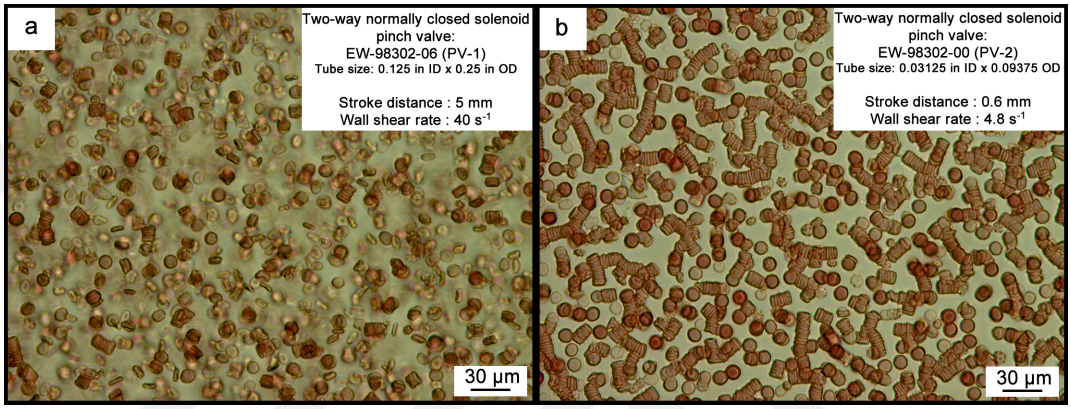


Figure 2.12: Visual observation of erythrocytes just after the pinch valves stopped operating. **a.** PV-1 was employed, and cells were disaggregated. **b.** PV-2 was employed, and disaggregation was not achieved.

2.4 Conclusion

In this chapter, we demonstrated the feasibility of the microfluidic platform for the measurement of erythrocyte sedimentation rate utilizing the aggregation dynamics of erythrocytes within 50 μl blood samples. Dextran-mediated blood samples with different dextran concentration were prepared, which showed varying erythrocyte aggregability properties. A dextran concentration interval was found where erythrocyte aggregation and correspondingly sedimentation rate increase linearly with the increasing concentration. We showed that the orientation of the device does not alter the test results, validating the use of the microfluidic system for hand-held use by non-professionals. Additionally, mechanical disturbances during the test were shown not to affect the optical signals obtained from the system. Also, two different pinch valves were integrated to the system, and

their performances for forming the required shear rate allowing erythrocyte disaggregation were characterized computationally and experimentally. Finite element modelling was employed to find the shear rates on cells at different locations along the channel. Afterwards, the pinch valves were integrated to the system, and the stronger valve was experimentally shown to successfully disaggregate the cells.

Chapter 3

Clinical erythrocyte sedimentation rate measurement from erythrocyte aggregation

Erythrocyte sedimentation rate (ESR) is a frequently used clinical test for screening of several inflammatory conditions, infections, trauma, and malignant disease, as well as non-inflammatory conditions including prostate cancer and stroke. In the previous chapter, we presented proof-of-concept studies for a method for ESR measurement from EA. In this chapter, we present the results for clinical measurement of ESR from EA using the microfluidic platform. We experimentally showed a significant correlation (R^2 = 86%) between conventionally measured ESR and EA. The microfluidic system was shown to measure ESR from EA in 2 min. We also developed another microfluidic cartridge specifically for monitoring EA process in real-time during ESR measurement.

The content of this chapter was published in [51] as;

Z. Isiksacan, O. Erel, and C. Elbuken, A portable microfluidic system for rapid measurement of the erythrocyte sedimentation rate, Lab on a Chip, vol. 16, no. 24, pp. 4682-4690, 2016.

3.1 Introduction

Erythrocytes form 3D aggregates that resemble rolls of coin at stasis or during low shear rates in plasma or an appropriate suspending medium [50, 87]. This reversible process is the main factor for the non-Newtonian nature of blood at low shear rates, and as such, plays a critical role for blood flow [75, 88, 89]. EA is affected by (i) intrinsic cellular properties (membrane deformability and surface charge density) [70, 90, 91], (ii) suspending medium properties (fibrinogen concentration in plasma or aggregation-inducer macromolecule concentration such as dextran) [72, 73, 92–95], and (iii) shear forces on cells [66, 69, 96]. EA is of clinical importance for diseases such as sepsis, thrombosis, and circulatory diseases [97, 98]. Most studies demonstrate aggregometers that measure EA using photometric methods that quantify light beam reflected from or transmitted through a blood sample during aggregation process [66, 99–105]. These aggregometers differ from each other based on their mechanical unit, which creates the shear force required for disaggregation. Image analysis of EA under different dynamic conditions and computational analysis have also been employed for the quantification of EA [106–109]. Custom-made optical systems (microscopes and holograms) are also proposed for erythrocyte analysis. These systems carry out non-invasive single cell investigation such as morphological properties, volume, and refractive index based on interferometric methods [110–113]. Due to the complexities of the optical systems and image retrieval algorithms, these systems are impractical for rapid and facile monitoring and quantification of fast aggregation process [114].

Erythrocyte sedimentation rate (ESR) was discovered in 1897 [115] and widely accepted in 1918 [79]. It is a simple clinical test commonly used as a sickness index for monitoring several inflammatory diseases such as temporal arteritis [116, 117] and polymyalgia rheumatic [118–120]. It is also accepted as a critical prognostic factor in some non-inflammatory conditions including stroke [121], heart attack [122], and prostate cancer [123]. ESR reflects the rate of settling of erythrocytes in a vertically placed tube filled with whole blood. The erythrocyte-free plasma height at the top of the tube is measured after 30 or 60 min and reported as the

ESR value in mm/h. The Westergren method is the gold standard method for ESR measurements, in which a tube with a length of 300 mm and inner diameter of 2.55 mm is used which requires 5 ml of whole blood sample [124, 125].

Lab-on-a-chip technologies for blood analysis and their commercialization possess significant potential for healthcare [126, 127]. There are studies that led to benchtop commercial products, which measure ESR from aggregation dynamics [128, 129]. They work much faster than the Westergren method (5 min) and use smaller sample volumes (150 μl). These products function as photometric rheoscopes, however the detailed working principles of these products are not disclosed. Therefore, it is not possible to evaluate the underlying fundamental phenomena that form the basis of faster ESR measurements claimed in these devices. In this chapter, we aim at explaining the fundamental relationship between EA and ESR by visualizing the whole disaggregation/aggregation process and correlating it with the corresponding optical transmitted signal obtained from the system.

In the previous chapter, we measured the rate of EA and used it to predict ESR, leveraging the relationship between particle size and sedimentation rate. Particle sedimentation in a suspending medium is explained by Stokes' Law, which states that the sedimentation velocity of a spherical particle is proportional to the square of its radius square [80]. EA forms clusters of erythrocytes that have higher sedimentation velocity compared to individual erythrocytes. We explored this direct relationship between erythrocyte aggregates and their settling velocity in order to perform rapid ESR measurements from EA. In this chapter, we demonstrated that our microfluidic system can clinically measure ESR from EA using only 50 μl whole blood in 2 min. The test cycle starts off by completely disaggregating erythrocytes in the cartridge using a rigorous back and forth fluid motion generated by a solenoid pinch valve. Then, the fluid motion is ceased, and cells start to aggregate. During this aggregation phase, near infrared light (λ = 830 nm) optically transmitted through the cartridge is measured for 1.5 min. Then, ESR value is calculated using the optical signal change. For experimental verification of the microfluidic system and the measurement method, whole blood samples of 70 patients were tested with our system. The microfluidic system was

shown to correlate with the conventional Westergren method with $R^2 = 86\%$ using linear regression. This value is higher than the correlation coefficients of commercially available ESR analyzers. In addition, we integrated a camera to the system and designed a new cartridge including a section for visual observation of EA process in real-time during ESR measurement. Using this unique cartridge, we were able to demonstrate the one-to-one correspondence between the aggregation of erythrocytes and the optical transmission signal.

3.2 Experimental

3.2.1 Sample Preparation

For clinical measurement of ESR, whole blood was used without any pre-processing to the blood sample. Therefore, for ESR measurements, 5 ml fresh venous blood was acquired from 70 volunteers into vacuum tubes containing ethylenediamine-tetraacetic acid (EDTA; 1.5 mg/ml) to prevent coagulation. For visual observation of erythrocytes, pre-processing of whole blood was needed, which consisted of PBS washing, dilution, and dextran addition. Therefore, for EA monitoring, 5 ml fresh blood was acquired from a healthy male volunteer into a vacuum tube containing ethylenediamine-tetraacetic acid (EDTA; 1.5 mg/ml) to prevent coagulation. The blood was centrifuged three times at 3500 rpm for 4 min, and plasma was replaced with 1x PBS solution each time. A micro centrifuge tube was filled with 5 μl of the plasma-free blood sample and 125 μl PBS and mixed. Then, 1 mg, 150 kDa Dextran (Sigma-Aldrich) was added to the tube and dissolved by gentle mixing for 1 min using a pipette.

3.2.2 Microfluidic Cartridge Fabrication

Disposable cartridges used in this work were fabricated out of polycarbonate (PC), a transparent thermoplastic polymer. The channel designs were made in

2D using a CAD software (Autodesk, AutoCAD 2016). We had two different cartridge designs. (i) For ESR measurements, cartridge-1 was used, which has a 1 mm deep, 1 mm wide, and 50 mm long channel. (ii) For simultaneous ESR measurement and EA monitoring, cartridge-2 was used, which has a single inlet and outlet and composed of two sections: a deep section ($h_1 = 1$ μm) for ESR measurement and a shallow section ($h_2 = 150$ μm) for EA monitoring. Cartridge-1 was mass-produced out of polycarbonate (PC) using injection molding to minimize chip-to-chip variations. Cartridge-2 was fabricated out of PMMA using CNC-machining.

The relationship between the erythrocyte settling velocity and erythrocyte aggregation is based on the Stokes' Law, which is a fundamental equation in fluid mechanics. There are also commercial benchtop instruments that report ESR values within minutes using EA. However, in the literature, there are strong oppositions to the use of these devices, since ensuring complete disaggregation of the erythrocytes is critical for correlating EA and ESR. Therefore, it is utmost importance to visualize the behavior of erythrocytes during the whole process and correlate it with the optical signal. Cartridge-2 was specifically designed for this purpose. For the optical transmission signal, the system requires a strong interaction between the incident light and the erythrocytes; therefore, the optical path length should be increased using a deep channel. However, monitoring of individual erythrocytes is not possible in a deep microchannel due to the high population of erythrocytes. The visualization system requires a smear-like blood sample. Cartridge-2 accommodates both microchannel segments: a shallow channel for monitoring of individual erythrocytes and a deep channel for optical measurement. However, changing the channel depth changes the wall shear rate as well as the disaggregating force on erythrocytes. Therefore, the width of the shallow channel is increased to ensure that the same wall shear rate is experienced in both channel segments as described below.

Volumetric flow rate Q of a liquid flowing in a channel is described as

$$Q = Uwh \tag{3.1}$$

where U is mean velocity, w is channel width, and h is channel height. Since the

flow rates are the same in the shallow and the deep channel sections of cartridge-2, the following must hold:

$$U_{deep} w_{deep} h_{deep} = U_{shallow} w_{shallow} h_{shallow} \tag{3.2}$$

According to Weissenberg-Rabinowitsch-Mooney equation, the wall shear rate $\dot{\gamma}$ is described as

$$\dot{\gamma} = \frac{6Q}{wh^2} \tag{3.3}$$

When equation (3.1) is plugged into equation (3.3), the following is found:

$$U = \frac{\dot{\gamma} h}{6} \tag{3.4}$$

Replacing the mean velocity (U) in equation (3.2) with the one in equation (3.4) for both deep and shallow sections, the following equation is obtained:

$$\dot{\gamma}_{deep} w_{deep} h_{deep} = \dot{\gamma}_{shallow} w_{shallow} h_{shallow} \tag{3.5}$$

We require that the disaggregating shear rates $\dot{\gamma}$ on erythrocytes in both sections be equal, i.e., $\dot{\gamma}_{deep} = \dot{\gamma}_{shallow}$. Thus, we require:

$$w_{deep} h_{deep} = w_{shallow} h_{shallow} \tag{3.6}$$

The channel heights were set as $h_{deep} = 1$ mm and $h_{shallow} = 150$ μm. The widths for both sections were set as $w_{deep} = 1$ mm and $w_{shallow} = 44.5$ mm. The lengths were chosen as $L_{deep} = 50$ mm, and $L_{shallow} = 7.5$ mm. The length of the deep channel segment (50 mm) is the same as the length of cartridge-1.

3.2.3 Measurement Platform

The same measurement platform presented in chapter 2 was used. Cartridge-1 was fabricated for the optical measurement of ESR, since a dense population of erythrocytes was required for stronger interaction of the cells with the incident light in order to obtain satisfactory signal change on the photodetector. Cartridge-2 was designed for real-time observation of the erythrocytes during the

whole test cycle. Cartridge-1 takes 50 μl whole blood sample, and cartridge-2 takes 200 μl pre-processed blood sample. Upon the sample introduction into the cartridge, the test cycle was started by completely disaggregating the erythrocytes for 10 s using the pinch valve. Then, the valve was turned off, allowing the cells to re-aggregate. During the aggregation process, the sample was illuminated with the LED, and the transmitted light was measured by the photodetector. Within the channel, each individual erythrocyte acts as a scattering center. Since the individual erythrocyte population is high, the intensity level is at its lowest when the cells are completely disaggregated. On the other hand, the intensity level reaches to its maximum at complete aggregation. Between the min and max values, as cells aggregate, the intensity level increases. The transmitted signal was recorded for 90 s. The amplitude of the transmitted signal, which is the difference between the signal level at 90^{th} s and the signal level at the start of aggregation process, was calculated using Matlab (R2014, MathWorks) and recorded as the aggregation index (AI). The results are verified using the measurements performed using the conventional Westergren method. For real-time observation of EA process, the shallow section is monitored using a 40x microscope objective (Axio Vert.A1, Zeiss) coupled to a camera (Axiocam ICc 1, Zeiss).

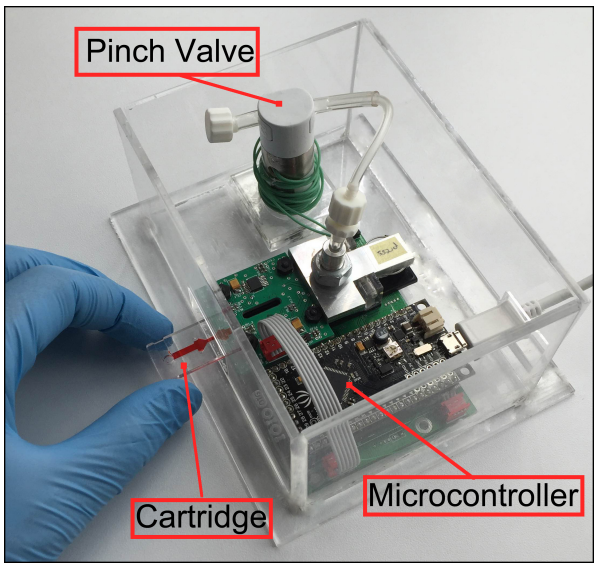


Figure 3.1: Photograghy of the platform.

3.3 Results and Discussion

3.3.1 Quantifying the Aggregation of Erythrocyte

The microfluidic system records the optically transmitted light through the blood sample. The minimum intensity of the light indicates complete disaggregation of the cells. During the aggregation process, the intensity level increases. To quantify the aggregation of erythrocytes, two aggregation indices (AI_1 and AI_2) were calculated. AI_1 is the area under curve (A) divided by the total area (A+B) of the transmitted signal, whereas AI_2 is the amplitude (AMP) that corresponds to the change of the transmitted signal. The total analysis time is another parameter to be considered. We have calculated AI_1 and AI_2 for a series of analysis durations from 30 s to 120 s. Figure 3.2a shows the transmitted signal intensities of four whole blood samples with different ESR values (11 mm/h, 16 mm/h, 33 mm/h, and 54 mm/h) measured using Westergren method. The samples were chosen such that two samples were in the normal ESR range (0 mm/h $\leq$ ESR $\leq$ 30 mm/h), and the other two were in the clinical ESR range (ESR $>$ 30 mm/h). The signals were recorded for 120 s after complete disaggregation. For each test, the two aggregation indices were calculated for different assay times (30, 36, 42, ..., 120 s). Using the two aggregation indices defined above, in total 32 AI values were calculated. Then, for each of the 32 AIs, the parity plot was obtained using the ESR values measured by the 30-min Westergren method (W 30) and the AI of interest. For each curve, the goodness of the fit (R^2) was calculated. Figure 3.2b and 3.2c give the goodness of fit of AI_1 and AI_2, respectively, measured for different analysis durations. As seen in Fig. 3.2, R^2 for AI_1 differs significantly for different test durations whereas R^2 for AI_2 is consistent and has a value closer to 1 at all assay times.

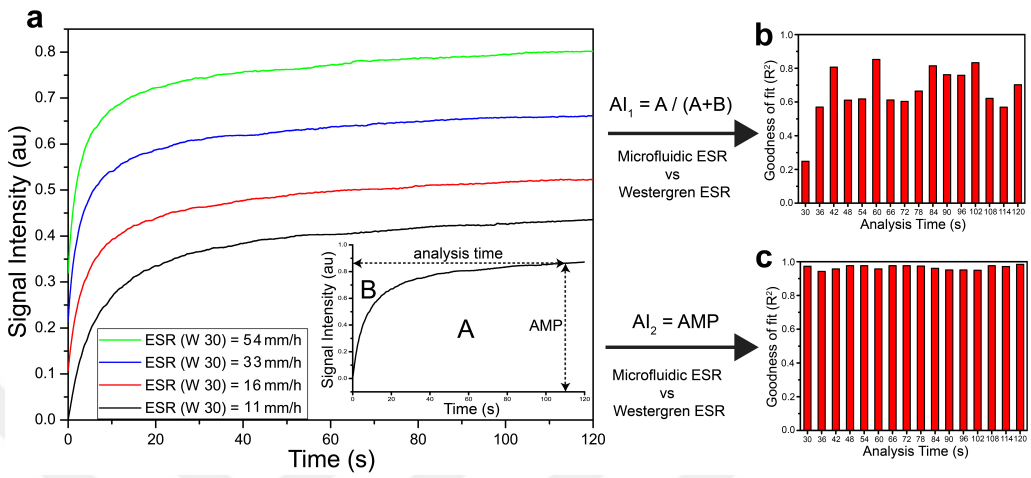


Figure 3.2: Aggregation indices calculated for the ESR measurement. n = 4 whole blood samples were tested using Westergren ESR analyzer as reference. **a.** Transmitted signal intensity of the 4 samples recorded for 120 s using the microfluidic system. Goodness of fit, R^2, between the Westergren ESR and microfluidic ESR for **b.** AI_1 and **c.** AI_2 measured at increasing analysis times.

3.3.2 ESR Measurement with the Microfluidic Platform

After determining the aggregation index that has the highest correlation with the conventional ESR method, whole blood samples of 70 volunteers were tested with the microfluidic system and compared with the measurements obtained by the gold standard method. Attention was paid to span a wide dynamic range covering both the healthy and clinical ESR ranges. The ESR values of the samples were first measured using the automated ESR analyzer (Linear Chemicals, Autoanalyzer) employing 30-min Westergren ESR method within 1 h of venipuncture. Upon the measurement with the analyzer, 50 μl whole blood was withdrawn from each Westergren tube and tested with the microfluidic system at room temperature. AI_2 measured at 90^{th} s was chosen as the basis for the microfluidic ESR method. This value was calculated from the transmitted signal intensity of each volunteer sample. The regression analysis of the measurements is shown in Fig. 3.3, where the y-axis is the conventionally measured ESR values of the 70 volunteers, and the x-axis is the calculated aggregation indices corresponding to each

sample's optical transmission signal as shown in Fig. 3.3. The overall correlation coefficient (R^2) of the regression curve is 0.86. The correlation coefficient (R^2) is 0.79 in the normal ESR range (0 mm/h $\leq$ ESR $\leq$ 30 mm/h), whereas it is 0.69 in the clinical ESR range (ESR $>$ 30 mm/h).

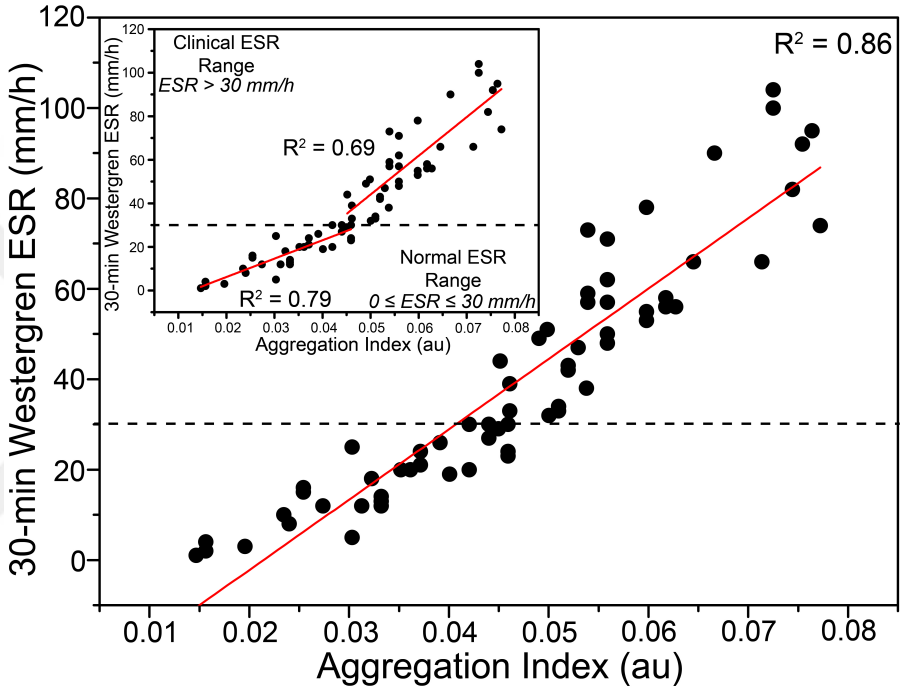


Figure 3.3: Comparison of the microfluidic system test results with the gold standard Westergren method. n = 70 whole blood samples tested using the Westergren ESR analyzer (y-axis) and the microfluidic system (x-axis). Goodness of fit, R^2, is 0.86 using linear regression analysis. Inset: n=35 blood samples in the normal ESR range (0 – 30 mm/h), R^2 of 0.79; n=35 blood samples in the clinical ESR range ($>$ 30 mm/h), R^2 of 0.69.

In the clinics, ESR value of 30 mm/h is accepted as the cut-off for further investigation of infection [98,120,124]. Therefore, we analyzed our results both in the whole dynamic range and also in healthy and clinical ranges. The correlation coefficient value in the normal ESR range (0 – 30 mm/h) is higher than that in the clinical ESR range ($>$ 30 mm/h). Although the correlation is weakened at high ESR values, it does not pose a problem for the microfluidic ESR system; since quantitative analysis is not required for high ESR values in the clinics. It suffices

to identify the patients with high ESR values who are directed to specialists for further analysis.

3.3.3 Precision and Repeatability

After finding the linear equations that are used to calculate ESR values from the AI_2 measurements, the performance of the microfluidic system was further evaluated. First, the precision of the microfluidic system was tested. For the precision tests, whole blood samples of 5 volunteers were first measured with the Westergren method as 4, 21, 33, 54, and 100 mm/h (Fig. 3.4, x-axis). Following the conventional measurements using Westergren analyzer, each sample was tested five times with the microfluidic system. The mean values were 4, 21, 36, 46, and 78 mm/h, respectively (Fig. 3.4, y-axis). The standard deviation for each sample was calculated as 0.82, 0, 1.41, 5.03, and 1.64 mm/h, respectively, and shown as error bars in Fig. 3.4.

The measurements for the precision tests (Fig. 3.4) were repeated immediately one after the other, determining how precise the measurements were within a very short period of time. It is also important to look at the device performance when there is a delay between the repetitive measurements. Clinically, this is a significant concern, since the time gap between the blood sampling from the patient and testing in the central laboratory varies from a few minutes to 4-5 hours. This time gap shows variability not only between different health centers but also within the same center. Therefore, it is critical to test the repeatability of the system for samples stored in blood sampling tubes for different times. For these repeatability tests, two whole blood samples were chosen with ESR values of 30 mm/h and 57 mm/h (W 30). The samples were tested four times using the microfluidic system over the course of 3 h, with 1 h delay between measurements. As shown in Fig. 3.7a, for the sample with an ESR value of 30 mm/h, the mean and the standard deviation of the four measurements were 27.3 mm/h and 1.3 mm/h, respectively. For the 57 mm/h ESR sample, the mean and the standard deviation were 52 mm/h and 2.9 mm/h, respectively. These results

demonstrate that aggregation dynamics of the erythrocytes are not affected with the 3 h storage of the sample at room temperature.

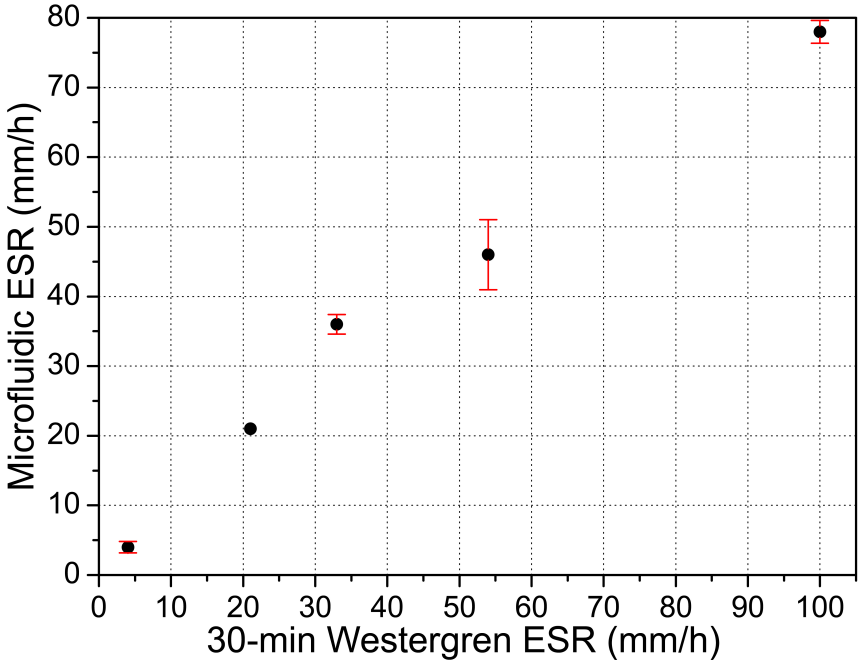


Figure 3.4: Precision tests for the microfluidic system. n = 5 whole blood samples tested. Samples were first tested with the Westergren ESR analyzer (x-axis), and five times with the microfluidic system (y-axis). Error bars denote 2 standard deviation (SD).

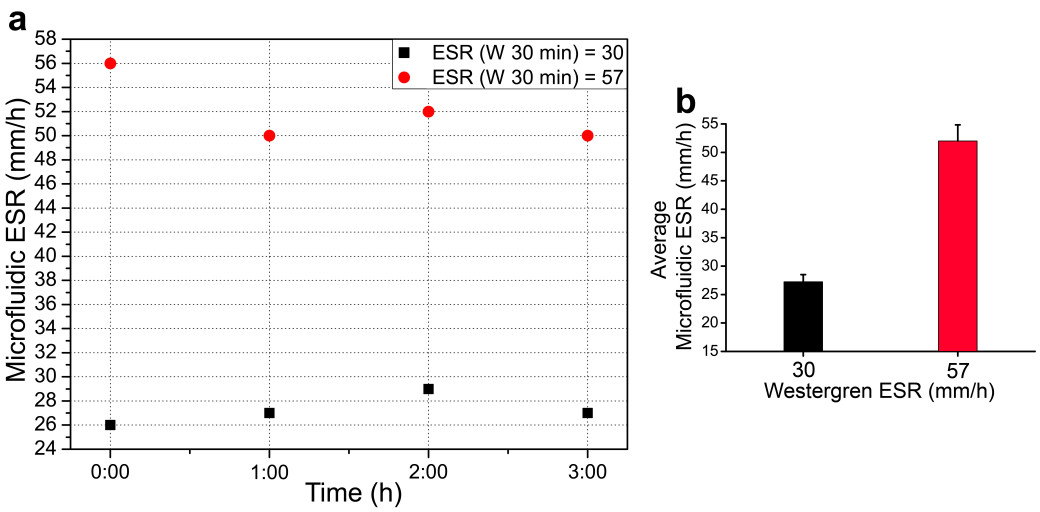


Figure 3.5: Repeatability performance of the microfluidic system. **a.** n = 2 whole blood samples with the ESR (W 30 min) values of 30 mm/h (black) and 57 mm/h (red) tested with the microfluidic system. Samples were first tested with the Westergren ESR analyzer, and then four times with the microfluidic system with 1 h delay between consecutive tests. **b.** (black) the mean (27.25 mm/h) and SD (1.26 mm/h) for the sample with ESR of 30 mm/h and (red) the mean (52 mm/h) and SD (2.83 mm/h) for the sample with ESR of 57 mm/h.

3.3.4 Simultaneous ESR Measurement and EA Monitoring

Another major goal of this study is to demonstrate the correspondence between the erythrocyte aggregation dynamics and the optical transmission signal obtained from the portable microfluidic system. Figure 3.7 shows the transmitted signal intensity for the pre-processed blood sample filled within cartridge-2. The intensity-time curve includes both the disaggregation phase (lasting for 15 s) and the aggregation phase (lasting for 6 min). The blood sample was diluted (plasma-free and suspended in PBS) to observe individual cells in the shallow section. Then, 150 kDa dextran was added to induce cell aggregation. Cartridge-2 was uniquely designed such that (i) the cells in the shallow section can be monitored

under microscope, (ii) the diluted sample gives satisfactory optical transmission in the deep section, and (iii) the disaggregating shear rates on the cells in both cartridge sections are the same.

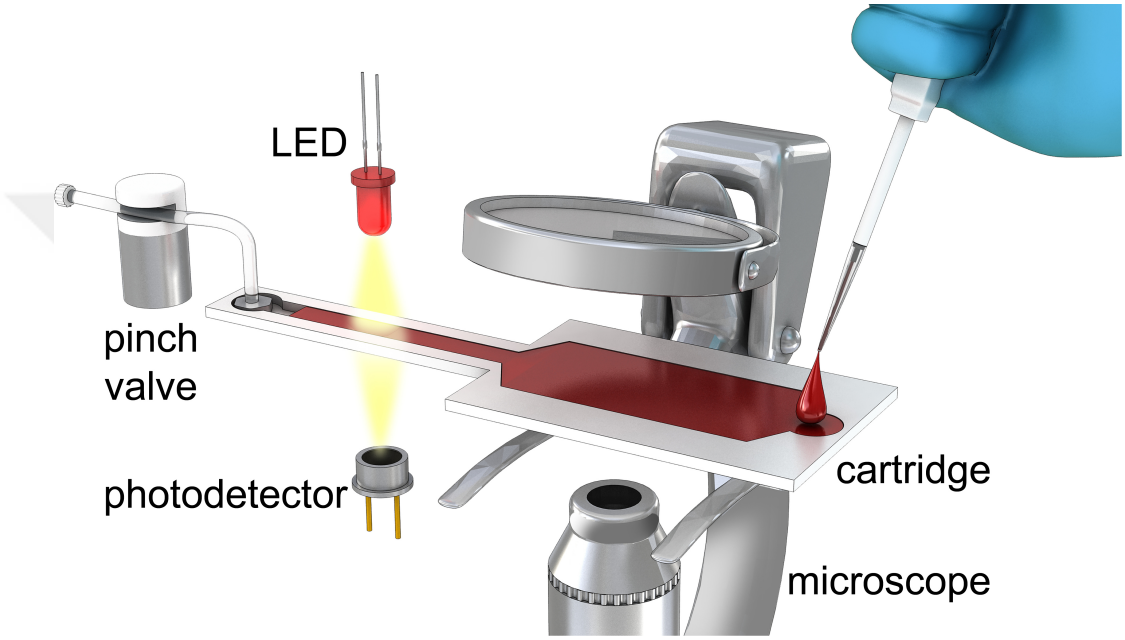


Figure 3.6: Schematic representation of the cartridge and simultaneous measurement method

200 μl of the prepared blood sample was introduced into the cartridge. After rigorous mixing of the sample, which achieves complete disaggregation as shown in Fig. 3.7 at time: 0 min, the cells were left intact for 6 min. During that time, the optically transmitted signal was measured in the deep section, and the erythrocyte aggregation process was video-recorded at the same time. In addition to the intensity-time curve, Fig. 3.7 gives time-lapse images taken from the recorded video. The time at which each image was taken has one-to-one correspondence with the intensity-time curve. At time: 0 min, the mixing was stopped, and the transmitted signal intensity was at its minimum when the cells were completely disaggregated. As time proceeded, the cells were shown to aggregate. At the beginning, aggregation was rapid and erythrocytes form bridges with the neighbouring cells. At time: 3 min, even though there are individual cells, most of the cells were clustered as aggregates. After time: 3 min, aggregates proceeded at a

much lower rate which is also confirmed by the intensity-time curve.

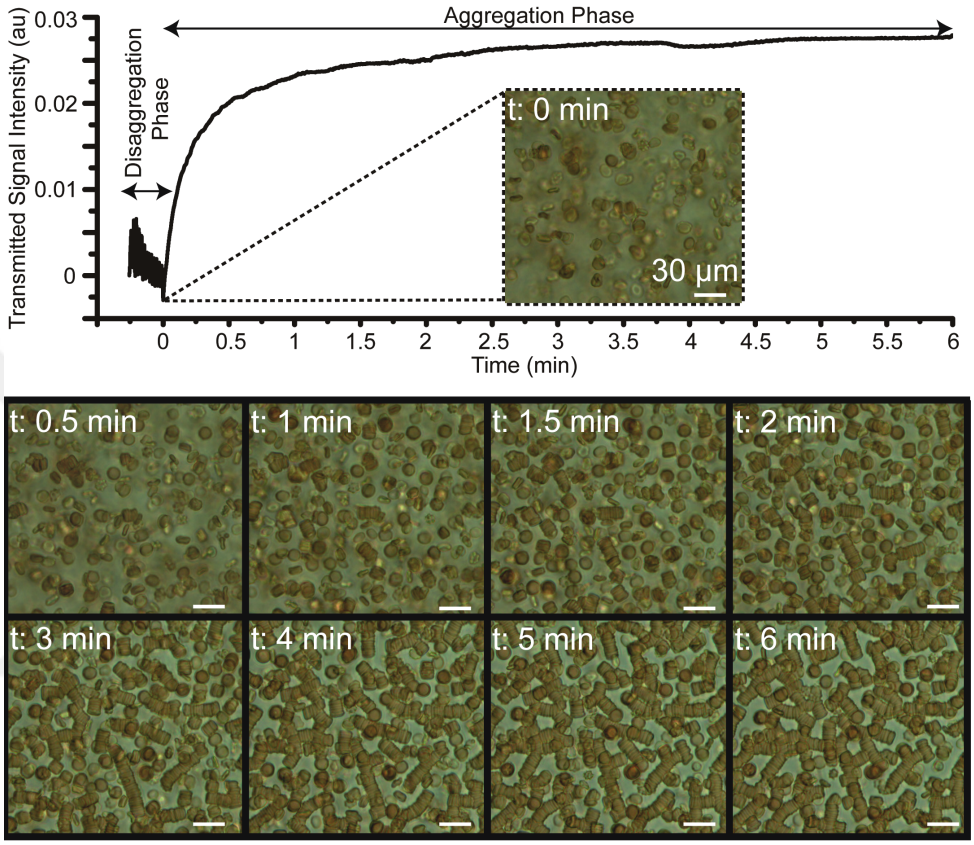


Figure 3.7: Simultaneous ESR measurement and EA monitoring with the microfluidic system. Pre-processed blood sample filled in cartridge-2, optical measurement taken from the deep section for 6 min after complete disaggregation. Erythrocyte aggregation process monitored in the shallow section for 6 min simultaneously as the ESR measurement. Plot showing the transmitted signal intensity measured for 6 min, and the time-lapse images of the aggregation process starting with complete disaggregation.

Although there are some studies in the literature that discuss the correlation between erythrocyte aggregation and sedimentation, none of these studies show the process in real-time. Also, a drawback of the commercial devices in the market was their potential incapability for succeeding complete disaggregation at the beginning of the assay [130]. The microscopic observations we made using cartridge-2 explains the correlation between erythrocyte aggregation and light

intensity change. At complete disaggregation, each cell becomes a scattering center, and their collective scattering results in less signal transmitting through the blood sample, leading to the lowest transmission intensity. During aggregation phase, the total area of the scattering centers decreases. This leads to more light passing through the microchannel, resulting in an increase of the transmitted signal intensity.

In whole blood, erythrocytes cannot be thought of as independent from the other blood constituents. There are many internal factors that affect the rate of erythrocyte sedimentation measured by the Westergren method. These include hematocrit level, plasma protein concentration, erythrocyte deformability, temperature, plasma viscosity and density [50, 130]. Some of these factors affecting the sedimentation might not affect the aggregation dynamics. For example, plasma viscosity has a major effect on the settling time of erythrocytes in the conventional system, but it has a minor effect in our system due to the fast measurement of the aggregation mechanism in a very small region of the cartridge. In contrast, erythrocyte deformability has a relatively minor effect in the conventional system, but it changes the aggregability of erythrocytes resulting in a major effect in our system. Since the microfluidic system that we developed measures the rate of EA and use it to predict ESR, some of these factors might be under or overestimated. This also explains the correlating coefficient of $R^2 = 0.86$.

On the other hand, there are several external factors influencing ESR results obtained by the Westergren method. These include (i) initial sample volume in the tube, (ii) tube vertical positioning, (iii) vibration, (iv) homogeneity of the sample at the beginning of the assay, (v) delay between venipuncture and measurement, (vi) manual reading of the result by the operator. Our microfluidic system addresses these shortcomings of the conventional method. (i) Measurement is performed at a single point along the sample channel. Cartridge-1 requires 50 μl of sample to fill the channel. Deviation from this amount does not affect the results if there is sample in front of the sensor during the test. (ii) Erythrocyte aggregation is not affected by the cartridge/analyzer orientation. (iii) The system is vibration-proof; carrying the system in hand during the measurement does not

affect the results. (iv) Homogeneity of the sample and complete disaggregation were ensured by sample mixing at the beginning of the test cycle. However, in the conventional assay, the operator should ensure sample homogeneity before placing the tube into the analyzer. (v) Since the system is portable and requires very small sample volume, the measurement can be carried out at the point-of-care without any delay. (vi) The system is a truly sample-in result-out system, thus eliminates operator mistakes.

3.4 Conclusion

In this chapter, we experimentally showed the correlation between ESR from EA. We explained the fundamental relationship between ESR and EA using Stokes' Law. Erythrocyte aggregates of large cell clusters lead to higher sedimentation velocity. This direct relationship was used for rapid measurement of ESR. The microfluidic system uses 50 μl whole blood and completes the test in 2 min. We measured the aggregation index, from the transmitted signal passing through the sample, which relates ESR to EA. The results were compared with the conventional Westergren method, and the microfluidic system showed high repeatability. We also showed the real-time observation of erythrocytes during ESR measurement using a unique cartridge geometry. Simultaneous ESR measurement and EA monitoring demonstrated one-to-one correspondence between the optical signal and the erythrocyte disaggregation and aggregation phases. The system was shown to eliminate the drawbacks of the Westergren method (operator-related problems such as tube shaking, sample volume, tube positioning, and result reading). The presented microfluidic system is a low sample volume requiring, low-cost, and portable system for ultrafast ESR measurement that can be used as a point-of-care unit.

Chapter 4

Determination of hemorheological properties using erythrocyte movements in a channel under damped oscillatory flow

Blood flow characteristics are determined mainly by erythrocyte deformation, aggregation, and sedimentation as well as blood/plasma viscoelasticity. These hemorheological properties are intricately interdependent and should be simultaneously monitored under numerous conditions including cardiovascular diseases. Current platforms lack the ability to quantify these properties all-at-once and in physiologically relevant conditions. In this chapter, we demonstrate that the microfluidic platform can be used for quantitative analysis of hemorheological properties from 50 μl undiluted blood inside a miniaturized channel. The assay is based on 3-min optical transmission analysis of collective erythrocyte dynamics, primarily deformation, under near-infrared illumination during damped oscillatory flow. This is a unique flow mechanism generated jointly by periodic pressure pulses and wetting effect.

4.1 Introduction

Hemorheology deals with non-Newtonian flow characteristics of blood in vascular networks [131]. The flow is determined by interdependent hemorheological properties [49]. Acquired or hereditary disorders affecting one property lead to alterations in others such as hyper-viscosity caused by anemia-originated decrease in erythrocyte deformation [98]. Storage-induced lesions like erythrocyte stiffness also cause severe complications following blood transfusion [132, 133]. Presently, hemorheological properties are rarely, if not at all, measured in clinics due to the drawbacks of using several benchtop equipment such as workforce, lab space, sample volume, operation time, and evidently cost. An all-at-once hemorheological measurement approach remains also elusive thus far in the microfluidics community. There are only a few studies analyzing two properties at a time based on image processing [134, 135]. This chapter addresses a microfluidic solution for the rapid analysis of multiple hemorheological properties without requiring cleanroom fabricated chips or microscopy setups.

Human erythrocytes are anucleated discoid cells of 5-8 μm diameter with viscoelastic membrane [44, 136]. Numerous pathological changes in erythrocyte membrane, skeleton, and interior cause stiffness that potentially results in capillary blockage (malaria, diabetes, sickle cell disease) [45, 137]. Most erythrocyte characterization methods focus on a single aspect of these cells. For instance, cell deformation is quantified by micropipette aspiration [138], atomic force microscopy [139], flow cytometry [140], and optical tweezers [141]. There is an extensive literature on microfluidic techniques for erythrocyte deformability. Operation principles of platforms include cell blockage [142], transit (velocity, margination, sorting) [143], and impedance analysis [144] for the characterization of malaria-infected or hardened erythrocytes. Despite the advantages of using microfluidics, these platforms have not yet found a ground in clinics possibly due to costly chip fabrication, prior blood processing (dilution), and the need for off-chip components such as pumps and microscopes. Blood consists of plasma and cells (mostly erythrocytes), and as such, is a shear-thinning viscoelastic fluid [52]. Blood viscosity is associated with diseases such as myocardial

infarction and hypertension [145]. Rheometers, viscometers, and recently various microfluidic techniques like co-flow analysis, advancing-meniscus monitoring, or impedimetric can be used for blood/plasma viscosity measurement [49]. Unlike viscosity, blood elasticity measurement is not a routine clinical practice. It was long believed that elastic behavior of blood originates solely from erythrocytes [146]. A recent study using a capillary breakup rheometer demonstrated the viscoelastic nature of plasma [59]. Nevertheless, the relationship between blood/plasma viscoelasticity and hemorheological disorders has not been entirely conceived and should be further elucidated. More specifically, a complete analysis of erythrocyte deformation, erythrocyte aggregation, and blood/plasma viscoelasticity could markedly increase safety of blood transfusion [147]. Erythrocytes of donated blood undergo hemorheological alterations during conventional 42-days cold storage (e.g., decreasing deformability, increasing viscosity) [148]. Hence, use of un-tested non-fresh blood causes potential complications including organ failure and mortality [149].

In this chapter, we propose a method for the analysis of multiple hemorheological properties from 50 μl blood in 3 min. The assay principle is based on optical transmission analysis of collective erythrocyte movements in a straight fluidic channel. The test starts off by sample introduction to the channel of a disposable polycarbonate cartridge. This is followed by repetitious 1-s reciprocating sample motions with gradually decreasing stroke distances, initiated by an integrated displacement pump. The sample is illuminated in the near-infrared band with a wavelength of 830 nm. To optically quantify erythrocyte deformation, transmission through the sample is recorded during flow. Medium viscosity, medium elasticity, and erythrocyte stiffness are varied to obtain blood samples with different hemorheological properties. These properties are swept once at a time, and the resulting optical signals are shown to be responsive to these hemorheological changes. The analysis is carried out in an environment that mimics vascular flow: confined, directional, pulsatile movement of blood at shear rates and hematocrit comparable to physiological levels.

4.2 Experimental

4.2.1 Materials and Characterization

Blood Collection. 10 ml fresh whole blood is acquired from a healthy male volunteer into a sodium citrate containing vacuum tube. The blood is centrifuged and washed three times with 1x PBS. **Suspending Medium Preparation.** (see Table 4.1) Blood plasma has a relaxation time of 0.1 ms. Hence, a plasma replacement medium with a relaxation time of 0.1 ms is prepared by dissolving 0.0085% Polyethylene oxide polymer (PEO; Mw = 600 kDa, Sigma-Aldrich) in 1x PBS. Glycerol (Sigma-Aldrich) is mixed with the plasma replacement at three concentrations (5%, 10%, 20% v/v) to obtain three mediums for viscosity analysis. PEO is dissolved in 1x PBS at three concentrations (0.05%, 0.1%, 0.2% w/v) to obtain three additional mediums for elasticity analysis.

Table 4.1: Summary of the rheological properties (η: viscosity and λ: relaxation time) of the suspending mediums.

Medium	Solvent	PEO in Solvent (w/v)	η [mPa.s]	λ [ms]
medium 1	5% Glycerol-95% PBS	0.0085%	0.98	0.099
medium 2	10% Glycerol-90% PBS	0.0085%	1.14	0.099
medium 3	20% Glycerol-80% PBS	0.0085%	1.53	0.099
medium 4	100% PBS	0.05%	1.40	0.312
medium 5	100% PBS	0.1%	1.57	0.490
medium 6	100% PBS	0.2%	2.41	0.768

Blood Sample Preparation. Six different blood samples (H-samples 1-to-6; H for healthy) are prepared by suspending healthy erythrocytes (47% v/v) in the mediums 1 to 6, respectively. To obtain erythrocytes with stiffened cell membranes, healthy erythrocytes suspended in 1x PBS (47% v/v) are treated with 0.025% v/v glutaraldehyde (GA) solution, which was prepared in 1x PBS from

a 25% w/v stock GA (Sigma-Aldrich). Then, six additional blood samples (S-samples 1-to-6; S for stiffened) are prepared by suspending stiffened erythrocytes (47% v/v) in the mediums 1 to 6, respectively. **Rheological Measurements.** A rotational rheometer (MCR 301, Anton Paar) is used for the viscosity measurement of the six suspending mediums. The measuring unit has 50 mm diameter cone plate geometry (CP50-1). Constant shear rate mode is chosen, and the temperature is set to 25°C. 760 μl sample is used for each measurement. The shear rate is swept from 10 to 1000 s^{-1} (Fig. 4.1). Relaxation times of the suspending mediums are calculated using the Zimm estimation. All rheological values are given in Table 4.1.

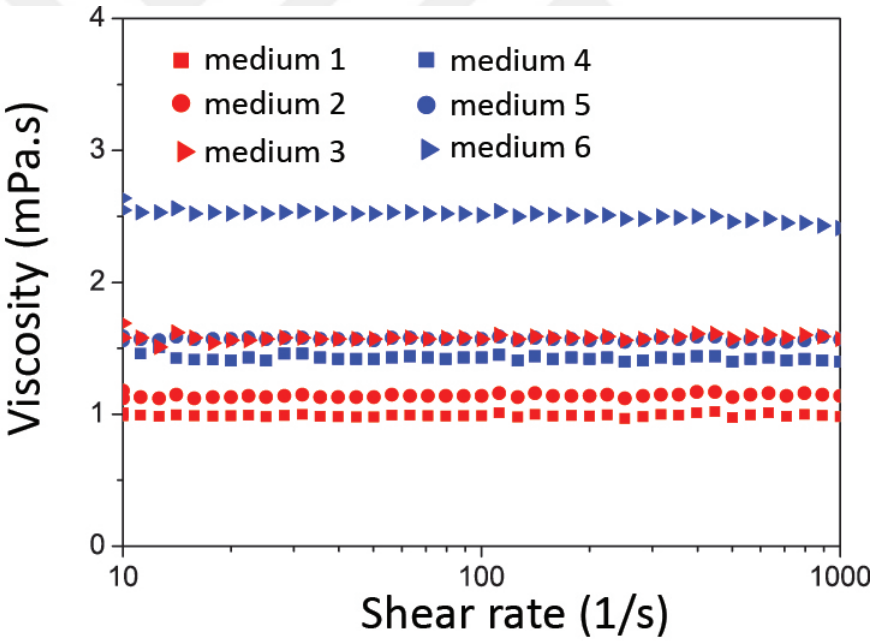


Figure 4.1: Suspending medium viscosity as measured by the rotational rheometer.

Pump Characterization. The pressure generated by the pump is characterized using a pressure sensor (40PC015 G, Honeywell). A silicone tubing is connected to the pump, and the pressure is recorded and sampled using a data acquisition card (DAQPad-6015, National Instruments). **Image Analysis.** A 1-s video recording of the blood sample inside a channel is taken using an inverted optical microscope (Zeiss Axio Vert) equipped with a high-speed camera

(Phantom Miro 2) at 2.5x magnification. The recording rate is 2800 frame per second. Images are obtained from the video using the camera software.

4.2.2 Measurement Platform

We used the same platform as in Chapter 2 but replaced the pinch valve with another displacement pump. Following 50 μl sample introduction into the channel and cartridge insertion into the printed cartridge holder, an airtight fluidic connection is made between the channel outlet and the pump. With the start of the test, the pump mechanically moves an actuator pin forward and backward with 0.5 s^{-1} frequency for a duration of 14 s. Each forward pin movement generates 12.5 mbar pressure driving the sample forward inside the channel with 5 mm stroke distance and initiates a 1-s damped oscillatory flow. Meanwhile, an 830-nm wavelength near-infrared light-emitting diode (LED; Vishay) illuminates the blood sample, and an NPN photodetector (Vishay) collects the transmitted light. Deformation reduces erythrocytes' surface area to volume ratio giving photons more space to pass through [67, 150]. Therefore, compared to the case where all erythrocytes are arbitrarily suspended in the channel, transmission intensity is higher when the erythrocytes are at shear flow and deformed. Hence, we optically quantified erythrocyte deformation during flow by measuring the transmission intensity (I_c [mA]) collected by the phototransistor. The photodetector current output passes through an analog circuit consisting respectively of a transimpedance amplifier, a lowpass filter, and amplifying differentiator to get a voltage output (V_{out} [mV]) such that

$$V_{out} = C_1 - C_2 \frac{dI_c}{dt} \tag{4.1}$$

where C_1,C_2 are constants. The resulting signal is analyzed using MATLAB (R2018, MathWorks).

4.3 Results and Discussion

4.3.1 Optical Analysis of Collective Erythrocyte Movements in a Fluidic Channel

During the test, the displacement pump moves the actuator pin forward and backward for 14 s. Figure 4.2a graphs the pressure generated by the pump during one pump period (T = 2 s). The pump action consists of a 1-s push and a 1-s pull states. At the start of the cycle (t_0), the pin is in contact with an elastic membrane making an airtight connection to the channel outlet. In the push state, the pin pushes the membrane inward for 60 ms compressing the air within the system to generate an increasing pressure with a maximum value of 12.5 mbar at t_1. Following t_1, the pressure decreases and finally attenuates to zero at the end of 1 s (t_4). For the push state (t_0 to t_4), the initial pin movement (t_0 to t_1; Δt_1=60 ms) initiates a 1-s oscillatory flow of the sample within the channel. In the pull state, the pin withdraws for 60 ms (t_4 to t_5), letting the membrane retract to its undeformed position and generating a decreasing pressure with a minimum value of -12.5 mbar at t_5.

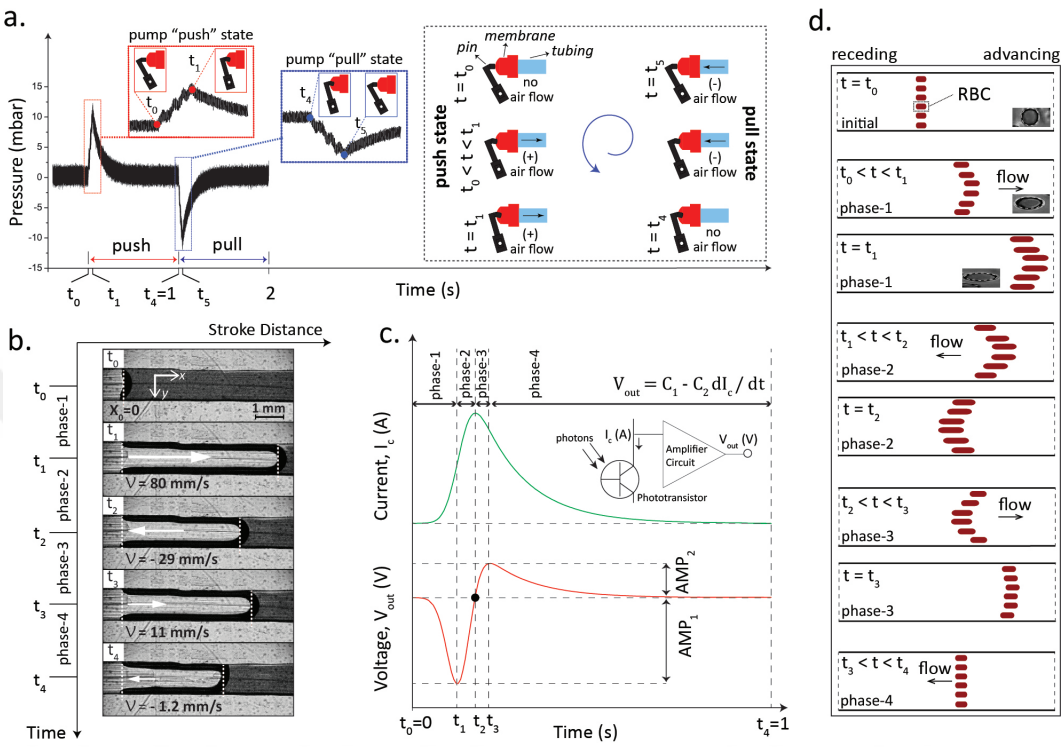


Figure 4.2: **a.** Pump characterization. Pressure generated by the pump during one period (2 s) comprising a 1-s push state and a 1-s pull state. **b.** Side-view images of a 1-s oscillatory flow from a high-speed camera recording. The observation window is near the receding edge for easier comparison for different phases. Stroke distances and velocities are displayed on images. **c.** Output signals measured by the device during 1-s oscillatory flow. Current signal measured directly from the phototransistor output and voltage signal measured as the output of the analog amplifier circuit fed by the current signal. Both signals are divided into four distinct phases. **d.** Schematic cross-sectional side-view model of collective erythrocyte movements during a 1-s oscillatory flow. Microscopy images demonstrate the progression of a single erythrocyte deformation during shear flow.

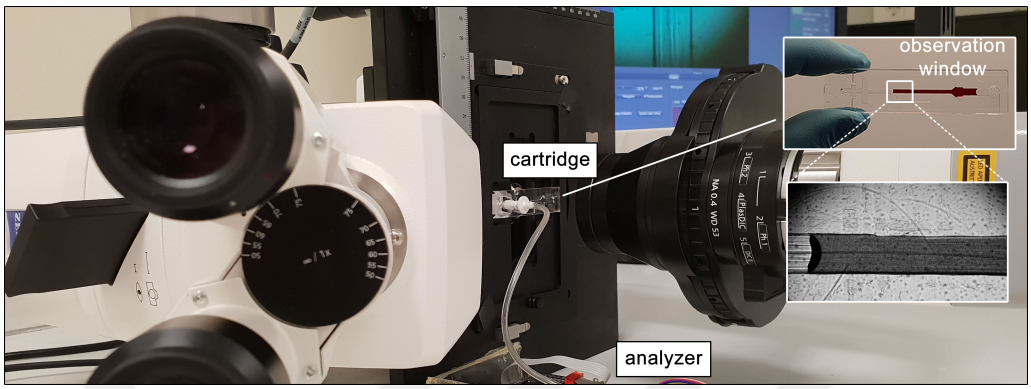


Figure 4.3: Customized microscopy setup to get side-view video recording of the blood sample flow inside the channel. Observation window near the sample receding edge is demonstrated.

A microscope is used to get side-view video recording of the blood sample flow inside the channel (Fig. 4.3). Figure 4.2b shows the side-view images of a 1-s oscillatory flow during a push state at an observation window near the channel receding edge. The sample is stationary at t_0. Then, the pin pushes the adaptor for 60 ms, driving the sample forward reaching a stroke distance of 5 mm at t_1 (Δt_1=60 ms). During this bulk motion, a small layer of fluid remains attached to the channel walls due to adhesion between the walls and fluid. Hence, although the pin stops at t_1, the bulk fluid moves backward for 1 mm until t_2 (Δt_2=42 ms) because of the cohesive forces between the fluids on the wetted walls and bulk. Again, the wetting on the advancing edge (not shown) causes a small forward flow until t_3 (Δt_3=36 ms). Finally, the fluid moves backward very slowly (mean velocity: 1.2 mm/s) for 860 ms until t_4. There are apparently four phases of sample flow. The sample has a different velocity in each phase. This results in different wall shear rates (phase-1: $480s^{-1}$; phase-2: $174s^{-1}$; phase-3: $66s^{-1}$; phase-4: $7.2s^{-1}$) calculated using equation (4.2) where $\dot{\gamma}$ and Q are wall shear rate and flow rate, respectively.

$$\dot{\gamma} = \frac{6Q}{wh^2} \tag{4.2}$$

Microscopic images of the oscillatory flow in Fig. 4.2b indicate the differences

in wall shear rates for each phase. Shear rate determines the shear stress experienced by erythrocytes that, as a result, deform to accommodate the stress. Changes in collective erythrocyte deformations are optically recorded by the microfluidic device as the light transmits through the blood sample. Figure 4.2c illustrates the current signal measured directly from the phototransistor during a 1-s oscillatory flow as well as the corresponding voltage signal obtained as the output of the optical detection unit. As in Fig. 4.2b, the current signal also consists of four distinct phases. The signal is concave-up with an increasing positive slope (phase-1), followed by the continuation of the rise with a decreasing slope (phase-2). After t_2 where the current is at maximum, the signal is concave-down with a decreasing negative slope (phase-3), and it goes back to the initial level (phase-4). The distinction between these phases is more pronounced in the voltage signal. The voltage signal makes two peaks ($AMP_{1,2}$) at the end of phase-1 and phase-3, respectively. It has the zero crossing when the current is at maximum (t_2), and it settles down to initial voltage level at the end of phase-4 (t_4).

Dense population of erythrocytes in the channel, as a result of the clinically relevant erythrocyte volume fraction and the channel depth, hinders the observation of individual erythrocytes under a microscope. Based on the microscopic observation of the bulk sample shown in Fig. 4.2b and the corresponding optical transmission analyses in Fig. 4.2c, a 1-s four-phase oscillatory flow is schematically summarized in Fig. 4.2d. Phase-0: (t=t_0) Erythrocytes are suspended in the medium. Phase-1: (t_0<t<t_1) Sample moves forward. Erythrocytes align with the Poiseuille flow and deform longitudinally in response to increasing shear stress. Current level increases since deformation allows more light transmission. (t=t_1) Pump pressure is at maximum. Erythrocytes have the largest forward deformation. Voltage output makes a peak, AMP_1. Phase-2: (t_1<t<t_2) Wetting effect on the receding edge moves the sample backward. Erythrocytes align with the flow and deform longitudinally. Current level increases due to erythrocyte deformation. Shear stress generated by wetting effect (0.15 Pa) is smaller than stress generated by the pump (0.43 Pa). Therefore, deformation is smaller at t_1<t<t_2 than t_0<t<t_1. (t=t_2) Erythrocytes have the highest backward deformation. Voltage output reaches the zero crossing. Phase-3: (t_2<t<t_3) Wetting

effect on the advancing edge moves the sample forward. Erythrocytes start to retain their original shape due to fading shear stress. Current level decreases when the deformation decreases. Phase-4: (t_3<t<t_4) Erythrocytes move backward very slowly until their complete stop and shape recovery at t=t_4. Current level gradually falls to the initial level.

4.3.2 Change in Medium Properties

Viscoelastic plasma is a suspending medium for erythrocytes, and medium rheology is a key determinant of blood flow. Specifically, medium viscoelasticity determines the generation of viscous and elastic stresses applied on erythrocytes, thereby determining erythrocyte deformation during flow. Viscous stresses facilitate erythrocyte deformation whereas elastic stresses suppress it. Hence, an increase in medium viscosity or a decrease in medium elasticity enhances deformation [151, 152]. We prepared suspending mediums with different viscoelastic properties (Table 4.1). Firstly, three mediums are prepared using varying concentrations of glycerol in the plasma replacement (mediums 1, 2, and 3). Using these mediums, three blood samples (H-samples 1, 2, and 3) are prepared from healthy, deformable erythrocytes (47% v/v). Figure 4.4a shows the optical measurements for these samples. Secondly, three mediums are prepared using varying concentrations of PEO in PBS (mediums 4, 5, and 6). Figure 4.2b compares the optical signal parameters (AMP_1, t_2, and AMP_2) with the glycerol concentration. $AMP_{1,2}$ increase with the increasing medium viscosity while t_2 remains the same. As demonstrated in Fig. 4.2b, in phase-1, the pump generates an increasing pressure to drive the sample forward. In the meantime, shear stress (τ) applied on erythrocytes deforms the cells. Given that the shear rate ($\dot{\gamma}$) is a function of flow rate (Q) and the same for all the samples during phase-1 (equation (4.2)), an increase in medium viscosity (η) increases shear stress as followed by

$$\tau = \eta\dot{\gamma} = \eta\frac{6Q}{wh^2} \tag{4.3}$$

The increasing shear stress in return deforms erythrocytes more and eventually

increases light transmission and AMP_1. Therefore, given the same elasticity, the more viscous the medium, the higher the AMP_1 value.

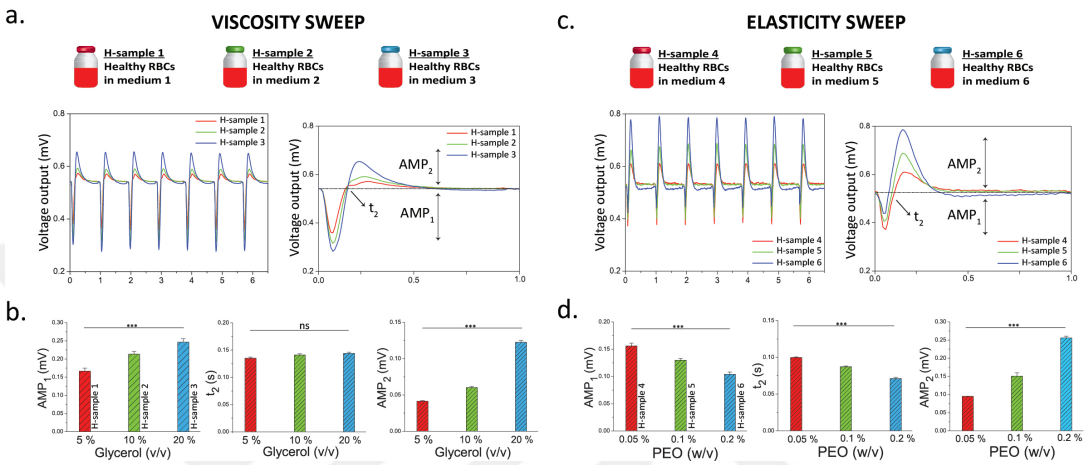


Figure 4.4: Effect of suspending medium viscoelasticity on optical transmission signals. Each plot consists of seven repetitive signals (a and c left) that are averaged (a and c right) for the following samples: Healthy erythrocytes suspended in **a.** Mediums with different glycerol concentrations and **c.** Mediums with different PEO concentrations. Comparison of the optical signal parameters with **b.** the glycerol concentration and **d.** the PEO concentration. One-way ANOVA test was used for comparison. The significance is displayed on graphs where *** for $p<0.001$ and ns for $p>0.5$.

Pressure is the dominant factor in determining the flow rate in phase-1 and phase-2, given the short time scales of these phases (Δt_1=60 ms, Δt_2=40 ms). Hence, t_2 only negligibly increases with the increasing medium viscosity.

Erythrocytes are in deformed state at t_2. During phase-3, they lose their deformation due to fading shear stress (Fig. 4.2b), and they partially recover their undeformed shape at t_3. The more viscous the medium, the higher the stress change (equation (4.3)). This consequently results in higher deformational change leading to higher intensity change. Hence, higher AMP_2 is measured in higher viscosity mediums.

Figure 4.4c shows the optical measurements for the samples again with healthy

erythrocytes (H-samples 4, 5, and 6). Figure 4.4d compares the parameters with the polymer concentration. AMP_1 and t_2 decrease with the increasing medium elasticity while AMP_2 increases. The relative importance of elastic and viscous forces of a viscoelastic medium can be represented by the Weissenberg number (Wi) as [153]

$$Wi = \lambda\dot{\gamma} \tag{4.4}$$

There are non-linear elastic forces in a viscoelastic fluid expressed in terms of normal stress differences, predominantly the first normal stress (N_1) that increases with polymer concentration [154]

$$N_1 = 2\eta\lambda\dot{\gamma}^2 \tag{4.5}$$

N_1 induced in the flow is at normal direction to the erythrocyte membrane [155, 156], and the existence of N_1 suppresses erythrocyte deformation during phase-1. Therefore, AMP_1 decreases with the increasing polymer concentration.

t_2 is different for each sample. The polymers are stretched by the stress generated in phase-1, and they store elastic stress, the magnitude of which is proportional to polymer concentration. They discharge this energy and relax in phase-2 (viscoelastic recovery). More elastic samples recover their initial state faster, explained by the creep-recovery response of the Kelvin model as

$$\varepsilon(t) = Ce^{-(E/\eta)}t \tag{4.6}$$

where ε, E, η, and C are strain, sample elasticity, sample viscosity, and initial-state constant, respectively. Therefore, t_2 is the lowest at the highest polymer concentration, namely highest E [60].

The effective relaxation times for all the mediums are less than 1 ms (Table 4.1), so the polymers are already relaxed prior to phase-3. Therefore, the mediums act only viscous (Newtonian) in phase-3. As in the previous discussion for AMP_2 in Fig. 4.4b, AMP_2 increases with the increasing medium viscosity.

Having demonstrated the relationship between the optical parameters and the medium viscosity (Fig. 4.4b) or medium elasticity (Fig. 4.4d), governing equations relating individual optical parameters to overall medium viscoelasticity can be derived using the viscosity (η_{medium}) and relaxation time (λ_{medium}) values presented in Table 4.1. Figure 4.5a compares $k_1 = [\eta_{medium} \ / \ \lambda_{medium}]$ to optically measured AMP_1, and Fig. 4.5b compares $k_2 = [\eta_{medium}]$ to AMP_2 (recalling that all mediums act only viscous in phase-3). Using the regression analysis, two linear equations are obtained

$$k_1 = \frac{\eta_{medium}}{\lambda_{medium}} = aAMP_1 + b \tag{4.7}$$

$$k_2 = \eta_{medium} = cAMP_2 + d \tag{4.8}$$

where a, b, c, and d are constants with the values of 93.1, -7.8, 6.3, and 0.7, multiplied by 10^{-3}, respectively. This analysis implies that using these equations and the parameters obtained from an optical measurement, medium properties can be calculated as an alternative to conventional rotational rheometry. In addition, since AMP_1 and AMP_2 are measures of erythrocyte deformation, if medium properties are already known, these parameters can be employed to obtain the deformation during flow.

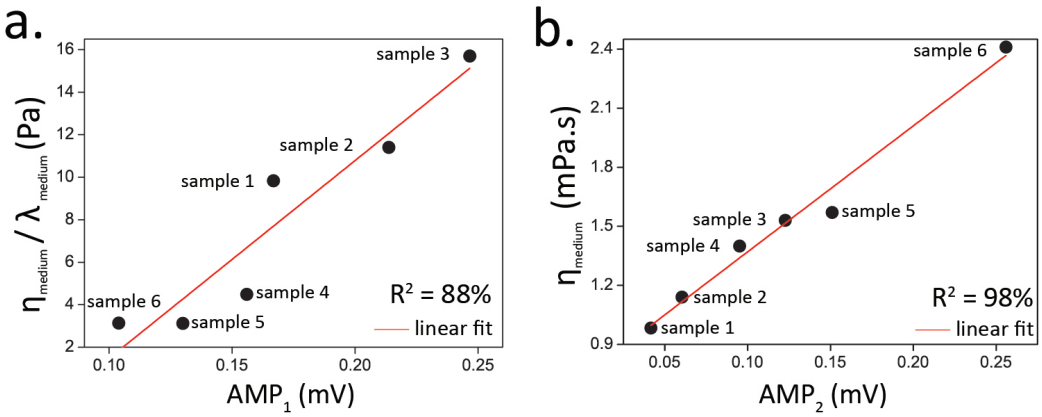


Figure 4.5: Comparing optical signal amplitudes to medium properties for the six blood samples with healthy erythrocytes. **a.** The scatter plot and the linear fit comparing AMP_1 to k_1. The correlation is 88% using linear regression. **b.** The scatter plot and the linear fit comparing AMP_2 to k_2. The correlation is 98% using linear regression

4.3.3 Change in Erythrocyte Membrane Stiffness

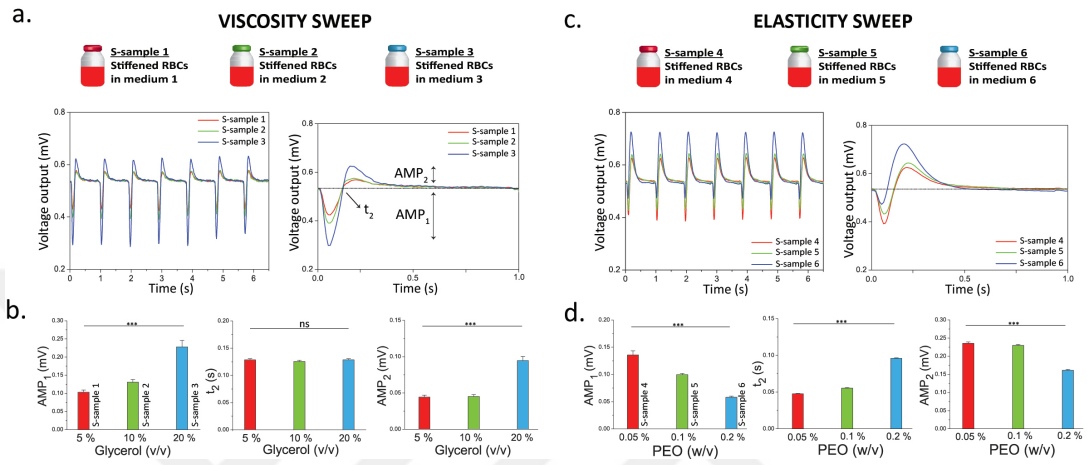


Figure 4.6: Effect of suspending medium viscoelasticity on optical transmission signals. Each plot consists of seven repetitive signals (a and c left) that are averaged (a and c right) for the following samples: Stiffened erythrocytes suspended in **a.** Mediums with different glycerol concentrations and **c.** Mediums with different PEO concentrations. Comparison of the optical signal parameters with **b.** the glycerol concentration and **d.** the PEO concentration. One-way ANOVA test was used for comparison. The significance is displayed on graphs where *** for $p<0.001$ and ns for $p>0.5$.

Healthy erythrocytes are deformable due to the viscoelastic membranes that enclose the cellular interior. Numerous clinical conditions such as malaria can decrease erythrocyte deformability. We prepared six blood samples (S-samples 1-to-6) by suspending glutaraldehyde-fixed stiffened erythrocytes inside the six suspending mediums. Figure 4.6 shows the optical measurements for these samples. The trends seen for the H-samples in Fig. 4.4b-d are also observed for the S-samples in Fig. 4.6b-d for the same reasons. Briefly, given the same elasticity, $AMP_{1,2}$ increase with the increasing medium viscosity while t_2 remains the same (Fig. 4.6b). Also, $AMP_{1,2}$ decrease with the increasing medium elasticity while t_2 increases. We expect that stiffened erythrocytes deform less than healthy erythrocytes (Fig. 4.6d). It is also confirmed in Fig. 4.7 where AMP_1 and AMP_2 are lower for the S-samples at a given $[\eta_{medium}\ /\ \lambda_{medium}]$ or $[\eta_{medium}]$ due to

compromised deformability of stiffened erythrocytes.

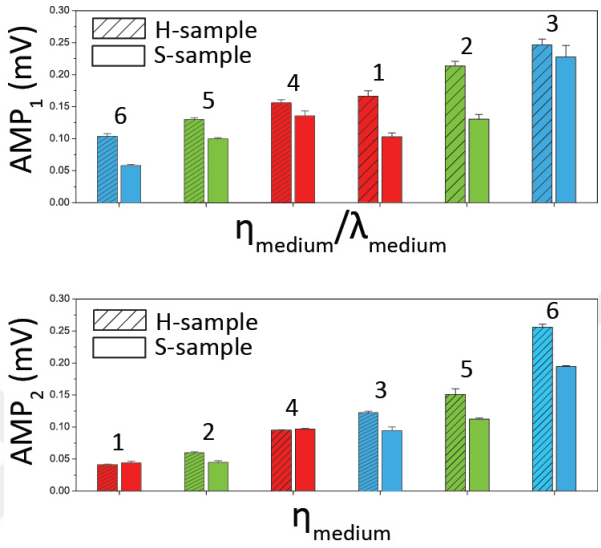


Figure 4.7: Comparing optical signal amplitudes of an H-sample and S-sample at a fixed medium property; [η_{medium} / λ_{medium}] or [η_{medium}]. The integers displayed on the bars signify the sample number (e.g., H-sample 6 and S-sample 6) **a.** Comparing AMP_1 at a k_1 = [η_{medium} / λ_{medium}] value. **b.** Comparing AMP_2 at a k_2 = [η_{medium}] value.

4.4 Conclusion

We presented a measurement method for the determination of multiple hemorheological properties from undiluted blood. The operation principle is based on 3-min optical transmission analysis of collective erythrocyte movements in a straight single channel under infrared illumination. A unique four-phase damped oscillatory flow mechanism was generated jointly by a displacement pump and wetting effect. The analyses were performed in a miniaturized environment that mimicked vascular flow. Optical transmission through the blood sample was recorded during the flow to quantify erythrocyte deformation. Blood samples with different medium viscoelasticity and erythrocyte stiffness were employed to experimentally demonstrate that viscous stresses facilitate erythrocyte deformation and

elastic stresses suppress it. This novel technique has a potential to remove the financial and practical drawbacks associated with the state-of-the-art hemorheological analysis. Such a sample-in result-out microfluidic approach can eventually make hemorheological monitoring accessible in clinics and research labs even in resource-poor setting.

Chapter 5

Coagulation time measurement from erythrocyte aggregation

Coagulation, the process leading to clot formation with the interplay of blood constituents, is a self-regulating mechanism, requiring attentive and periodic monitoring for numerous clinical cases. Erythrocyte aggregation (EA) is a characteristic behavior of erythrocytes forming reversible clumps especially in vitro at low shear rates. The effect of EA during coagulation is overlooked in whole blood (WB) clotting assays, and the relationship between the two mechanisms is not well understood. We employed our microfluidic platform for quantitative investigation of EA from 50 μl WB during the coagulation process. In this chapter, not only did we explain the coagulation mechanism considering EA, but we also demonstrated coagulation time measurement from optical EA analysis. The platform consists of a new cartridge and the same analyzer containing a pinch valve for fluid motion. Following the sample introduction and cessation of the valve operation, the optical signal is the lowest due to shear-induced cell disaggregation. Then, the signal increases due to EA until reaching a peak, indicating blood clotting. The working principle was proven through clinical tests for prothrombin time measurement. In addition to revealing the relation between coagulation and aggregation, this device was shown to be promising for rapid WB coagulation time measurement.

The content of this chapter was published in [157] as;

Z. Isiksacan, N. Hastar, O. Erel, and C. Elbuken, An optofuidic point-of-care device for quantitative investigation of erythrocyte aggregation during coagulation, Sensors and Actuators A: Physical, vol. 281, pp. 24-30, 2018.

5.1 Introduction

Blood coagulation is a process involving the interaction of various plasma proteins, coagulation factors, and platelets to eventually form stable fibrin strands for the prevention of hemorrhage [158]. This process consists of two pathways, named intrinsic and extrinsic, which are triggered by different activators, but lead to a common pathway (Fig. 5.1). The common pathway ends with the conversion of fibrinogens into fibrin clots [159]. In vitro measurement of coagulation time is required for individuals who are under operational evaluation [160, 161]. Also, patients who are diagnosed with or have the risk for coagulation disorders, embolism, stroke, heart attack, and other cardiovascular diseases (CVD) need coagulation time measurement [162, 163]. Anticoagulant therapy, the prescription of blood-thinning medication, is the common strategy to combat coagulation related disorders and to regulate clotting status of patients [164]. The traditional approach for coagulation time monitoring is the use of benchtop instruments in clinical settings. This necessitates periodic hospital visits, which is generally costly and time-consuming. It is even potentially life-threatening if hospital visit is delayed. This is especially a concern for patients receiving anticoagulant therapy as the medications have narrow therapeutic windows.

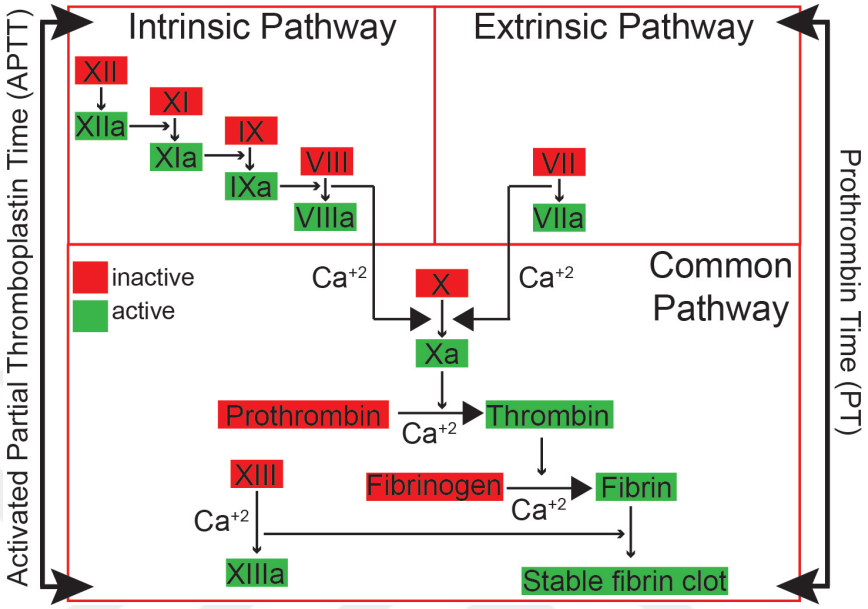


Figure 5.1: Coagulation cascade

The use of point-of-care (POC) technologies for coagulation time measurement aims to alleviate the drawbacks of the conventional equipment [1]. There are portable coagulation analyzers in the market that facilitate self-monitoring and reduce turnaround times [165]. These devices employ various measurement principles such as optical (e.g., detection of change of particle oscillation frequency by light reflection), mechanical (e.g., viscosity change detection by cantilever or magnet position), or electrochemical (e.g., amperometric detection using substrate molecules) [166]. From a finance point of view, the high price tag for both the main device (purchased once) and the disposable test cartridges (purchased repeatedly; generally having complicated fabrication) is a drawback. Health insurances in many countries including Turkey do not cover the purchase of such costly equipment for home use. This places such devices beyond the reach of many people who, therefore, visit hospitals/anticoagulation clinics for periodic tests. There are also studies in the literature using microsystems technology for coagulation time measurement. Examples include paper-based [167], cantilever-based [168], impedimetric [169], quartz crystal microbalance (QCM) [170], surface

plasmon resonance (SPR) [171], migration distance-based [172], and elastometry-based [173]. The practical issues associated with these studies are limited quantitative measurement, dependence to cleanroom fabrication, need for electronic integration, set-up complications, necessity for plasma separation, standardization, and viscosity dependency, respectively, hindering their adaptability as common techniques. The two biological samples analyzed with these platforms are whole blood (WB) and plasma. The use of WB for coagulation assays offers ease-of-use, low sample requirement, and short turnaround times in comparison to the use of plasma. On the other hand, current WB coagulation assays fall short of understanding the effect of erythrocyte aggregation (EA), which is an inherent mechanism affecting the assay kinetics. Herein, we explored this intricate relationship between coagulation and EA using a real-time optical analysis device.

Erythrocytes constitute reversible face-to-face aggregates under stationary conditions or at low shear rates in blood. The aggregation of erythrocytes is governed by cellular surface properties (e.g., surface charge), plasma protein concentrations (e.g., fibrinogen), and shear rate that can disaggregate the cell clumps once applied above a threshold. Several attempts have previously been made to monitor coagulation through the aggregation phenomenon [174–177]. However, the fundamental mechanisms for the relationship between coagulation and aggregation have remained unclear, and the studies lacked clinical verifications.

In this chapter, we reported the use of our microfluidic platform for the optical analysis of the EA kinetics during the coagulation process. The device is employed for two main purposes: (i) measuring coagulation time from a drop of WB (50 μl) in less than 2 min using EA and (ii) demonstrating the presence/effect of EA in a coagulating blood to understand the fundamental relationship between these two mechanisms. The device is used for prothrombin time (PT) measurement. The measurement principle is based on the optical investigation of EA during coagulation by illuminating the blood sample with near-infrared light and recording the transmitted light intensity. We explained the interrelation between these two physiological phenomena, coagulation and EA, which have long been studied independently of each other. Microscopy observations during the coagulation

provided in-depth understanding of the actual physical correspondence of the optical measurement signals, supporting the results obtained from our platform. In addition, the clinical tests allowed comparison of the device with a conventional benchtop equipment, which showed the potential of the study beyond research laboratories.

5.2 Experimental

5.2.1 Sample Preparation

21 volunteers (11 males, 10 females) were chosen, ensuring that a wide PT range was covered. 3 ml venous WB was acquired from the volunteers into sodium citrate containing vacuum tubes, and all the experiments were performed at 37 °C within the same day of blood draw. The benchtop equipment available in the hospital for the conventional measurements was Sysmex CA-1500 System (Siemens, Germany). Thromborel S Human Thromboplastin (Siemens, Germany) reagent was used for the PT tests. 7.6 mg Thromborel S Human Thromboplastin is dissolved in 100 μl deionized (DI) water by gentle mixing at 24 °C. 25 μl dissolved reagent is pipetted into the cartridges which are then kept at -80 °C for 2 h. The reagents in the cartridges are then lyophilized in a freeze-dryer (Labconco, US) for 6 h. Following, the cartridges are stored at 4 °C with a desiccator and used within 6 h.

Human fibrinogen conjugate labeled with Alexa Fluor 488 (Molecular Probes, US) was prepared by reconstituting the supplied sample in 0.1 M sodium bicarbonate (pH 8.3) at room temperature. The stock solution is divided into aliquots and stored at -20 °C. Prior to use, the solution is brought to room temperature. The required amount (1 μl, 2 μl, 3 μl, or 4 μl) is then gently mixed with 100 μl WB and kept intact at room temperature for 30 min.

70 kDa dextran is purchased from Sigma-Aldrich and stored at room temperature. Three microcentrifuge tubes are filled with 200 μl WB. To prepare WB

samples with 5 mg/ml, 10 mg/ml, and 15 mg/ml dextran concentrations, 1 mg, 2 mg, and 3 mg dextran are added to the tubes and dissolved by gentle mixing.

5.2.2 Cartridge Fabrication and Measurement Platform

The cartridges presented in Chapters 2, 3, and 4 consisted of a 1 mm deep, 1 mm wide, and 50 mm long straight channel, with an inlet and outlet. In this work, we again had a single channel cartridge with 1 mm depth and 50 mm length. This time, we fabricated narrowing-expanding sections on one half of the channels to facilitate the mixing of the blood sample with the coagulation activator (Fig. 5.2a). The coagulation activator was lyophilized in the other half of the channel.The same measurement platform presented in Chapter 2 was used. In addition to the disaggregation of the cell clusters, the pinch valve motions allow homogenous mixing of the blood sample with the coagulation activator reagent lyophilized in the cartridge.

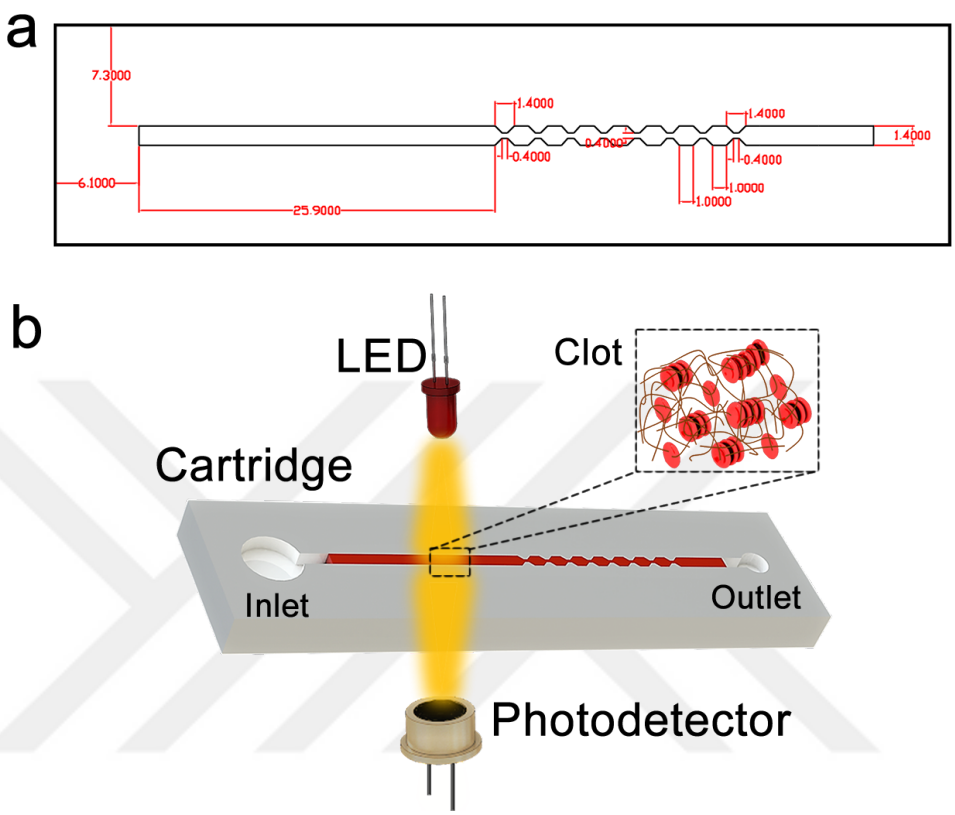


Figure 5.2: Channel with constriction regions. **a.** AutoCAD drawing of the cartridge. **b.** Schematic drawing of the measurement platform.

5.3 Results and Discussion

5.3.1 Optical Analysis of Erythrocyte Aggregation

A cartridge takes 50 μl citrated WB that starts to coagulate only when mixed with an activator reagent. The initial experiment was carried out using citrated WB without using any reagent in the cartridge. Following the introduction of the blood sample to the channel, the solenoid pinch valve was operated for 10 s to completely disaggregate the erythrocyte clusters. Then, the valve operation was terminated to let the erythrocytes re-aggregate. During this re-aggregation process, the LED illuminated the blood sample while the photodetector measured

the intensity of the transmitted light. The black signal profile in Fig. 5.3a shows the measured signal intensity for this case. At the end of the pinch valve operation (time: 0^{th} s), the erythrocytes are all dispersed. Since each individual cell serves as a scattering source, the intensity is at the lowest. As time progresses, erythrocytes aggregate, and, therefore, the signal intensity increases until complete aggregation of the erythrocytes. With the complete aggregation, the signal intensity stays constant.

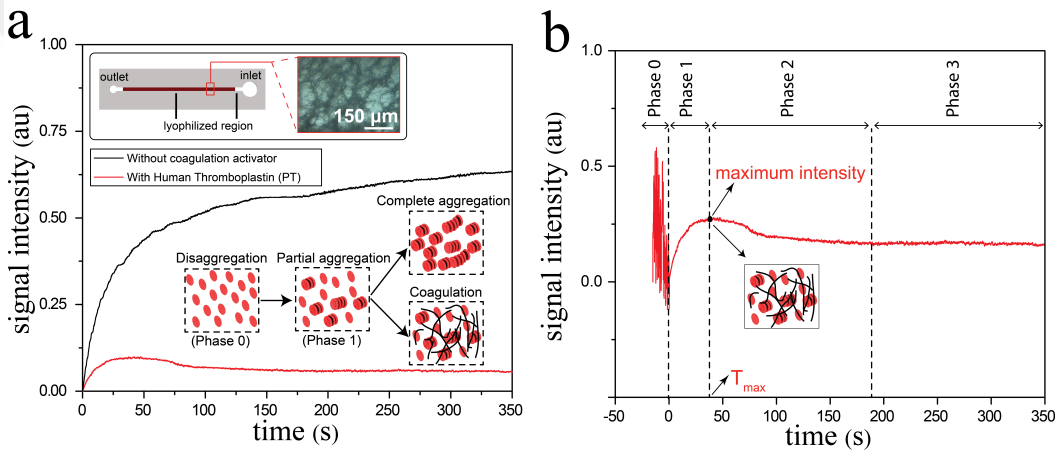


Figure 5.3: **a.** Measurement of the transmitted signal intensity of the whole blood sample using the coagulation platform when the cartridge was tested without an activator reagent and with PT reagent. The inset shows the schematic cartridge and a photography of the lyophilized reagent within the channel. **b.** The transmitted signal intensity when human thromboplastin was lyophilized prior to the test. The signal profile is divided into four phases, and the maximum intensity level corresponds to the coagulation time.

The coagulation cascade consists of an intrinsic and an extrinsic pathway directing to a common pathway that ends with the formation of fibrin clots. The latter is triggered by tissue factor, and prothrombin time (PT) is used for the evaluation of the extrinsic pathway. Human thromboplastin was lyophilized in a cartridge to trigger the extrinsic pathway for PT measurement. Figure 5.3a also shows the measured signal intensity for this case (red signal). Here, the signal intensity increases until a maximum value and decreases back. On the other hand,

for the cartridge without any activator reagent, the signal intensity continuously increases due to the aggregation of erythrocytes (black signal). It should also be noted that the absorption/transmission spectra of both the coagulating and non-coagulating WB are determined by the erythrocytes in the near-infrared band. It, therefore, implies that the coagulation process affects the aggregation of the erythrocytes, which can optically be observed from the recorded signal profile.

Figure 5.3b shows the signal profile obtained when human thromboplastin is lyophilized in the cartridge. This signal is divided into four distinct phases. The initial phase corresponds to the 10 s-long valve operation that induces shear rate on the cells for disaggregation. At the end of this phase, the signal intensity is at its lowest, confirming the complete disaggregation. Following this phase, phase-1 witnesses an increase in the signal intensity for around 30 s. Like the no coagulation case, this increase is due to the aggregation of the erythrocytes. No more increase beyond the maximum intensity is then observed. This is caused by the formation of fibrin clots preventing further clumping of the erythrocytes and, therefore, ends the aggregation process. The time corresponding to the maximum intensity is named as T_{max}. The signal intensity decreases in phase-2 due to the clot contraction, a process that takes place right after the clot formation [178,179]. Following the end of phase-2, the signal intensity shows a constant trend in phase-3, suggesting that the clot is completely stabilized.

5.3.2 Role of Fibrinogen in Coagulation and Aggregation

When no activator reagent was used in the cartridge, the blood sample does not coagulate but only experiences erythrocyte aggregation. The clumping of the erythrocytes progressively decreases the surface area of the cells, resulting in an ongoing increase in the transmitted signal intensity. When human thromboplastin was used in the cartridge to trigger the coagulation, we observe a similar increasing trend in the optical signal intensity until reaching a peak point.

Referring to the initial 30 s of the red and black signals in Fig. 5.3a, at the start, the signal intensities are the same (at the lowest) due to the prior valve

operation. Then, during phase-1, there is a difference in the intensity increase, therefore in the aggregation rate, between these two cases. When the cartridge is free of any activator, the aggregation rate of the sample (black) is higher than that of the coagulating sample (red). This is mainly due to the fibrinogen activity in the samples.

Fibrinogen, a glycoprotein in plasma, plays an integral part in the coagulation process [159]. It is converted to a fibrous protein named fibrin to form stable clots. Fibrinogen also takes role during EA and is the most essential plasma protein for this process [95,180]. According to the bridging model, fibrinogen proteins adsorb on the cell surfaces bringing adjacent erythrocytes in contact [181].

To show the equally key role of fibrinogen in coagulation and aggregation, fluorescent labeled human fibrinogen was employed. Four WB samples with different fibrinogen concentrations were prepared. Each sample was introduced to a cartridge with human thromboplastin, and the optical measurements were performed. Following the measurements, the cartridges were observed under an upright fluorescence microscope (Zeiss, Germany) at 40x magnification. Figure 5.4a shows the microscopic images for the four samples. The fluorescence regions in each image are the fibrin networks lighting up due to the polymerized dye-labeled fibrinogens. As the fibrinogen concentration in WB increased from 1% up to 4%, the fluorescence illumination area also proportionally increased. It suggests that with the increasing fibrinogen concentration, more fibrinogens took part in the coagulation process, and, therefore, more fibrin strands were formed. Figure 5.4b shows the optical signal intensities of the four blood samples measured with the analyzer. The inset shows the initial 10 s following the complete disaggregation. As the fibrinogen concentration increases, the rate of increase in intensity, namely the rate of aggregation, also increases. It implies that the addition of more fibrinogens facilitates the aggregation of erythrocytes.

When there is no activator in the cartridge, the blood sample does not coagulate, and we observe only the aggregation of the erythrocytes (black signal, Fig. 5.3a). Here, fibrinogens only take role during the aggregation process. On the other hand, the presence of the activator in the cartridge triggers the coagulation

cascade (red signal, Fig. 25.3a). In this case, fibrinogens are simultaneously appealed to take part in the coagulation and the aggregation processes. This splits their energy to two distinct roles that would otherwise play role only in EA. Since fibrinogen concentrations for both cases are the same at the start, the number of fibrinogens taking part in the aggregation process and/or the fibrinogens' aggregation efficiency decrease for the coagulating blood sample in phase-1.

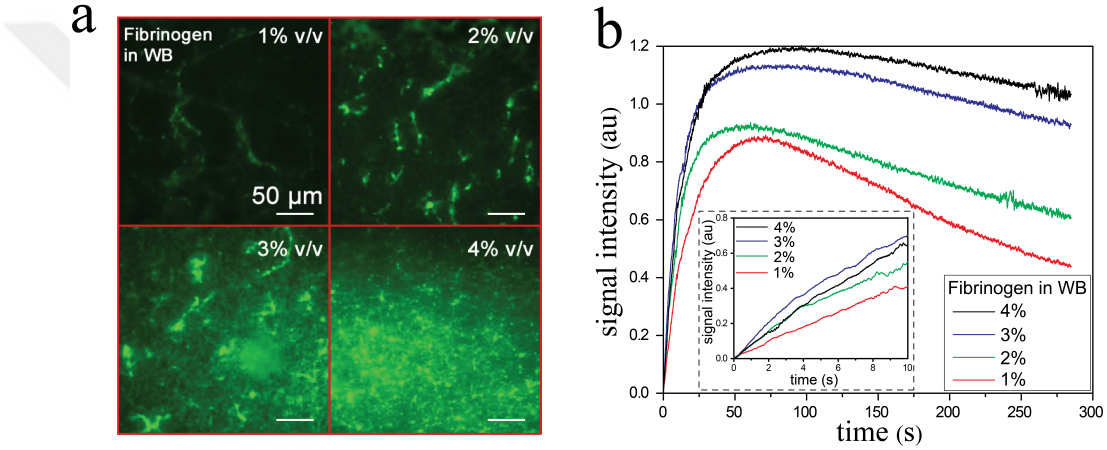


Figure 5.4: The role of fibrinogen in coagulation and aggregation. Four whole blood samples with varying fluorescence labeled fibrinogen concentrations were prepared and introduced to cartridges with human thromboplastin. **a.** The sample-filled cartridges were observed using fluorescence microscopy at 40x. The illuminating regions correspond to fibrin networks formed because of coagulation. **b.** The sample-filled cartridges were tested using the platform. The inset shows the initial 10 s for each case. The rate of aggregation increases with the increasing fibrinogen concentration.

To further confirm these findings, we employed an EA inducer molecule, dextran [68], to enhance the aggregation rate that is affected by the fibrinogens engaged in the coagulation process. Firstly, citrated WB with no dextran was introduced to an empty cartridge, and optical measurement was performed with the analyzer. As shown in Fig. 5.5a (black signal), there is always an increase in intensity due to uninterrupted EA. Secondly, we prepared four WB samples with dextran concentrations of 0 mg/ml, 5 mg/ml, 10 mg/ml, and 15 mg/ml. Citrated

WB with no dextran was introduced to a cartridge having human thromboplastin. In this case (red signal, Figure 5.5a), the intensity increase was observed with a much lower rate compared to the first case. Then, citrated WB samples with different dextran concentrations were introduced to human thromboplastin lyophilized cartridges. Figure 5.5a shows the signal intensities of the measurements for all the cases, and Fig. 5.5b illustrates the first 10 s of each signal for ease of comparison. These results show that the presence of dextran supports the aggregation process and increases the aggregation rate in phase-1. As shown in Fig. 5.5b, higher dextran concentration increases the aggregation rate and, therefore, compensates for the fibrinogen deficiency of the coagulating samples.

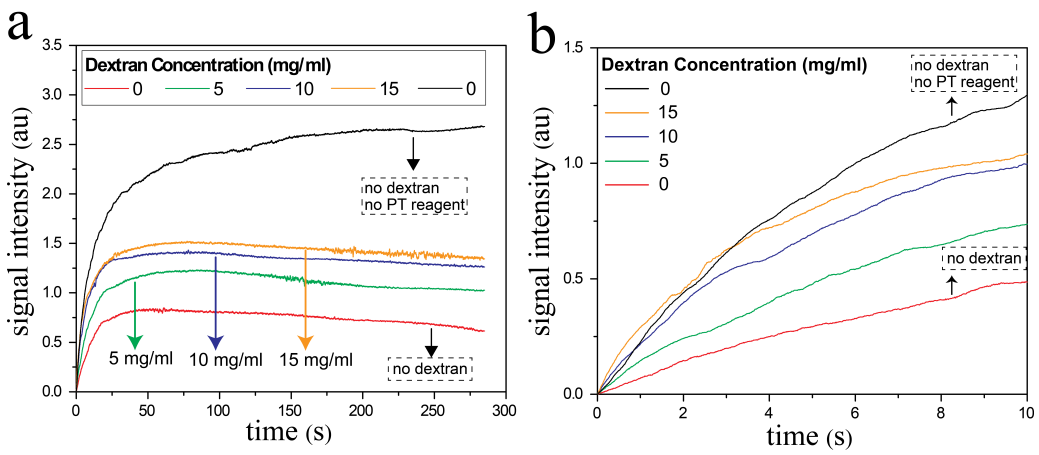


Figure 5.5: The employment of dextran to facilitate the aggregation process in phase-1 for the coagulating blood sample. **a.** Four whole blood samples with varying dextran concentrations were prepared and introduced to human thromboplastin lyophilized cartridges. Also, whole blood sample with no dextran was introduced to an empty cartridge. Optical measurements were performed with the platform. **b.** Initial 10 s of the optical signals given in part **a.**

5.3.3 Comparative Coagulation Time Measurements

For the coagulating blood sample, the transmitted signal intensity initially increases due to EA and reaches a maximum intensity value. The time when the

signal is at the peak is named as T_{max}. The observation that the intensity of the non-coagulating sample increases but that of the coagulating sample does not beyond T_{max} proposes that the EA in the coagulating sample stops at T_{max}. In other words, no further aggregation at and beyond T_{max} stops further intensity increase. We suggest that the reason preventing further aggregation is the fibrin strands that wrap up the erythrocytes and form the clotting at T_{max}. Therefore, T_{max} is the time when the blood coagulation occurs.

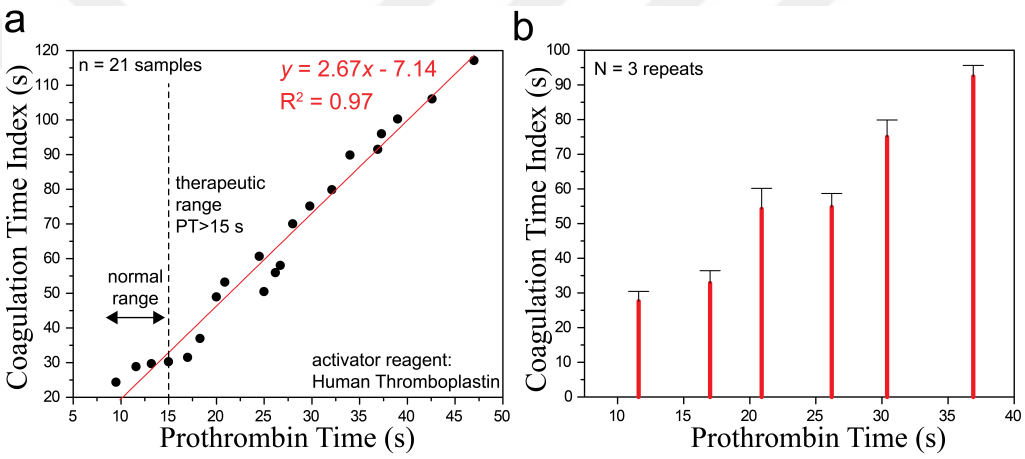


Figure 5.6: Comparison of the platform with the conventional equipment for PT measurement. **a.** Comparison with n=21 whole blood samples. Goodness of the fit is 0.97 using linear regression. **b.** Repeatability analysis with n = 6 samples. Each sample is tested three times. Error bars indicate standard deviations.

To verify that T_{max} is indeed an indication of the coagulation time, specifically prothrombin time (PT), comparative tests were performed at a hospital. First, the PT values of 21 volunteer WB samples were measured using the conventional gold standard method. Afterwards, 50 μl from each WB sample was introduced into a cartridge, and optical measurements were performed using our analyzer. T_{max} values were measured from the transmitted signal intensities using a peak detection algorithm in MATLAB. Figure 5.6a shows the regression analysis for the comparison of the conventionally measured PT values (x-axis) and the T_{max} values measured by our system (y-axis). A linear fit was used to find the linear equation for the T_{max}, and the correlation coefficient (R^2) of the regression fit was

calculated as 97%, demonstrating the high correlation between the measurement platforms. Then, 6 WB samples with PTs in between 10-15, 15-20, 20-25, 25-30, 30-35, 35-40 s ranges were chosen. The samples were tested three times with the analyzer for repeatability analysis, and three T_{max} values for each volunteer sample were averaged. Figure 5.6b shows the mean and standard deviation (SD) of the averaged T_{max} values measured by our system (y-axis). The SD for the sample in the healthy range was around 2.5 s, whereas it was around 4 s for the other samples.

5.3.4 Simultaneous Optical Measurement and Microscopic Observation

We also aimed to observe a blood sample under an optical microscope while measuring the optical transmission signal to demonstrate the actual physical correspondence of the optical signals. Two cartridges were employed for the observation of erythrocytes for coagulating and non-coagulating blood samples as schematically shown in Fig. 5.7a inset. These cartridges were uniquely fabricated to monitor the erythrocytes in real-time under a microscope from the shallow channel segment as well as simultaneously obtaining optical transmission signal from the deep channel segment. Since the erythrocyte population in WB is high, diluted WB (hematocrit: 5%) was used to distinguish individual cells within the sample. We preferred lower concentration human thromboplastin (19 g/l) as an activator reagent for a slower coagulation process to have more detailed cell visualization. 4 μl reagent solution was added into the inlet of one of the cartridges. To ensure the same dilution ratio, 4 μl PBS was added into the inlet of the other cartridge. Following the introduction of the reagent solution or PBS, the blood samples were gently mixed with the reagents for 3 s at the inlets and pipetted into the cartridges for real-time observation under a microscope at 40x magnification during the optical measurements.

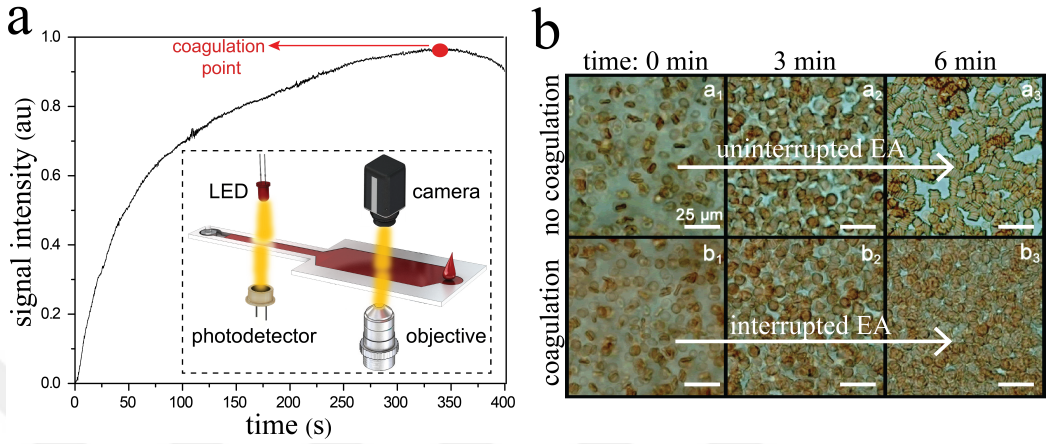


Figure 5.7: **a.** Measurement of the transmitted signal intensity for a coagulating whole blood using the point-of-care platform. The maximum signal intensity is reached in 6 min. The inset is the schematic representation of the simultaneous optical measurement and microscopic observation. **b.** Real-time top-view observation of the non-coagulating (a_1 to a_3) and coagulating (b_1 to b_3) blood samples under an optical microscope. Erythrocytes completely aggregate in the former sample at the end of the 6^{th} min without any interruption. Erythrocytes partially aggregate in the latter sample, followed by the prevention of the aggregation due to the coagulation of the sample.

The "no coagulation" case in Fig. 5.7b represents the non-coagulating blood sample, whereas the "coagulation" case in Fig. 5.7b represents the coagulating blood sample. At time: 0 min, the cells were all disaggregated in both cases. At the "no coagulation" case, the erythrocytes started to partially aggregate as time passed, and they completely aggregated at time: 6 min due to no internal (e.g., coagulation) or external (e.g., shear rate) intervention on them. At the "coagulation" case, the erythrocytes started to aggregate with a lower rate, compared to the "no coagulation" case, due to the onset of the coagulation. The aggregation process was clearly observed from the 0^{th} min (b_1) to the 3^{rd} min (b_2). Then, aggregation hardly progressed, and, finally, the cells were all packed at the 6^{th} min (b_3). This demonstrates that the coagulating blood sample coagulated at the 6^{th} min. This was also verified in Fig. 5.7a showing the transmitted signal intensity for the coagulating blood sample that reaches its maximum in around

350 s (T_{max} = 350 s).

5.4 Conclusion

In this chapter, we reported optical investigation of EA during coagulation for demonstrating the interrelation between aggregation and coagulation processes as well as measuring blood coagulation time using a novel methodology employing EA mechanism. The platform optically investigates the aggregation of the erythrocytes and extracts the time for the formation of fibrin networks hence the time of coagulation. The assay was shown to be responsive to the evaluation of the extrinsic pathway of the coagulation cascade (prothrombin time). It requires only 50 μl blood and is completed in less than 5 min. The test results demonstrated the high correlation of the platform with a conventional benchtop equipment. The role of fibrinogen proteins in the aggregation and coagulation processes and therefore on the measured optical signals was shown through fluorescence imaging of labeled fibrin strands as well as using dextran as an aggregation inducer in the blood samples.

Chapter 6

Low-cost approach to prothrombin time measurement

Coagulation is an essential physiological activity initiated by the interaction of blood components for clot formation. Prothrombin time (PT) measurement is a clinical test for the assessment of the extrinsic/common pathways of coagulation cascade. Periodic measurement of PT is required under numerous conditions including cardiovascular disorders. In this chapter, we present a self-powered microfluidic device for quantitative PT measurement from 50 μl whole blood. The entire platform is disposable and does not require any external pumping, power, or readout units. It consists of a 3D-printed effervescent pump for CO_2 generation from a chemical reaction, a cartridge for two-channel fluid flow (blood and water), and a grid for the quantification of fluid migration distance. Following the introduction of the fluids to the corresponding channel inlets, marking the coagulation start, an acid-base reaction is triggered for gas generation that drives the fluids within the channels. When the blood coagulates, its flow in the channel is halted. At that point, the distance water has travelled is measured using the grid. This distance correlates with PT as demonstrated through clinical tests with patient samples.

The content of this chapter was published in [172] as;

M. T. Guler, Z. Isiksacan, M. Serhatlioglu, and C. Elbuken, Self-powered disposable prothrombin time measurement device with an integrated efervescent pump, Sensors and Actuators B: Chemical, vol. 273, pp. 350-357, 2018.

6.1 Introduction

Blood coagulation is a dynamic hematological activity necessitating the interplay of numerous plasma proteins, cells, and coagulation factors for the formation of cross-linked fibrin networks to prevent bleeding [158]. The coagulation cascade is triggered by either extrinsic or intrinsic pathways through the activation of tissue factors or surface, respectively, and leads to a common pathway where stable fibrin strands are formed from fibrinogen [159, 182]. Prothrombin time (PT) test is frequently performed in clinics for the evaluation of the extrinsic and common pathways of the coagulation cascade [183]. Sensitive and periodic measurement of this parameter is critical for patients who are under pre-, peri-, and post- operative monitoring or undertaking anticoagulant therapy for the regulation of the clotting status by the blood-thinning drugs such as a vitamin K antagonist Coumadin [160, 161]. People with coagulation disorders, atrial fibrillation, pulmonary embolism, myocardial infarction, and several other cardiovascular diseases as well as heart valve prosthesis need lifelong anticoagulant therapy [184, 185]. However, the medications for the therapy have narrow therapeutic windows [186]. Therefore, the required dose varies among individuals and fluctuates for the same patient on a daily basis because of diet and genetic background [164, 187]. The failure to receive maintenance doses may result in either hemorrhage or thrombo-embolism, which are both life-threatening [187, 188]. The conventional practice to monitor the course of the therapy is hospital visits at fixed intervals for PT measurements by benchtop devices. This practice, on the other hand, is time-consuming and expensive, and delayed visits may end up with unfortunate consequences.

Point-of-care devices have been developed to address the issues associated with the benchtop counterparts in clinical settings [189]. Commercial coagulation

time measurement devices have been launched to decrease the test turnaround times [165]. Different measurement principles are being utilized including electrochemical detection (CoaguChek XS), mechanical measurement by a cantilever (CoagMax), or optical detection of the cease of blood flow (Hemochron Signature) [166, 190]. These products consist of a main device and disposable test cartridges that contain the necessary reagents, electrodes, magnetic particles, or MEMS structures depending on the measurement principle. Even though these products have a potential for point-of-care testing to facilitate timely intervention in case of emergency, the costs of the main devices make them unaffordable for the majority. Since the health insurances in most of the countries have limited coverage for such devices, the patients are dependent on clinics or anticoagulation centers for their periodic PT measurements. The tests are even more inaccessible for those living in resource-poor regions. The microfluidics community is aiming to develop novel methodologies for the PT measurements such as impedimetric [191], aptamer-based [192], paper-based [167], cantilever-based [193], quartz crystal microbalance (QCM) [170], centrifugal [194] and fluorescence-based [195]. These studies, on the other hand, generally have a long way to compactness and lack clinical validation tests, which are necessary for commercialization.

The requirement to employ external components such as pumps, power sources, and control circuitry increases the cost and complexity of lab-on-a-chip platforms while limiting their portability [196]. Miniaturized integration of these components is desired to make these platforms appropriate for point-of-care use. Apart from the frequently used pressure or syringe pumps, the liquid handling is aimed through micropumps categorized as non-mechanical (electrowetting, electrokinetic, electrochemical) and mechanical (rotary, peristaltic, diaphragm) [12, 14]. Of the first category, chemical pumps have recently become popular for the construction of self-powered platforms due to their simple fabrication and integration [197]. Examples include the decomposition of H_2O_2 or N_2H_4 in the presence of metal substrates (e.g., Ag, Au, Pt, Pd) for self- electrophoresis [198] or electroosmosis [199], respectively. Methanol is decomposed in a microfluidic device to generate CO_2 for fluid pumping [200]. Differing from this trend, chemical

pumps can also be designed without any need for microfabricated substrates. Effervescent tablets used in medical treatment are composed of an acid and a base. Before intake, these tablets are dissolved in water generating CO_2 bubbles. As shown in this work, effervescent micropumps can employ acid-base neutralization reactions in aqueous solutions that generate enough CO_2 for long durations to drive fluids in microfluidic systems for a variety of applications. These effervescent micropumps yield predictable pressures, with rapid response times and long durations at steady-state values, that are firmly controlled by the type and the molarity of the reactants used in the reactions [201].

In this chapter, we present a portable and entirely disposable microfluidic device for point-of-care PT measurement from 50 μl whole blood in less than 2 min. The device is lightweight (50 g) and does not require any external components. Even though the device is designed for self-evaluation of the test result, integration of a cell phone makes it an ideal telemedicine application if needed. The key element of this self-powered system is an integrated effervescent pump where an acid-base neutralization reaction generates CO_2 gas that supplies pressure for liquid flow within the two-channel test cartridge. The sample channel is for whole blood, whereas the reference channel is for DI water. The assay principle is based on the measurement of the distance travelled by water using an integrated grid upon the cease of the blood flow due to coagulation. We explained the fabrication steps of the 3D-printed effervescent pump and characterization results of the generated pressure and settling time of the pump for different acid and base molarities. Comparative tests were performed at a local clinic using a conventional benchtop device to show the potential of our system for reliable and quantitative PT measurements.

6.2 Experimental

6.2.1 Sample Preparation

We acquired 3 ml intravenous whole blood from each volunteer into vacuum tubes containing 3.2% sodium citrate anticoagulant at most 6 h before the tests. The samples were incubated at 37 °C before use. 47.5 mg Thromborel S Human Thromboplastin was dissolved in 250 μl DI water at room temperature. 10 μl of the solution was pipetted into the inlet of the sample channel of each cartridge, and the cartridges were left at -80 °C for 2 h. The reagents in the cartridges were then lyophilized in a freeze-dryer (Labconco, US) for 6 h, and the cartridges were stored at 4 °C until their use.

Coverslips (20 mm x 20 mm, thickness: 0.15 mm) were purchased from neuVitro. Silicone (ID: 1/32 in) and tygon (ID: 3/32 in) tubings were purchased from Cole Parmer. Dual bulb exact volume pipettes (50 μl) were purchased from Alpha Laboratories Ltd. Liquid sodium citrate as an anticoagulant was passed through the exact volume pipettes, and the pipettes were left to dry at room temperature overnight.

6.2.2 Cartridge Fabrication

The test cartridge design was drawn in a CAD software (AutoCAD 2016). Transparent 3mm thick PMMA sheet was obtained from a local supplier, and the cartridges were fabricated out of PMMA using a 30W CO_2 laser cutter (Epilog, Zing). The feed rate, power, and frequency of the cutter were set to 2.6 cm/s, 2.4 W, and 1000 Hz, respectively. The cartridge has a 34 mm x 127 mm rectangular structure. It has two inlets for two separate serpentine channels. One channel is for the reference fluid (DI water), and the other channel is for the sample fluid (whole blood). The inlet chamber volumes are 85 mm^3, and the outlet chamber volume is 16 mm^3. The serpentine channels have 80 μm height and 250 μm width.

The Hagen-Poiseuille law for a steady, laminar, and Newtonian flow states that

$$\Delta P = QR \tag{6.1}$$

where ΔP is the pressure difference, Q is the volumetric flow rate, and R is the channel resistance. For rectangular channels, the hydrodynamic resistance for $0<h/w<1$ is approximated as

$$R = \frac{12\eta L}{wh^3}[1 - 0.63\frac{h}{w}]^{-1} \tag{6.2}$$

where η is the dynamic viscosity, L is the channel length, w is the channel width, and h is the channel height. Also,

$$Q = \frac{wh\Delta L}{\Delta t} \tag{6.3}$$

where t is the time. Plugging equations (6.2) and (6.3) into (6.1), we have

$$L = \sqrt{\frac{th^2\Delta P}{12\eta}[1 - 0.63\frac{h}{w}]} \tag{6.4}$$

DI water dynamic viscosity is lower than whole blood apparent viscosity, so the water flows faster in a channel in a given time interval. Therefore, the length of the serpentine channels is found by taking the water flow into consideration. The clotting time for a whole blood sample is around 110 s at max. The channel length should be sufficiently long so that water does not reach the outlet until the coagulation, i.e., $t = 110$ s. ΔP generated by the effervescent pump is 195 mbar as explained in the next section. Also, $h = 80$ μm and $\eta = 8.9\text{x}10^{-4}$ Pa.s. Plugging these parameters in equation (6.4), the length of the serpentine channel is calculated as 1100 mm.

6.2.3 Effervescent Pump Fabrication

The effervescent pump consists of four polymer layers and a coverslip as shown in Fig. 6.1. The four layers were designed in a CAD software (SolidWorks 2016) and fabricated by a 3D-printer (M200, Zortrax) with 100% infill. The filament was acrylonitrile butadiene styrene (ABS), a thermoplastic polymer used as a common

3D printing material [202]. The 1^{st} printed layer contains a space for aqueous solution filling and two posts for the alignment of the other layers. Following the filling of the aqueous solution (1 ml DI water and dissolved base), the 2^{nd} printed layer is aligned on top of the 1^{st} printed layer. Afterwards, a glass coverslip with 150 μm thickness is fit in the 2^{nd} printed layer. Then, the 3^{rd} printed layer is aligned on top of the 2nd printed layer. This layer contains a window in contact with the coverslip where we add the acid powder. The 4^{th} printed layer contains a hole at the center for the insertion of a metal pin and two identical holes for the insertion of tubings. The other ends of these tubings are later inserted to the inlets of the cartridge. A metal pin is covered with a gasket made of soft silicone tubing to prevent gas leakage, and the pin is inserted to the center hole of the 4^{th} layer. Following the insertion, a U-shape PMMA bowl was sealed to the pin bottom. This bowl aims to cover the powder on the coverslip such that any orientation change of the pump does not spread the powder. It also ensures that all the powder falls into the aqueous solution after the coverslip breaking. Following the sealing of the bowl to the pin, we placed the 4^{th} layer on top of the 3^{rd} layer. After the alignment of all, the layers are sealed to one another with epoxy adhesive (Pattex, Henkel) to prevent potential leakage. The pump was then tested up to 250 mbar, and no gas leakage was observed.

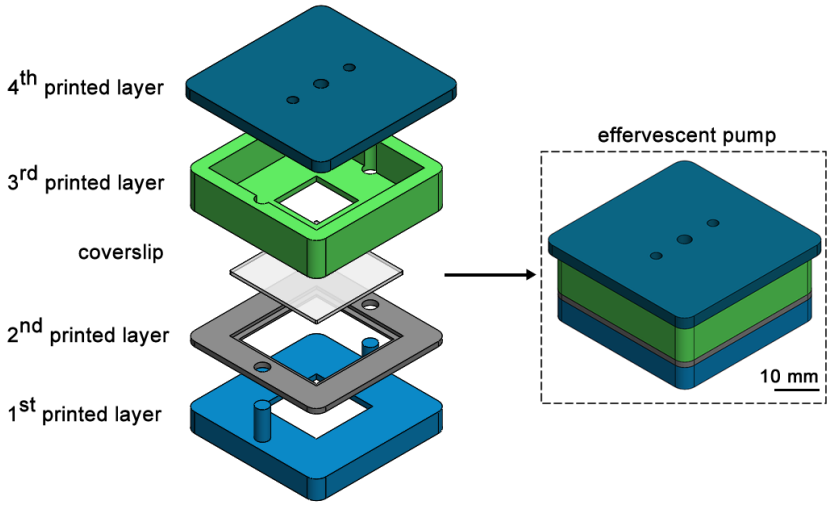


Figure 6.1: Schematic drawing of the effervescent pump layers and their assembly. The pump has four 3D-printed layers and a glass coverslip. The 1^{st} and 3^{rd} layers contain the aqueous solution and acid powder, respectively.

6.2.4 Measurement Platform

Referring to equation (6.4), the time at which fluid travels a certain distance in a microfluidic channel can be measured once the fluid viscosity, channel dimensions, and applied pressure are known. Using this principle, we aimed at measuring the prothrombin time of a whole blood sample travelling in a microfluidic channel. However, blood is a non-Newtonian fluid, and blood viscosity varies for everyone, depending on various hematological and external parameters such as hematocrit, plasma proteins' concentration, erythrocyte aggregation, and temperature. Two different whole blood samples might have the same PT value, but this does not necessarily mean that these samples have the same viscosity. In other words, the quantification of the travel distance of a blood sample is not a correct method for the measurement of PT. Therefore, a reference Newtonian fluid, whose viscosity is constant, is employed along with the whole blood sample for PT measurement. This eliminates the effect of blood viscosity variation on test results.

Figure 6.2a and 6.2b show the schematic representation and photography of the device excluding the readout grid. The fabricated pump is tightly placed on the cartridge. There are two gas transfer tubings. Each is a silicone tubing (8 mm), one end of which is inserted to the pump. The other end is inserted to a larger diameter tygon tubing (2 mm) that is inserted to the center hole of a 1 cm x 1 cm PMMA structure. The opposite side of the PMMA structure has a double-sided tape ready for sealing the cartridge inlets. The cartridge has a sample channel (SC) for whole blood and a reference channel (RC) for coloured DI water. The channels share a common outlet. The activator reagent is lyophilized in the inlet of the SC a few hours before the test ($<$ 6 h). 50 μl DI water is pipetted into the inlet chamber of the RC. Fluidic connections are established between the pump and the channels using tygon tubings.

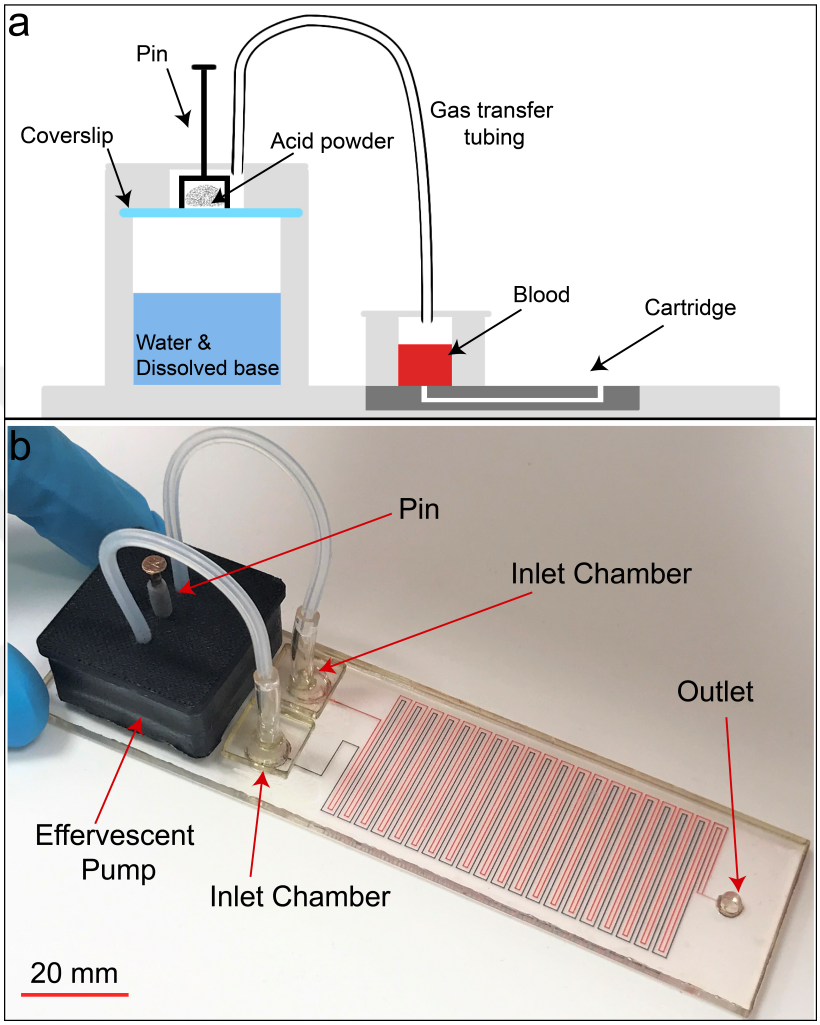


Figure 6.2: **a.** Schematic representation and **b.** photograph of the PT measurement device. The device consists of an effervescent pump for CO_2 generation and a two-channel transparent cartridge. Gas pressure drives the sample and reference fluids in their serpentine channels. The coagulation stops the sample fluid flow, and the reference fluid flow is manually stopped at that moment. The distance traveled by the reference fluid is correlated with the sample fluid PT. The fluids used in **b** are DI water colored with red and black food dyes for demonstration.

The following steps are then performed for the measurement: Step 1. 50 μl anticoagulated whole blood sample is pipetted into the inlet chamber of the SC. The sample is mixed for 5 s with the lyophilized reagent using the pipette to

trigger the coagulation process. Then, the PMMA structure is placed on the chamber for the tubing connection between the pump and SC (Fig. 6.3a). The capillary force or the pressure generated by the placement of the PMMA structure over the inlet does not drive the sample in the serpentine microchannel at this stage due to the channel hydrophobicity. Step 2. The pump pin is gently pushed down with a finger to break the coverslip (analogous to pressing a START button). The acid powder falls into the aqueous solution, and an acid-base reaction takes place within seconds (Fig. 6.3b). Step 3. The generated CO_2 inside the pump and the gas transfer tubings apply equal pressure on the fluids in the inlets (Fig. 6.3b). Step 4. This constant pressure drives both the sample and reference fluids in their corresponding channels (Fig. 6.3b). Step 5. After some time, the sample fluid stops flowing in the SC due to the coagulation, which forms stable fibrin strands trapping the blood cells and adhering to the SC surfaces (Fig. 6.3c).

The aim is to measure the distance travelled by the reference fluid using the custom-developed grid when the sample fluid stops flowing (step-5). For this purpose, one of two alternative steps can be performed depending on the user's choice/need. Step 6. (first alternative) At the instant when the sample fluid stops, the tubing ensuring the connection between the pump and the RC chamber inlet is manually pulled from the corresponding pump hole to prevent further gas transfer. This stops the flow of the reference fluid in the RC. For the clinical tests at the local hospital, we preferred this method and did not experience any difficulty. However, this step might be prone to minor user-mediated error if the user is not attentive enough to stop the reference fluid flow at the right time. Step 6. (second alternative) Following step-2, a video of the device with the grid underneath is recorded using a cell phone for 3 min. For ease of operation, a custom-made cell phone stand was fabricated out of PMMA using the laser cutter. Then, the video can be replayed to find the frame where the sample fluid stops flowing. Step 7. The distance travelled by the reference fluid is measured using the grid by naked eye from either the device itself (1^{st} alternative) or from the recorded video (2^{nd} alternative). This distance is a measure of the PT of the sample fluid.

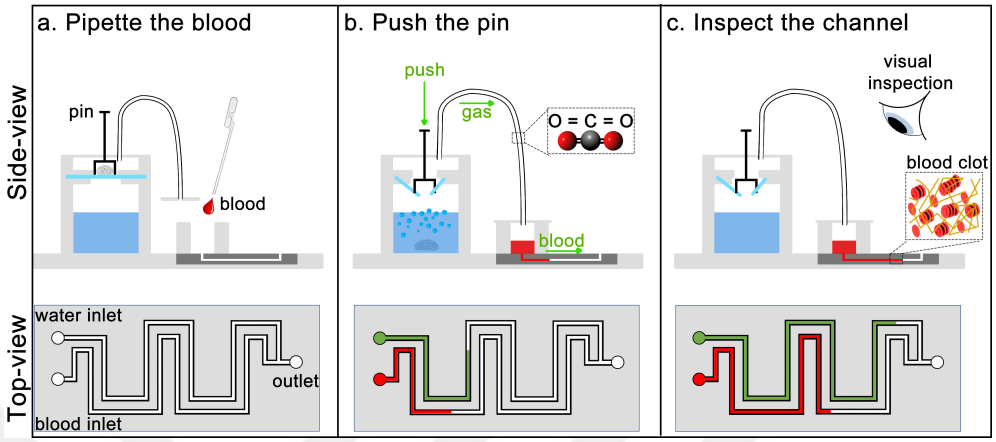


Figure 6.3: Schematic representation of the device and the channels during test. **a.** The blood sample is pipetted into the SC inlet and mixed with the reagent. **b.** The pin is pushed, starting the reaction and forming the gas. The generated pressure drives both fluids. **c.** The blood coagulates, and the fluid flow in the channels is observed by eye.

Referring to step-1, 5-s manual mixing of the blood with the reagent seems a drawback in terms of a potential for user-mediated error. A magnet or a pinch valve could have been used for the same purpose. However, we have not integrated such a mechanism to keep the cost lower. To characterize the time error during the mixing, a co-author performed the same 5-s pipette mixing 50 times. At the same time, another co-author employed a timer to measure the time as a reference. The mean and standard deviation of the repetitive tests are 5.28 s and 0.44 s, respectively. Similarly, we asked 50 different volunteers (age range: 15-65) to perform a pipette mixing. The mean and standard deviation of these tests are 5.26 s and 0.74 s, respectively. In each case, the error is less than 1 s.

6.3 Results and Discussion

6.3.1 Effervescent Pump Characterization

The neutralization reaction between citric acid ($H_3C_6H_5O_7$) and sodium bicarbonate ($NaHCO_3$) in an aqueous solution yields carbon dioxide (CO_2) and salt.

$$H_3C_6H_5O_7(aq) + 3\ NaHCO_3(aq) \rightarrow 3\ CO_2(g) + 3\ H_2O(l) + Na_3C_6H_5O_7(aq)$$

We employed the gaseous product of this acid-base reaction as the pumping source to drive the fluids in the channels. To find the optimum concentration of the reactants for which the gas pressure reaches the equilibrium value as fast as possible (i.e., low settling time) and keeps its value during the PT measurement (max 100 s), the pump was characterized with different amounts of the acid and base. The two schemes taken into consideration were (1) dissolving the base powder in DI water and then adding the acid powder and (2) dissolving the acid powder in DI water and then adding the base powder. We have also considered adding the acid and base powders to the water at the same time, but that dramatically increased the settling time.

During the pump construction, we added base dissolved aqueous solution to the 1^{th} layer and the acid powder to the 3^{rd} layer for scheme-1, or acid dissolved aqueous solution to the 1st layer and the base powder to the 3^{rd} layer for scheme-2. After the pump construction, we inserted a metal pin to the center hole and a silicone tubing to one of the side holes of the 4^{th} layer. The other hole was sealed with silicone glue to prevent leakage. The other end of the tubing was connected to a pressure sensor (40PC015G, Honeywell), which was sampled using a data acquisition card (DAQPad-6015, National Instruments, US). Figure 6.4a plots the generated pressure for four different concentrations of the dissolved base when the same acid powder amount ($0.99\text{x}10^{-4}$ mole) was used.

Let $0.99\text{x}10^{-4}$ be $n/3$. Referring to the chemical equation, the ratio of the stoichiometric coefficient of the acid to the base is 1/3. Therefore, at equilibrium,

$n/3$ mole of the acid reacts with n mole of base (red signal, Fig. 6.4a). In this case, the pressure increases at a slow rate, and the equilibrium pressure cannot be reached within 700 s. Then, $2n$, $4n$, and $8n$ moles of the base were dissolved for different pumps. In these cases, the acid is the limiting reactant, so regardless of the increase of the base mole, the generated gas amount is always n mole. On the other hand, increasing the base amount from n mole up to $8n$ mole enhances the interaction between the acid and base molecules, resulting in a significant decrease in the settling time. When $8n$ mole of the base is dissolved (black signal, Fig. 6.4a), the settling time is 5 s; the equilibrium pressure is 195 mbar and it stays constant for 700 s. For the other base amounts, the settling time differs, but if we wait long enough, the pressure value reaches to the equilibrium (195 mbar) since the generated gas amount is the same.

Similarly, Fig. 6.4b plots the generated pressure values for four different concentrations of the dissolved acid when the same base powder amount (2.97 x 10^{-4} mole) was used. Let 2.97 x 10^{-4} be n. At equilibrium, n mole of the base reacts with $n/3$ mole of the acid (red signal, Fig. 6.4b). We observe that this amount is not enough to reach the equilibrium pressure within 700 s. Therefore, the acid amount was increased to $2n/3$, then $4n/3$, and finally to $8n/3$. In these cases, the base is the limiting reactant, so the generated gas amount is always n mole. As also witnessed in Fig. 6.4a while increasing the base amount, increasing the acid amount here facilitates the molecular interaction and therefore decreases the settling time. On the other hand, in this scheme, none of the reactions could reach the equilibrium gas pressure within 700 s; only the reaction for $8n/3$ mole of the acid approaches it very closely.

The pressure generated by the chemical reaction reaches to the equilibrium value faster in scheme-1 compared to scheme-2. The pre-dissolved reactant (base in scheme-1 and acid in scheme-2) is always ready for the reaction, so it is the reactivity of the reactant added later to the aqueous solution that causes this difference. In scheme-1, the added reactant is citric acid whose ionization/dissociation constant is higher than that of the sodium bicarbonate (like the case for many other acids compared to bases). The reaction starts faster, and therefore the equilibrium pressure is reached faster. Based on these observations, scheme-1

was chosen for the pump of the device. $8n$ mole of sodium bicarbonate was dissolved in DI water, and n mole of citric acid was placed onto the coverslip whose breakage with the metal pin would start the reaction.

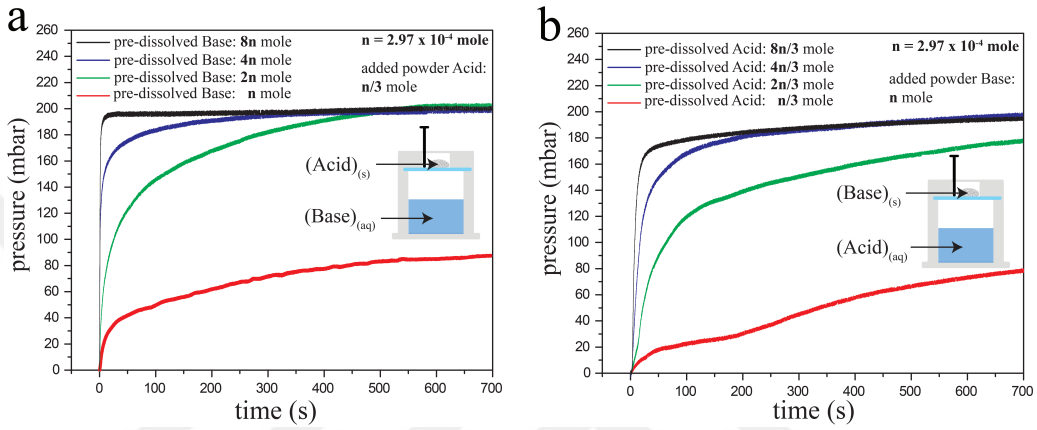


Figure 6.4: Characterization of the effervescent pump for different acid and base amounts. The pressure values of CO_2 generated by the reactions were measured. **a.** Scheme-1: different moles of sodium bicarbonate were dissolved in DI water, and the same mole of citric acid was added to the aqueous solution. **b.** Scheme-2: different moles of citric acid were dissolved in DI water, and the same mole of sodium bicarbonate was added to the aqueous solution. Scheme-1 allows smaller settling time and longer stay in the equilibrium pressure in 700 s.

6.3.2 Quantitative Distance Measurement

The measurement principle of the device is based on the assessment of the distance travelled by the reference liquid in its corresponding channel (RC) at the end of the coagulation process. Since there is no electronic readout unit for the device, which indeed makes it low-cost and disposable, accurate quantitative distance measurement with the naked eye is essential. Therefore, we designed a grid specific for the test cartridge. Figure 6.5a is the schematic drawing of the cartridge demonstrating only the RC. Point A is where the flow starts from the inlet. Figure 6.5b is the designed grid where the dashed lines correspond to the borders of the cartridge. Point B in Fig. 6.5a matches with the bottom red point in Fig. 6.5b.

The grid consists of 18 horizontal (k) and 39 vertical (n) lines. The distance between two horizontal lines is 1.5 mm. The vertical lines are divided into two sets: odd (written bottom) and even (written top). The distance between two odd vertical lines and between two even vertical lines is 2.25 mm.

The grid was drawn in a CAD software (Autodesk, AutoCAD 2016) and printed on a white paper. Then, the printed paper was taped on a PMMA layer (thickness: 3 mm, width: 8 mm, length: 15 mm). The cartridge is placed on the paper grid such that the cartridge stays inside the representative cartridge borders of the paper grid (dashed lines in Fig. 6.5b). The liquid flow starts with the start of the chemical reaction and ends with the blood coagulation. Following the coagulation, it is read with naked eye to determine the vertical (n) and horizontal line (k) at which the reference liquid has stopped.

If n is odd, the travelled distance is calculated using the following equation,

$$L_{nk} = 0.75[10 + 36n + 2k] \ \ mm \tag{6.5}$$

If n is even, the travelled distance is calculated using the following equation,

$$L_{nk} = 0.75[45 + 36n - 2k] \ \ mm \tag{6.6}$$

where $1 \leq n \leq 39$ and $1 \leq k \leq 18$. It is also possible that the liquid may stop between two n or two k values. In this case, the user can decide which value to choose. The error will be less than 1.5 mm, which corresponds to 0.1 s error in PT.

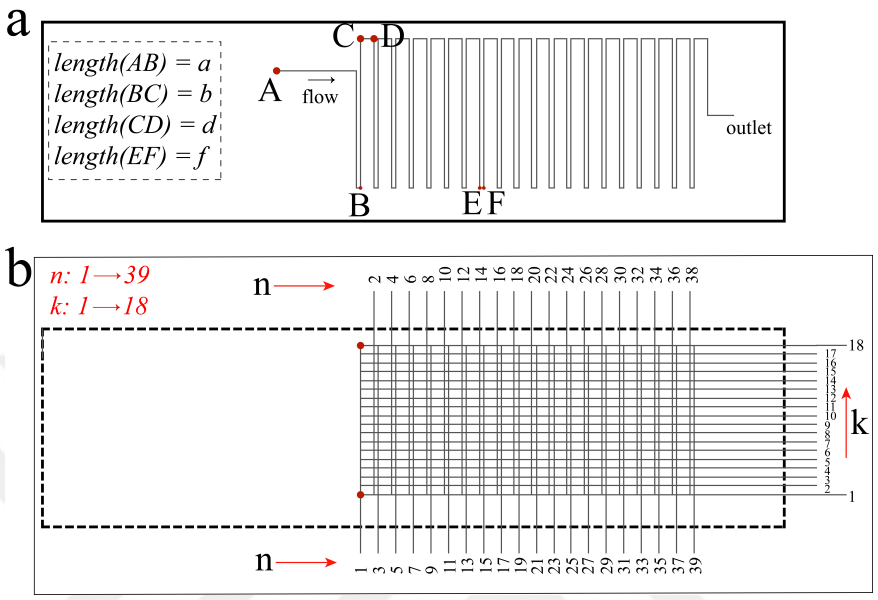


Figure 6.5: Grid design for quantitative distance measurement. **a.** Schematic drawing of the test cartridge demonstrating only the reference channel. **b.** The grid for the measurement. The dashed lines correspond to the cartridge borders. The grid has 18 horizontal lines k and 39 vertical lines n.

6.3.3 Comparative Prothrombin Time Tests

We performed tests at a clinic to demonstrate the correlation between the reference fluid travel distance measured from the device and the conventionally measured PT time. Human thromboplastin was lyophilized in the sample inlets of the cartridges. The donor whole blood samples were acquired via venipuncture into blood tubes. The tubes were centrifuged to get the plasma portion which was then placed into the benchtop PT analyzer (Sysmex, Siemens). Following the conventional PT measurement, 7 whole blood samples whose PT values were between 10 s and 45 s were picked from the sample population (healthy range is: 10-17 s). Afterwards, we introduced 50 μl from a whole blood sample into the sample inlet of a cartridge for a single test. Each blood sample was tested three times. The distances travelled by the sample and the coloured DI water were measured using the equations (6.5) and (6.6).

Figure 6.6 demonstrates the regression analysis for the correlation between the conventionally measured PT versus the distance travelled by the sample fluid (Fig. 6.6a) and the distance travelled by the reference fluid (Fig. 6.6b). No correlation can be seen between the conventional PT and the distance travelled by the sample fluid. Referring to equation (6.4), the viscosity values of the sample fluids are also in play, determining the flow characteristics of the fluids along with their coagulation times. This finding has also rationalized the use of the reference fluid having the same viscosity across the tests. On the other hand, the correlation coefficient between the conventional PT values and the distance travelled by the reference fluid is 99% using the following exponential decay function $y = a - be^{-cx}$ where $a = 793$, $b = 704$, and $c = 0.05$. This trend shows that as the PT value increases, the distance travelled by the water also increases but at a decreasing rate each time. Referring to equation (6.2), the reason for the decreasing rate is the increase in the resistance, R, of the channel as the fluid proceeds within the channel (as L increases). The increase in the resistance makes it difficult for the fluid to flow, delaying its progress.

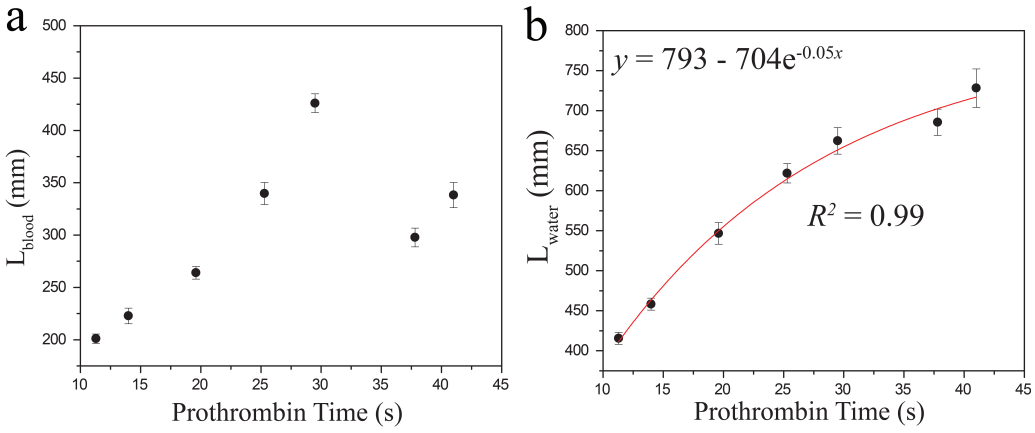


Figure 6.6: Comparing the device with the conventional benchtop PT analyzer for PT measurement. 7 whole blood samples were tested three times. Error bars indicate 2 standard deviations. **a.** Conventional PT measurement versus blood travel distance does not have any correlation due to the differences in blood viscosities. **b.** Conventional PT measurement versus water travel distance correlates 99%.

According to Fig. 6.6b, the equation relating the PT (T) to the travelled distance (L_{nk}) is the following:

$$T = 20ln[\frac{704}{793–L_{nk}}]\ mm \tag{6.7}$$

To free the user from any mathematical calculations, we have prepared a table tabulating the prothrombin time values (T) for any n and k.

6.3.4 Personal Prothrombin Time Measurement

The aim of this entirely disposable device is to allow facile PT measurement from fingerprick blood for home use by the patients. We therefore carried out a case study to demonstrate the potential of the device toward this goal. (I) The pump having the chemicals, pin, and tubings, (II) the cartridge having the green coloured DI water in the reference inlet and lyophilized reagent in the sample inlet, and (III) the paper grid are all integrated together to make the device a single-unit. A test kit was prepared that has a blood lancet, an exact volume pipette (the pipette interior is anticoagulated), and the device. The kit was handed to a 65-year old female volunteer who has been undertaking anticoagulant therapy and using Coumadin for 10 years. Verbal instructions were given to her who performed the steps herself. The left middle finger was punched using the blood lancet. 50 μl whole blood was taken into the exact volume pipette and then introduced the sample inlet. Following 5 s gentle mixing of the sample with the pipette, the inlet was sealed with the square PMMA structure to establish the tubing connection. The pin of the pump was gently pushed to start the reaction. The whole blood flow was observed, and when it stopped, the pump side of the tubing, which transfers gas to the water inlet, was manually disconnected from the pump. This immediately stopped the water flow. Then, the intersection of the vertical and horizontal lines of the grid was read with the eye without any difficulty. The vertical line was the 16^{th} (n = 16) and the horizontal line was the 3^{rd} (k = 3) as shown in Fig. 6.7. Since n is even, equation (6.6) gives the distance travelled by the water, which is L_{nk} = 461.25 mm. The prepared table was used to find the prothrombin time for these n and k values as 15.05 s.

The volunteer is asked to repeat the test 5 times in total over the course of one hour. The mean and the standard deviation of the measured PT are 14.45 s and 0.44 s, respectively. The fingerprick whole blood of the same volunteer was also tested with Hemochron Signature Elite (Accriva) as a reference, and the PT was measured as 14 s, which agrees well with the result of the presented device.

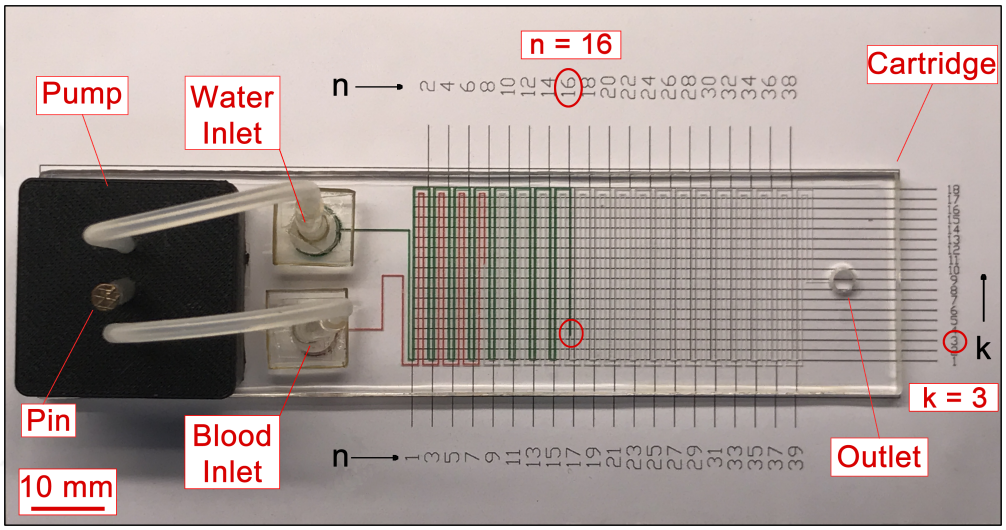


Figure 6.7: The photograph of the device after the PT measurement test for the case study. The device is an integrated single-unit and consists of a pump, a cartridge, and a grid. With the coagulation of the blood sample, the green colored DI water stops at (n, k) = (16, 3), which can be read with naked eye.

The physicians can sometimes be suspicious about the potential of the home-use of the point-of-care devices for two primary reasons. (I) The patient might get an erroneous diagnostic result or no result at all due to wrong use of the device. (II) The patient might get the correct diagnostic result but take a wrong action based on the result such as changing the dose of a medicine. The developed device can still comfortably be used as a telemedicine platform even if these concerns are present. The test results or the video of the tested cartridge can be shared with a professional for the evaluation of the test result. This eliminates both the wrong use of the device as well as discouraging the user to take actions before informing the physician.

Viscosity of coagulating or non-coagulating whole blood is another clinically relevant parameter, which is often overlooked. The determination of average blood viscosity during coagulation is important to understand the interrelation between coagulation dynamics and hemorheological properties [203, 204]. The viscosity of blood is affected by shear rate due to two distinct internal mechanisms that yields its non-Newtonian characteristics: erythrocyte aggregation and erythrocyte deformation. Thus, it is critical to perform the coagulation time measurements at physiologically relevant flow conditions. The presented double channel structure with a reference flow channel is a potential platform for such a measurement. Since the reference flow viscosity is known, the coagulating sample viscosity can be measured, which has clinical value rather than home-use. Then, as a future direction, the disposable platform can be used for obtaining the two parameters, PT and viscosity, simultaneously from the same blood sample.

6.4 Conclusion

In this chapter, we presented a portable and entirely disposable device enabling point-of-care prothrombin time measurement from 50 μl whole blood in less than 2 min. This device consists of the full integration of an effervescent pump, a two-channel test cartridge, and a grid for readout. The use of the effervescent pump, carrying out a neutralization reaction to generate CO_2 for fluid handling, eliminates the need of external components for pumping and energy source. Also, the custom-made paper grid allows easy readout with naked eye, freeing the system from a costly readout unit. The underlying principle is based on the measurement of the distance travelled by the reference fluid in a serpentine channel, right after the coagulation process of the sample fluid in the other serpentine channel of the cartridge. The test results performed at a local hospital demonstrated the high correlation between the conventionally measured PT and the reference fluid travel distance. The case study revealed the ease-of-use of the device by non-professionals for home use and showed the potential of the device for coagulation screening at the point-of-care. This portable, low-cost, lightweight, disposable, easy-to-use and rapid device is promising for periodic PT measurement from low

volume whole blood for both lab- and home-based monitoring.

Chapter 7

Conclusion and Future Directions

7.1 Concluding Remarks

We have grown up with the idea that a healthy breath is the most precious asset on earth. It is indeed not without a solid reason. During the years I have carried out my Ph.D. studies (2014-2019), around 17 million people worldwide died each year because of cardiovascular diseases, making them responsible for more than 25% of all deaths. This rate is the double of cancer-related deaths.

This thesis divided blood flow characteristics into three main streams: hemorheology, hemodynamics, and coagulation. Hemorheology is interested in aspects of blood and its components that determine blood's material properties, hence its flow, being aggregation, sedimentation, deformation, and volume fraction of erythrocytes and blood/plasma viscoelasticity. Hemodynamics covers the remaining determinants of blood flow that include blood pressure, cardiac output, and geometric/mechanical structure of vessels. Coagulation deals with the mechanisms, named primary and secondary hemostasis, aiming to stop blood flow in the case of bleeding.

Quantifying hemorheology, hemodynamics, and coagulation parameters is essential to understand health state of individuals, diagnose possible cardiovascular abnormalities, and monitor treatment strategies. In this regard, conventional benchtop instruments used in clinics have drawbacks in terms of workforce, lab space, sample volume, operation time, and cost. Although microfludic platforms have recently been developed to measure aforementioned parameters, they have a long way to go for clinical acceptance.

In this thesis, we proposed novel measurement methods to analyze hemorheology and coagulation parameters in microfluidic platforms that mimic in vivo hemodynamics conditions. The microfluidic platforms were all portable and designed as sample-in result-out systems. We demonstrated that optical analysis of erythrocyte dynamics in a 50 μl blood sample with physiological hematocrit levels can be used to measure aggregation, sedimentation rate, deformation of erythrocytes, blood suspending medium viscoelasticity, and coagulation time in less than 5 min. We validated our test results using real patient samples. If this thesis serves a single purpose, we hope this should be the idea of the possibility that all the hemorheology, hemodynamics, and coagulation parameters can simultaneously and rapidly be measured in physiologically relevant in vitro environments from a drop of blood even in resource-poor settings.

7.2 Future Directions

These promising studies can further be expanded into multiple directions. These include the following:

Hematocrit: Hematocrit is the volume percent of erythrocytes in blood with a normal range of 35% to 54%. Lower levels of hematocrit may signal malnutrition or anemia while elevated levels are indications of dehydration or plasma loss. Centrifugation is the most common method for hematocrit measurement. It is an important hemorheological property affecting the general flow characteristics of blood and oxygenation of body. Hematocrit level determines opacity of a blood

sample. Hence, optical transmission analysis of erythrocytes can be employed to measure this property.

Endothelization: In body, the internal surfaces of the vessels are covered by endothelial cells that form an interface between blood and vessel wall. Endothelization of microfluidic channels can be a means to better mimic in vivo circulation and can reveal the interaction between blood components and endothelial cells during various hematological processes.

Blood Storage: Transfusion of blood is a life-saving clinical operation performed for more than fifty years. In response to the growing global need, over hundred million units of blood are donated every year and kept in storage bags until their expiration date. Erythrocytes are stored at 4 °C for up to 42 days. Evidence has shown that during storage, erythrocytes undergo hemorheological alterations (erythrocyte storage lesion) including hemolysis and stiffness that might lead to complications like organ failure. Given the equipment and trained personnel limitations of blood banks, there is no standard procedure to check stored blood components against storage lesions. Hemorheological properties of stored blood samples can be analyzed concurrently for a complete hemorheological analysis.

Thromboembolism: Two main aspects of thrombotic conditions are thrombosis formation and embolism. Normally, blood coagulation is the body's response mechanism against bleeding, but there are cases where coagulation takes place unexpectedly in a vessel. The coagulation process can create a clot that may block the blood flow on the wound site. If the clot does not block the flow where it is formed, it does not imply that the risk is over. It is possible that a small piece of clot, named emboli, can leave the main clot and block a smaller vessel, potentially a capillary in brain or eye. In other words, understanding mechanical properties of a clot can help predict the risk of thromboembolism. Mechanical disturbance of a formed clot in a microfluidic channel segment and optical transmission analysis of the clot during disturbance can be used to quantify clot mechanical properties.

Contraction: Clot contraction is a hematological process where the formed blood clot actively gets squeezed in time to reduce its volume. The contraction is mainly caused by the activated platelets binding to the fibrin network and generating contractile forces, which changes clot organization. The stability of the contracted clot is also increased by Factor XIIIa that increases the stiffness of the clot with subtle-to-no morphology change via its cross-linking to fibrin alpha-chains. The contraction process consists of three stages: contraction initiation where the platelets are activated and bound to the fibrins for initial slight contraction, linear contraction where the platelets generate more contraction forces to alter the clot structure, and mechanical stabilization where the contraction continues, but the outcome is not as substantial as the previous stages. Long term optical transmission analysis of a stationary clot can be employed to quantify clot contraction.

Bibliography

[1] Z. Isiksacan, M. T. Guler, A. Kalantarifard, M. Asghari, and C. Elbuken, "Lab-on-a-chip platforms for disease detection and diagnosis," *Biosensors and Nanotechnology: Applications in Health Care Diagnostics*, pp. 155–181, 2018.

[2] J. Castillo-León and W. E. Svendsen, *Lab-on-a-Chip devices and micro-total analysis systems: a practical guide*. Springer, 2014.

[3] S. Terry, J. Jerman, and J. Angell, "A gas chromatographic air analyzer fabricated on a silicon wafer," *IEEE Transactions on Electron Devices*, vol. 26, no. 12, pp. 1880–1886, 1979.

[4] E. Bassous, H. Taub, and L. Kuhn, "Ink jet printing nozzle arrays etched in silicon," *Applied Physics Letters*, vol. 31, no. 2, pp. 135–137, 1977.

[5] A. Manz, N. Graber, and H. á. Widmer, "Miniaturized total chemical analysis systems: a novel concept for chemical sensing," *Sensors and actuators B: Chemical*, vol. 1, no. 1-6, pp. 244–248, 1990.

[6] D. C. Duffy, J. C. McDonald, O. J. Schueller, and G. M. Whitesides, "Rapid prototyping of microfluidic systems in poly (dimethylsiloxane)," *Analytical chemistry*, vol. 70, no. 23, pp. 4974–4984, 1998.

[7] Z. Isiksacan, M. T. Guler, B. Aydogdu, I. Bilican, and C. Elbuken, "Rapid fabrication of microfluidic pdms devices from reusable pdms molds using laser ablation," *Journal of Micromechanics and Microengineering*, vol. 26, no. 3, p. 035008, 2016.

[8] N. Convery and N. Gadegaard, "30 years of microfluidics," *Micro and Nano Engineering*, vol. 2, pp. 76–91, 2019.

[9] R. W. Peeling, K. K. Holmes, D. Mabey, and A. Ronald, "Rapid tests for sexually transmitted infections (stis): the way forward," *Sexually transmitted infections*, vol. 82, no. suppl 5, pp. v1–v6, 2006.

[10] R. Peeling and D. Mabey, "Point-of-care tests for diagnosing infections in the developing world," *Clinical microbiology and infection*, vol. 16, no. 8, pp. 1062–1069, 2010.

[11] S. Nahavandi, S. Baratchi, R. Soffe, S.-Y. Tang, S. Nahavandi, A. Mitchell, and K. Khoshmanesh, "Microfluidic platforms for biomarker analysis," *Lab on a Chip*, vol. 14, no. 9, pp. 1496–1514, 2014.

[12] D. J. Laser and J. G. Santiago, "A review of micropumps," *Journal of micromechanics and microengineering*, vol. 14, no. 6, p. R35, 2004.

[13] F. Abhari, H. Jaafar, and N. A. M. Yunus, "A comprehensive study of micropumps technologies," *Int. J. Electrochem. Sci*, vol. 7, no. 10, pp. 9765–9780, 2012.

[14] A. K. Au, H. Lai, B. R. Utela, and A. Folch, "Microvalves and micropumps for biomems," *Micromachines*, vol. 2, no. 2, pp. 179–220, 2011.

[15] K. W. Oh and C. H. Ahn, "A review of microvalves," *Journal of micromechanics and microengineering*, vol. 16, no. 5, p. R13, 2006.

[16] N.-T. Nguyen and Z. Wu, "Micromixers—a review," *Journal of micromechanics and microengineering*, vol. 15, no. 2, p. R1, 2004.

[17] M. A. Unger, H.-P. Chou, T. Thorsen, A. Scherer, and S. R. Quake, "Monolithic microfabricated valves and pumps by multilayer soft lithography," *Science*, vol. 288, no. 5463, pp. 113–116, 2000.

[18] D. Mark, S. Haeberle, G. Roth, F. Von Stetten, and R. Zengerle, "From microfluidic application to nanofluidic phenomena issue," *Chem. Soc. Rev*, vol. 39, pp. 1153–1182, 2010.

[19] D. M. Cate, J. A. Adkins, J. Mettakoonpitak, and C. S. Henry, "Recent developments in paper-based microfluidic devices," *Analytical chemistry*, vol. 87, no. 1, pp. 19–41, 2014.

[20] D. A. Bruzewicz, M. Reches, and G. M. Whitesides, "Low-cost printing of poly (dimethylsiloxane) barriers to define microchannels in paper," *Analytical chemistry*, vol. 80, no. 9, pp. 3387–3392, 2008.

[21] E. Carrilho, A. W. Martinez, and G. M. Whitesides, "Understanding wax printing: a simple micropatterning process for paper-based microfluidics," *Analytical chemistry*, vol. 81, no. 16, pp. 7091–7095, 2009.

[22] J. Hu, S. Wang, L. Wang, F. Li, B. Pingguan-Murphy, T. J. Lu, and F. Xu, "Advances in paper-based point-of-care diagnostics," *Biosensors and Bioelectronics*, vol. 54, pp. 585–597, 2014.

[23] Y. Lu, W. Shi, L. Jiang, J. Qin, and B. Lin, "Rapid prototyping of paper-based microfluidics with wax for low-cost, portable bioassay," *Electrophoresis*, vol. 30, no. 9, pp. 1497–1500, 2009.

[24] J. Wang, M. R. N. Monton, X. Zhang, C. D. Filipe, R. Pelton, and J. D. Brennan, "Hydrophobic sol–gel channel patterning strategies for paper-based microfluidics," *Lab on a Chip*, vol. 14, no. 4, pp. 691–695, 2014.

[25] D. Robert, "Device for grinding broken paper.," Sept. 2 1902. US Patent App. 730,617.

[26] H. Yagoda, "Applications of confined spot tests in analytical chemistry: preliminary paper," *Industrial & Engineering Chemistry Analytical Edition*, vol. 9, no. 2, pp. 79–82, 1937.

[27] A. M. López-Marzo and A. Merkoçi, "Paper-based sensors and assays: a success of the engineering design and the convergence of knowledge areas," *Lab on a Chip*, vol. 16, no. 17, pp. 3150–3176, 2016.

[28] S.-Y. Teh, R. Lin, L.-H. Hung, and A. P. Lee, "Droplet microfluidics," *Lab on a Chip*, vol. 8, no. 2, pp. 198–220, 2008.

[29] A. M. Foudeh, T. F. Didar, T. Veres, and M. Tabrizian, "Microfluidic designs and techniques using lab-on-a-chip devices for pathogen detection for point-of-care diagnostics," *Lab on a Chip*, vol. 12, no. 18, pp. 3249–3266, 2012.

[30] B. G. De Geest, J. P. Urbanski, T. Thorsen, J. Demeester, and S. C. De Smedt, "Synthesis of monodisperse biodegradable microgels in microfluidic devices," *Langmuir*, vol. 21, no. 23, pp. 10275–10279, 2005.

[31] M. He, C. Sun, and D. T. Chiu, "Concentrating solutes and nanoparticles within individual aqueous microdroplets," *Analytical chemistry*, vol. 76, no. 5, pp. 1222–1227, 2004.

[32] M. He, J. S. Edgar, G. D. Jeffries, R. M. Lorenz, J. P. Shelby, and D. T. Chiu, "Selective encapsulation of single cells and subcellular organelles into picoliter-and femtoliter-volume droplets," *Analytical chemistry*, vol. 77, no. 6, pp. 1539–1544, 2005.

[33] L.-H. Hung, K. M. Choi, W.-Y. Tseng, Y.-C. Tan, K. J. Shea, and A. P. Lee, "Alternating droplet generation and controlled dynamic droplet fusion in microfluidic device for cds nanoparticle synthesis," *Lab on a Chip*, vol. 6, no. 2, pp. 174–178, 2006.

[34] R. Burger, D. Kirby, M. Glynn, C. Nwankire, M. O'Sullivan, J. Siegrist, D. Kinahan, G. Aguirre, G. Kijanka, R. A. Gorkin III, *et al.*, "Centrifugal microfluidics for cell analysis," *Current opinion in chemical biology*, vol. 16, no. 3-4, pp. 409–414, 2012.

[35] M. Tang, G. Wang, S.-K. Kong, and H.-P. Ho, "A review of biomedical centrifugal microfluidic platforms," *Micromachines*, vol. 7, no. 2, p. 26, 2016.

[36] M. Focke, F. Stumpf, B. Faltin, P. Reith, D. Bamarni, S. Wadle, C. Müller, H. Reinecke, J. Schrenzel, P. Francois, *et al.*, "Microstructuring of polymer films for sensitive genotyping by real-time pcr on a centrifugal microfluidic platform," *Lab on a Chip*, vol. 10, no. 19, pp. 2519–2526, 2010.

[37] W. Gao, S. Emaminejad, H. Y. Y. Nyein, S. Challa, K. Chen, A. Peck, H. M. Fahad, H. Ota, H. Shiraki, D. Kiriya, *et al.*, "Fully integrated wearable sensor arrays for multiplexed in situ perspiration analysis," *Nature*, vol. 529, no. 7587, p. 509, 2016.

[38] G. Appelboom, E. Camacho, M. E. Abraham, S. S. Bruce, E. L. Dumont, B. E. Zacharia, R. D'Amico, J. Slomian, J. Y. Reginster, O. Bruyère, *et al.*, "Smart wearable body sensors for patient self-assessment and monitoring," *Archives of public health*, vol. 72, no. 1, p. 28, 2014.

[39] A. J. Bandodkar and J. Wang, "Non-invasive wearable electrochemical sensors: a review," *Trends in biotechnology*, vol. 32, no. 7, pp. 363–371, 2014.

[40] B. Zhang, A. Korolj, B. F. L. Lai, and M. Radisic, "Advances in organ-on-a-chip engineering," *Nature Reviews Materials*, vol. 3, no. 8, pp. 257–278, 2018.

[41] E. N. Marieb and K. Hoehn, *Human anatomy & physiology*. Pearson Education, 2007.

[42] T. W. Secomb, "Blood flow in the microcirculation," *Annual Review of Fluid Mechanics*, vol. 49, pp. 443–461, 2017.

[43] B. Sebastian and P. S. Dittrich, "Microfluidics to mimic blood flow in health and disease," *Annual review of fluid mechanics*, vol. 50, pp. 483–504, 2018.

[44] Y. Qiu, D. R. Myers, and W. A. Lam, "The biophysics and mechanics of blood from a materials perspective," *Nature Reviews Materials*, vol. 4, no. 5, pp. 294–311, 2019.

[45] G. Tomaiuolo, "Biomechanical properties of red blood cells in health and disease towards microfluidics," *Biomicrofluidics*, vol. 8, no. 5, p. 051501, 2014.

[46] A. S. Smith, R. B. Nowak, S. Zhou, M. Giannetto, D. S. Gokhin, J. Papoin, I. C. Ghiran, L. Blanc, J. Wan, and V. M. Fowler, "Myosin iia interacts

with the spectrin-actin membrane skeleton to control red blood cell membrane curvature and deformability," *Proceedings of the National Academy of Sciences*, vol. 115, no. 19, pp. E4377–E4385, 2018.

[47] H. F. Bunn, B. G. Forget, *et al.*, *Hemoglobin: molecular, genetic and clinical aspects*. WB Saunders Company Philadelphia, 1986.

[48] W. E. C. on Malaria and W. H. Organization, *WHO expert committee on malaria: twentieth report*. No. 892, World Health Organization, 2000.

[49] Y. J. Kang and S.-J. Lee, "In vitro and ex vivo measurement of the biophysical properties of blood using microfluidic platforms and animal models," *Analyst*, vol. 143, no. 12, pp. 2723–2749, 2018.

[50] O. Baskurt, B. Neu, and H. J. Meiselman, *Red blood cell aggregation*. CRC Press, 2011.

[51] Z. Isiksacan, O. Erel, and C. Elbuken, "A portable microfluidic system for rapid measurement of the erythrocyte sedimentation rate," *Lab on a Chip*, vol. 16, no. 24, pp. 4682–4690, 2016.

[52] L. Lanotte, J. Mauer, S. Mendez, D. A. Fedosov, J.-M. Fromental, V. Claveria, F. Nicoud, G. Gompper, and M. Abkarian, "Red cells' dynamic morphologies govern blood shear thinning under microcirculatory flow conditions," *Proceedings of the National Academy of Sciences*, vol. 113, no. 47, pp. 13289–13294, 2016.

[53] G. R. Cokelet, "Rheology and hemodynamics," *Annual Review of Physiology*, vol. 42, no. 1, pp. 311–322, 1980.

[54] S. Chien, "Shear dependence of effective cell volume as a determinant of blood viscosity," *Science*, vol. 168, no. 3934, pp. 977–979, 1970.

[55] T. M. Geislinger and T. Franke, "Hydrodynamic lift of vesicles and red blood cells in flow—from fåhræus & lindqvist to microfluidic cell sorting," *Advances in colloid and interface science*, vol. 208, pp. 161–176, 2014.

[56] T. G. Mezger, *The rheology handbook: for users of rotational and oscillatory rheometers*. Vincentz Network GmbH & Co KG, 2006.

[57] T. W. Secomb, "Hemodynamics," *Comprehensive Physiology*, vol. 6, no. 2, pp. 975–1003, 2011.

[58] G. B. Thurston, "Viscoelasticity of human blood," *Biophysical journal*, vol. 12, no. 9, pp. 1205–1217, 1972.

[59] M. Brust, C. Schaefer, R. Doerr, L. Pan, M. Garcia, P. Arratia, and C. Wagner, "Rheology of human blood plasma: Viscoelastic versus newtonian behavior," *Physical review letters*, vol. 110, no. 7, p. 078305, 2013.

[60] P. Kelly, "Solid mechanics part i: An introduction to solid mechanics," *A Creative Commons Attributions, Mountain View, CA*, vol. 94042, 2013.

[61] R. Lakes and R. S. Lakes, *Viscoelastic materials*. Cambridge university press, 2009.

[62] A. Sennaroglu, *Photonics and laser engineering: principles, devices, and applications*. McGraw-Hill, 2010.

[63] L. J. Vandergriff *et al.*, "Nature and properties of light," *Fundam. Photonics*, pp. 1–38, 2008.

[64] A. B. Hertzman, "Photoelectric plethysmography of the fingers and toes in man," *Proceedings of the Society for Experimental Biology and Medicine*, vol. 37, no. 3, pp. 529–534, 1937.

[65] M. C. Meinke, G. J. Müller, J. Helfmann, and M. Friebel, "Optical properties of platelets and blood plasma and their influence on the optical behavior of whole blood in the visible to near infrared wavelength range," *Journal of biomedical optics*, vol. 12, no. 1, p. 014024, 2007.

[66] O. K. Baskurt, M. Uyuklu, S. Ozdem, and H. J. Meiselman, "Measurement of red blood cell aggregation in disposable capillary tubes," *Clinical hemorheology and microcirculation*, vol. 47, no. 4, pp. 295–305, 2011.

[67] L.-G. Lindberg and P. A. Oberg, "Optical properties of blood in motion," *Optical Engineering*, vol. 32, no. 2, pp. 253–258, 1993.

[68] Z. Isiksacan, M. Asghari, and C. Elbuken, "A microfluidic erythrocyte sedimentation rate analyzer using rouleaux formation kinetics," *Microfluidics and Nanofluidics*, vol. 21, no. 3, p. 44, 2017.

[69] H.-j. Lim, Y.-J. Lee, J.-H. Nam, S. Chung, and S. Shin, "Temperature-dependent threshold shear stress of red blood cell aggregation," *Journal of biomechanics*, vol. 43, no. 3, pp. 546–550, 2010.

[70] M. Rampling, H. Meiselman, B. Neu, and O. Baskurt, "Influence of cell-specific factors on red blood cell aggregation," *Biorheology*, vol. 41, no. 2, pp. 91–112, 2004.

[71] J. K. Armstrong, H. J. Meiselman, R. B. Wenby, and T. C. Fisher, "Modulation of red blood cell aggregation and blood viscosity by the covalent attachment of pluronic copolymers," *Biorheology*, vol. 38, no. 2, 3, pp. 239–247, 2001.

[72] G. Barshtein, I. Tamir, and S. Yedgar, "Red blood cell rouleaux formation in dextran solution: dependence on polymer conformation," *European biophysics journal*, vol. 27, no. 2, pp. 177–181, 1998.

[73] B. Neu, R. Wenby, and H. J. Meiselman, "Effects of dextran molecular weight on red blood cell aggregation," *Biophysical journal*, vol. 95, no. 6, pp. 3059–3065, 2008.

[74] J. J. Bishop, A. S. Popel, M. Intaglietta, and P. C. Johnson, "Rheological effects of red blood cell aggregation in the venous network: a review of recent studies," *Biorheology*, vol. 38, no. 2, 3, pp. 263–274, 2001.

[75] S. Chien, "Biophysical behavior of red cells in suspensions," *The red blood cell*, vol. 2, no. 4, pp. 1031–133, 1975.

[76] S. Asakura and F. Oosawa, "On interaction between two bodies immersed in a solution of macromolecules," *The Journal of Chemical Physics*, vol. 22, no. 7, pp. 1255–1256, 1954.

[77] A. Dima, D. Opris, C. Jurcut, and C. Baicus, "Is there still a place for erythrocyte sedimentation rate and c-reactive protein in systemic lupus erythematosus?," *Lupus*, vol. 25, no. 11, pp. 1173–1179, 2016.

[78] M. M. Wintrobe, "A standardised technique for the blood sedimentation test," *Am. J. Med. Sci.*, vol. 189, pp. 102–115, 1935.

[79] A. Westergren, "Studies of the suspension stability of the blood in pulmonary tuberculosis," *Acta Medica Scandinavica*, vol. 54, no. 1, pp. 247–282, 1921.

[80] G. G. Stokes, *On the effect of the internal friction of fluids on the motion of pendulums*, vol. 9. Pitt Press Cambridge, 1851.

[81] T.-F. Hong, W.-J. Ju, M.-C. Wu, C.-H. Tai, C.-H. Tsai, and L.-M. Fu, "Rapid prototyping of pmma microfluidic chips utilizing a co 2 laser," *Microfluidics and nanofluidics*, vol. 9, no. 6, pp. 1125–1133, 2010.

[82] M. Uyuklu, M. Canpolat, H. J. Meiselman, and O. K. Baskurt, "Wavelength selection in measuring red blood cell aggregation based on light transmittance," *Journal of biomedical optics*, vol. 16, no. 11, p. 117006, 2011.

[83] M. Anand and K. Rajagopal, "A shear-thinning viscoelastic fluid model for describing the flow of blood," *Int. J. Cardiovasc. Med. Sci*, vol. 4, no. 2, pp. 59–68, 2004.

[84] M. M. Cross, "Rheology of non-newtonian fluids: a new flow equation for pseudoplastic systems," *Journal of colloid science*, vol. 20, no. 5, pp. 417–437, 1965.

[85] F. J. Walburn and D. J. Schneck, "A constitutive equation for whole human blood," *Biorheology*, vol. 13, no. 3, pp. 201–210, 1976.

[86] P. J. Carreau, I. F. MacDonald, and R. B. Bird, "A nonlinear viscoelastic model for polymer solutions and melts—ii," *Chemical Engineering Science*, vol. 23, no. 8, pp. 901–911, 1968.

[87] B. Neu, "Red blood cell aggregation. in 'handbook of hemorheology and hemodynamics'.(eds ok baskurt, mr hardeman, mw rampling and hj meiselman.) pp. 114–136," 2007.

[88] H. Amini, W. Lee, and D. Di Carlo, "Inertial microfluidic physics," *Lab on a Chip*, vol. 14, no. 15, pp. 2739–2761, 2014.

[89] G. Tomaiuolo, M. Barra, V. Preziosi, A. Cassinese, B. Rotoli, and S. Guido, "Microfluidics analysis of red blood cell membrane viscoelasticity," *Lab on a Chip*, vol. 11, no. 3, pp. 449–454, 2011.

[90] K.-M. Jan and S. Chien, "Role of surface electric charge in red blood cell interactions," *The Journal of general physiology*, vol. 61, no. 5, pp. 638–654, 1973.

[91] G. B. Nash and H. J. Meiselman, "Alteration of red cell membrane viscoelasticity by heat treatment: effect on cell deformability and suspension viscosity," *Biorheology*, vol. 22, no. 1, pp. 73–84, 1985.

[92] N. Maeda, K. Imaizumi, M. Sekiya, and T. Shiga, "Rheological characteristics of desialylated erythrocytes in relation to fibrinogen-induced aggregation," *Biochimica et Biophysica Acta (BBA)-Biomembranes*, vol. 776, no. 1, pp. 151–158, 1984.

[93] N. Maeda and T. Shiga, "Inhibition and acceleration of erythrocyte aggregation induced by small macromolecules," *Biochimica et Biophysica Acta (BBA)-General Subjects*, vol. 843, no. 1-2, pp. 128–136, 1985.

[94] M. Boynard and J. Lelievre, "Size determination of red blood cell aggregates induced by dextran using ultrasound backscattering phenomenon," *Biorheology*, vol. 27, no. 1, pp. 39–46, 1990.

[95] N. Maeda, M. Seike, T. Nakajima, Y. Izumida, M. Sekiya, and T. Shiga, "Contribution of glycoproteins to fibrinogen-induced aggregation of erythrocytes," *Biochimica et Biophysica Acta (BBA)-Biomembranes*, vol. 1022, no. 1, pp. 72–78, 1990.

[96] S. Shin, J.-H. Nam, J.-X. Hou, and J.-S. Suh, "A transient, microfluidic approach to the investigation of erythrocyte aggregation: the threshold shear-stress for erythrocyte disaggregation," *Clinical hemorheology and microcirculation*, vol. 42, no. 2, pp. 117–125, 2009.

[97] O. K. Baskurt, A. Temiz, and H. J. Meiselman, "Red blood cell aggregation in experimental sepsis," *Journal of Laboratory and Clinical Medicine*, vol. 130, no. 2, pp. 183–190, 1997.

[98] O. K. Baskurt and H. J. Meiselman, "Erythrocyte aggregation: basic aspects and clinical importance," *Clinical hemorheology and microcirculation*, vol. 53, no. 1-2, pp. 23–37, 2013.

[99] B. S. Bull and J. D. Brailsford, "The zeta sedimentation ratio," *Blood*, vol. 40, no. 4, pp. 550–559, 1972.

[100] S. Forconi, C. Rossi, M. Guerrini, R. Cappelli, M. Materazzi, D. Pieragalli, S. Pecchi, A. Acciavatti, C. Galigani, and T. Di Perri, "Action of cigarette smoking on microcirculation. effects on some haemorheological, haemodynamic and metabolic parameters.," *Clinical Hemorheology and Microcirculation*, vol. 6, no. 2, pp. 175–184, 1986.

[101] O. K. Baskurt, H. Meiselman, and E. Kayar, "Measurement of red blood cell aggregation in a "plate–plate" shearing system by analysis of light transmission," *Clinical hemorheology and microcirculation*, vol. 19, no. 4, pp. 307–314, 1998.

[102] M. Hardeman, J. Dobbe, and C. Ince, "The laser-assisted optical rotational cell analyzer (lorca) as red blood cell aggregometer," *Clinical hemorheology and microcirculation*, vol. 25, no. 1, pp. 1–11, 2001.

[103] O. K. Baskurt, M. Uyuklu, M. R. Hardeman, and H. J. Meiselman, "Photometric measurements of red blood cell aggregation: light transmission versus light reflectance," *Journal of biomedical optics*, vol. 14, no. 5, p. 054044, 2009.

[104] O. K. Baskurt, M. Uyuklu, P. Ulker, M. Cengiz, N. Nemeth, T. Alexy, S. Shin, M. R. Hardeman, and H. J. Meiselman, "Comparison of three instruments for measuring red blood cell aggregation," *Clinical hemorheology and microcirculation*, vol. 43, no. 4, pp. 283–298, 2009.

[105] E. Hysi, R. K. Saha, and M. C. Kolios, "On the use of photoacoustics to detect red blood cell aggregation," *Biomedical optics express*, vol. 3, no. 9, pp. 2326–2338, 2012.

[106] S. Chen, G. Barshtein, B. Gavish, Y. Mahler, and S. Yedgar, "Monitoring of red blood cell aggregability in a flow-chamber by computerized image analysis," *Clinical Hemorheology and Microcirculation*, vol. 14, no. 4, pp. 497–508, 1994.

[107] S. Chen, B. Gavish, S. Zhang, Y. Mahler, and S. Yedgar, "Monitoring of erythrocyte aggregate morphology under flow by computerized image analysis," *Biorheology*, vol. 32, no. 4, pp. 487–496, 1995.

[108] G. Barshtein, D. Wajnblum, and S. Yedgar, "Kinetics of linear rouleaux formation studied by visual monitoring of red cell dynamic organization," *Biophysical journal*, vol. 78, no. 5, pp. 2470–2474, 2000.

[109] S. Jayavanth and M. Singh, "Computerized analysis of erythrocyte aggregation from sequential video-microscopic images under gravitational sedimentation," *ITBM-RBM*, vol. 25, no. 2, pp. 67–74, 2004.

[110] B. Rappaz, P. Marquet, E. Cuche, Y. Emery, C. Depeursinge, and P. J. Magistretti, "Measurement of the integral refractive index and dynamic cell morphometry of living cells with digital holographic microscopy," *Optics express*, vol. 13, no. 23, pp. 9361–9373, 2005.

[111] S. Mavandadi, S. Feng, F. Yu, S. Dimitrov, K. Nielsen-Saines, W. R. Prescott, and A. Ozcan, "A mathematical framework for combining decisions of multiple experts toward accurate and remote diagnosis of malaria using tele-microscopy," *PloS one*, vol. 7, no. 10, p. e46192, 2012.

[112] T. Kim, R. Zhou, M. Mir, S. D. Babacan, P. S. Carney, L. L. Goddard, and G. Popescu, "White-light diffraction tomography of unlabelled live cells," *Nature Photonics*, vol. 8, no. 3, p. 256, 2014.

[113] D. Dannhauser, D. Rossi, F. Causa, P. Memmolo, A. Finizio, T. Wriedt, J. Hellmers, Y. Eremin, P. Ferraro, and P. Netti, "Optical signature of erythrocytes by light scattering in microfluidic flows," *Lab on a Chip*, vol. 15, no. 16, pp. 3278–3285, 2015.

[114] L. Miccio, P. Memmolo, F. Merola, P. Netti, and P. Ferraro, "Red blood cell as an adaptive optofluidic microlens," *Nature communications*, vol. 6, p. 6502, 2015.

[115] A. Grzybowski and J. Sak, "Edmund biernacki (1866-1911): Discoverer of the erythrocyte sedimentation rate. on the 100th anniversary of his death," *Clinics in dermatology*, vol. 29, no. 6, pp. 697–703, 2011.

[116] M. R. Cheema and S. M. Ismaeel, "Temporal arteritis with erythrocyte sedimentation rate¡ 50 mm/h: a clinical reminder," *Clinical interventions in aging*, vol. 11, p. 185, 2016.

[117] R. L. Wong and J. H. Korn, "Temporal arteritis without an elevated erythrocyte sedimentation rate: case report and review of the literature," *The American journal of medicine*, vol. 80, no. 5, pp. 959–964, 1986.

[118] H. C. Sox and M. H. Liang, "Diagnostic decision: the erythrocyte sedimentation rate: guidelines for rational use," *Annals of internal medicine*, vol. 104, no. 4, pp. 515–523, 1986.

[119] F. Wolfe and K. Michaud, "The clinical and research significance of the erythrocyte sedimentation rate.," *The Journal of Rheumatology*, vol. 21, no. 7, pp. 1227–1237, 1994.

[120] M. Plebani and E. Piva, "Erythrocyte sedimentation rate: use of fresh blood for quality control," *American journal of clinical pathology*, vol. 117, no. 4, pp. 621–626, 2002.

[121] A. S. Singh, V. Atam, B. E. Yathish, L. Das, and S. Koonwar, "Role of erythrocyte sedimentation rate in ischemic stroke as an inflammatory marker of carotid atherosclerosis," *Journal of neurosciences in rural practice*, vol. 5, no. 1, p. 40, 2014.

[122] M. B. Andresdottir, N. Sigfusson, H. Sigvaldason, and V. Gudnason, "Erythrocyte sedimentation rate, an independent predictor of coronary heart disease in men and women: The reykjavik study," *American journal of epidemiology*, vol. 158, no. 9, pp. 844–851, 2003.

[123] J.-E. Johansson, T. Sigurdsson, L. Holmberg, and R. Bergstrom, "Erythrocyte sedimentation rate as a tumor marker in human prostatic cancer. an analysis of prognostic factors in 300 population-based consecutive cases," *Cancer*, vol. 70, no. 6, pp. 1556–1563, 1992.

[124] S. E. Bedell and B. T. Bush, "Erythrocyte sedimentation rate. from folklore to facts," *The American journal of medicine*, vol. 78, no. 6, pp. 1001–1009, 1985.

[125] B. Bull, M. Caswell, E. Ernst, J. Jou, A. Kallner, J. Koepke, S. Lewis, G. Lowe, M. Rampling, and J. Stuart, "Icsh recommendations for measurement of erythrocyte sedimentation-rate," *Journal of Clinical Pathology*, vol. 46, no. 3, pp. 198–203, 1993.

[126] C. D. Chin, V. Linder, and S. K. Sia, "Commercialization of microfluidic point-of-care diagnostic devices," *Lab on a Chip*, vol. 12, no. 12, pp. 2118–2134, 2012.

[127] C. van Berkel, J. D. Gwyer, S. Deane, N. Green, J. Holloway, V. Hollis, and H. Morgan, "Integrated systems for rapid point of care (poc) blood cell analysis," *Lab on a Chip*, vol. 11, no. 7, pp. 1249–1255, 2011.

[128] M. Plebani, S. De Toni, M. C. Sanzari, D. Bernardi, and E. Stockreiter, "The test 1 automated system: a new method for measuring the erythrocyte sedimentation rate," *American journal of clinical pathology*, vol. 110, no. 3, pp. 334–340, 1998.

[129] N. Boğdaycioğlu, F. M. Yilmaz, S. Sezer, and E. Oğuz, "Comparison of ised and ves-matic cube 200 erythrocyte sedimentation rate measurements with westergren method," *Journal of clinical laboratory analysis*, vol. 29, no. 5, pp. 397–404, 2015.

[130] M. R. Hardeman, M. Levitus, A. Pelliccia, and A. A. Bouman, "Test 1 analyser for determination of esr. 2. experimental evaluation and comparison with rbc aggregometry," *Scandinavian journal of clinical and laboratory investigation*, vol. 70, no. 1, pp. 26–32, 2010.

[131] A. L. Copley and G. V. Seaman, "The meaning of the terms rheology, biorheology and hemorheology," *Clinical Hemorheology and Microcirculation*, vol. 1, no. 2, pp. 117–119, 1981.

[132] Z. Xu, Y. Zheng, X. Wang, N. Shehata, C. Wang, and Y. Sun, "Stiffness increase of red blood cells during storage," *Microsystems & Nanoengineering*, vol. 4, p. 17103, 2018.

[133] Z. Xu, W. Dou, C. Wang, and Y. Sun, "Stiffness and atp recovery of stored red blood cells in serum," *Microsystems & nanoengineering*, vol. 5, no. 1, pp. 1–9, 2019.

[134] Y. Kang, "Microfluidic-based technique for measuring rbc aggregation and blood viscosity in a continuous and simultaneous fashion," *Micromachines*, vol. 9, no. 9, p. 467, 2018.

[135] Y. J. Kang, "Periodic and simultaneous quantification of blood viscosity and red blood cell aggregation using a microfluidic platform under in-vitro closed-loop circulation," *Biomicrofluidics*, vol. 12, no. 2, p. 024116, 2018.

[136] H. Turlier, D. A. Fedosov, B. Audoly, T. Auth, N. S. Gov, C. Sykes, J.-F. Joanny, G. Gompper, and T. Betz, "Equilibrium physics breakdown reveals the active nature of red blood cell flickering," *Nature Physics*, vol. 12, no. 5, p. 513, 2016.

[137] J. Duez, M. Carucci, I. Garcia-Barbazan, M. Corral, O. Perez, J. L. Presa, B. Henry, C. Roussel, P. A. Ndour, N. B. Rosa, *et al.*, "High-throughput microsphiltration to assess red blood cell deformability and screen for malaria transmission–blocking drugs," *nature protocols*, vol. 13, no. 6, p. 1362, 2018.

[138] G. Artmann, C. Kelemen, D. Porst, G. Büldt, and S. Chien, "Temperature transitions of protein properties in human red blood cells," *Biophysical journal*, vol. 75, no. 6, pp. 3179–3183, 1998.

[139] P.-H. Wu, D. R.-B. Aroush, A. Asnacios, W.-C. Chen, M. E. Dokukin, B. L. Doss, P. Durand-Smet, A. Ekpenyong, J. Guck, N. V. Guz, *et al.*, "A comparison of methods to assess cell mechanical properties," *Nature methods*, vol. 15, pp. 491–498, 2018.

[140] B. Fregin, F. Czerwinski, D. Biedenweg, S. Girardo, S. Gross, K. Aurich, and O. Otto, "High-throughput single-cell rheology in complex samples by dynamic real-time deformability cytometry," *Nature communications*, vol. 10, no. 1, p. 415, 2019.

[141] M. Dao, C. T. Lim, and S. Suresh, "Mechanics of the human red blood cell deformed by optical tweezers," *Journal of the Mechanics and Physics of Solids*, vol. 51, no. 11-12, pp. 2259–2280, 2003.

[142] Q. Guo, S. J. Reiling, P. Rohrbach, and H. Ma, "Microfluidic biomechanical assay for red blood cells parasitized by plasmodium falciparum," *Lab on a Chip*, vol. 12, no. 6, pp. 1143–1150, 2012.

[143] H. W. Hou, A. A. S. Bhagat, A. G. L. Chong, P. Mao, K. S. W. Tan, J. Han, and C. T. Lim, "Deformability based cell margination—a simple microfluidic design for malaria-infected erythrocyte separation," *Lab on a Chip*, vol. 10, no. 19, pp. 2605–2613, 2010.

[144] Y. Zheng, E. Shojaei-Baghini, A. Azad, C. Wang, and Y. Sun, "High-throughput biophysical measurement of human red blood cells," *Lab on a Chip*, vol. 12, no. 14, pp. 2560–2567, 2012.

[145] M. E. Safar, "Arterial stiffness as a risk factor for clinical hypertension," *Nature Reviews Cardiology*, vol. 15, no. 2, p. 97, 2018.

[146] S. Varchanis, Y. Dimakopoulos, C. Wagner, and J. Tsamopoulos, "How viscoelastic is human blood plasma?," *Soft Matter*, vol. 14, no. 21, pp. 4238–4251, 2018.

[147] A. Daly, J. S. Raval, J. H. Waters, M. H. Yazer, and M. V. Kameneva, "Effect of blood bank storage on the rheological properties of male and female donor red blood cells," *Clinical hemorheology and microcirculation*, vol. 56, no. 4, pp. 337–345, 2014.

[148] H. Huang, M. L. Yarmush, and O. B. Usta, "Long-term deep-supercooling of large-volume water and red cell suspensions via surface sealing with immiscible liquids," *Nature communications*, vol. 9, no. 1, p. 3201, 2018.

[149] A. D'Alessandro, G. Liumbruno, G. Grazzini, and L. Zolla, "Red blood cell storage: the story so far," *Blood Transfusion*, vol. 8, no. 2, p. 82, 2010.

[150] G. Oster and R. Zalusky, "Shape transformation of erythrocytes determined by light scattering changes associated with relaxation of particle orientation," *Biophysical journal*, vol. 14, no. 2, pp. 124–129, 1974.

[151] A. H. Raffiee, S. Dabiri, and A. M. Ardekani, "Elasto-inertial migration of deformable capsules in a microchannel," *Biomicrofluidics*, vol. 11, no. 6, p. 064113, 2017.

[152] A. H. Raffiee, S. Dabiri, and A. M. Ardekani, "Suspension of deformable particles in newtonian and viscoelastic fluids in a microchannel," *Microfluidics and Nanofluidics*, vol. 23, no. 2, p. 22, 2019.

[153] G. Holzner, S. Stavrakis, and A. DeMello, "Elasto-inertial focusing of mammalian cells and bacteria using low molecular, low viscosity peo solutions," *Analytical chemistry*, vol. 89, no. 21, pp. 11653–11663, 2017.

[154] T. Go, H. Byeon, and S. J. Lee, "Focusing and alignment of erythrocytes in a viscoelastic medium," *Scientific reports*, vol. 7, p. 41162, 2017.

[155] A. H. Raffiee, S. Dabiri, and A. M. Ardekani, "Deformation and buckling of microcapsules in a viscoelastic matrix," *Physical Review E*, vol. 96, no. 3, p. 032603, 2017.

[156] P. Yue, J. J. Feng, C. Liu, and J. Shen, "Viscoelastic effects on drop deformation in steady shear," *Journal of Fluid Mechanics*, vol. 540, pp. 427–437, 2005.

[157] Z. Isiksacan, N. Hastar, O. Erel, and C. Elbuken, "An optofluidic point-of-care device for quantitative investigation of erythrocyte aggregation during coagulation," *Sensors and Actuators A: Physical*, vol. 281, pp. 24–30, 2018.

[158] B. Furie and B. C. Furie, "The molecular basis of blood coagulation," *Cell*, vol. 53, no. 4, pp. 505–518, 1988.

[159] J. P. Antovic and M. Blombäck, *Essential guide to blood coagulation*. Wiley Online Library, 2013.

[160] P. Toulon, Y. Ozier, A. Ankri, M.-H. Fléron, G. Leroux, and C. M. Samama, "Point-of-care versus central laboratory coagulation testing during haemorrhagic surgery," *Thrombosis and haemostasis*, vol. 101, no. 02, pp. 394–401, 2009.

[161] S. A. Kozek-Langenecker, "Perioperative coagulation monitoring," *Best Practice & Research Clinical Anaesthesiology*, vol. 24, no. 1, pp. 27–40, 2010.

[162] G. Lowe and A. Rumley, "The relevance of coagulation in cardiovascular disease: what do the biomarkers tell us?," *Thrombosis and haemostasis*, vol. 112, no. 11, pp. 860–867, 2014.

[163] R. Mathews and R. M. Issac, "Bleeding and coagulation disorders," in *Clinical Pathways in Emergency Medicine*, pp. 417–428, Springer, 2016.

[164] B. Collins and C. Hollidge, "Antithrombotic drug market," *Nature Reviews Drug Discovery*, vol. 2, no. 1, pp. 11–13, 2003.

[165] W. S. Baker, K. J. Albright, M. Berman, H. Spratt, P. A. Mann, J. Unabia, and J. R. Petersen, "Poct pt inr—is it adequate for patient care? a comparison of the roche coaguchek xs vs. stago star vs. siemens bcs in patients routinely seen in an anticoagulation clinic," *Clinica Chimica Acta*, vol. 472, pp. 139–145, 2017.

[166] L. F. Harris, V. Castro-López, and A. J. Killard, "Coagulation monitoring devices: Past, present, and future at the point of care," *TrAC Trends in Analytical Chemistry*, vol. 50, pp. 85–95, 2013.

[167] H. Li, D. Han, G. Pauletti, and A. Steckl, "Blood coagulation screening using a paper-based microfluidic lateral flow device," *Lab on a Chip*, vol. 14, no. 20, pp. 4035–4041, 2014.

[168] F. Padovani, J. Duffy, and M. Hegner, "Microrheological coagulation assay exploiting micromechanical resonators," *Analytical chemistry*, vol. 89, no. 1, pp. 751–758, 2016.

[169] K. F. Lei, K.-H. Chen, P.-H. Tsui, and N.-M. Tsang, "Real-time electrical impedimetric monitoring of blood coagulation process under temperature and hematocrit variations conducted in a microfluidic chip," *PLoS One*, vol. 8, no. 10, p. e76243, 2013.

[170] M. Andersson, J. Andersson, A. Sellborn, M. Berglin, B. Nilsson, and H. Elwing, "Quartz crystal microbalance-with dissipation monitoring (qcm-d) for real time measurements of blood coagulation density and immune complement activation on artificial surfaces," *Biosensors and Bioelectronics*, vol. 21, no. 1, pp. 79–86, 2005.

[171] K. M. Hansson, K. Johansen, J. Wetterö, G. Klenkar, J. Benesch, I. Lundström, T. L. Lindahl, and P. Tengvall, "Surface plasmon resonance detection of blood coagulation and platelet adhesion under venous and arterial shear conditions," *Biosensors and Bioelectronics*, vol. 23, no. 2, pp. 261–268, 2007.

[172] M. T. Guler, Z. Isiksacan, M. Serhatlioglu, and C. Elbuken, "Self-powered disposable prothrombin time measurement device with an integrated effervescent pump," *Sensors and Actuators B: Chemical*, vol. 273, pp. 350–357, 2018.

[173] R. Luddington, "Thrombelastography/thromboelastometry," *Clinical & Laboratory Haematology*, vol. 27, no. 2, pp. 81–90, 2005.

[174] P. Riha, F. Liao, and J.-F. Stoltz, "The effect of rouleaux formation on blood coagulationmanuscript presented at the symposium on cellular aggregation and adhesion held at the 21st french congress on biomechanics and the 9th french congress on biorheology, september 1996. organized by prof. dr. j.-f. stoltz.," *Clinical hemorheology and microcirculation*, vol. 17, no. 4, pp. 341–346, 1997.

[175] H. Lim, J. Nam, S. Xue, and S. Shin, "Measurement of blood coagulation with considering rbc aggregation through a microchip-based light transmission aggregometer," *Clinical hemorheology and microcirculation*, vol. 47, no. 3, pp. 211–218, 2011.

[176] K.-H. Nam, E. Yeom, H. Ha, and S. J. Lee, "Simultaneous measurement of red blood cell aggregation and whole blood coagulation using high-frequency ultrasound," *Ultrasound in medicine & biology*, vol. 38, no. 3, pp. 468–475, 2012.

[177] D. Sakota, R. Kosaka, M. Nishida, and O. Maruyama, "Optical aggregometry of red blood cells associated with the blood-clotting reaction in extracorporeal circulation support," *Journal of Artificial Organs*, vol. 19, no. 3, pp. 241–248, 2016.

[178] V. Tutwiler, R. I. Litvinov, A. P. Lozhkin, A. D. Peshkova, T. Lebedeva, F. I. Ataullakhanov, K. L. Spiller, D. B. Cines, and J. W. Weisel, "Kinetics and mechanics of clot contraction are governed by the molecular and cellular composition of the blood," *Blood*, vol. 127, no. 1, pp. 149–159, 2016.

[179] W. A. Lam, O. Chaudhuri, A. Crow, K. D. Webster, A. Kita, J. Huang, D. A. Fletcher, *et al.*, "Mechanics and contraction dynamics of single platelets and implications for clot stiffening," *Nature materials*, vol. 10, no. 1, p. 61, 2011.

[180] N. Maeda and T. Shiga, "Opposite effect of albumin on the erythrocyte aggregation induced by immunoglobulin g and fibrinogen," *Biochimica et Biophysica Acta (BBA)-Biomembranes*, vol. 855, no. 1, pp. 127–135, 1986.

[181] S. Chien and K.-M. Jan, "Red cell aggregation by macromolecules: roles of surface adsorption and electrostatic repulsion," *Journal of supramolecular structure*, vol. 1, no. 4-5, pp. 385–409, 1973.

[182] M. Hoffman, "Remodeling the blood coagulation cascade," *Journal of thrombosis and thrombolysis*, vol. 16, no. 1-2, pp. 17–20, 2003.

[183] J. L. Hood and C. S. Eby, "Evaluation of a prolonged prothrombin time," *Clinical chemistry*, vol. 54, no. 4, pp. 765–768, 2008.

[184] K. Harter, M. Levine, and S. O. Henderson, "Anticoagulation drug therapy: a review," *Western Journal of Emergency Medicine*, vol. 16, no. 1, p. 11, 2015.

[185] M. Franchini, G. M. Liumbruno, C. Bonfanti, and G. Lippi, "The evolution of anticoagulant therapy," *Blood Transfusion*, vol. 14, no. 2, p. 175, 2016.

[186] J. Hirsh, J. E. Dalen, D. R. Anderson, L. Poller, H. Bussey, J. Ansell, and D. Deykin, "Oral anticoagulants: mechanism of action, clinical effectiveness, and optimal therapeutic range," *Chest*, vol. 119, no. 1, pp. 8S–21S, 2001.

[187] D. B. Petitti, B. L. Strom, and K. L. Melmon, "Duration of warfarin anticoagulant therapy and the probabilities of recurrent thromboembolism and hemorrhage," *The American journal of medicine*, vol. 81, no. 2, pp. 255–259, 1986.

[188] C. S. Landefeld and R. J. Beyth, "Anticoagulant-related bleeding: clinical epidemiology, prediction, and prevention," *The American journal of medicine*, vol. 95, no. 3, pp. 315–328, 1993.

[189] V. Gubala, L. F. Harris, A. J. Ricco, M. X. Tan, and D. E. Williams, "Point of care diagnostics: status and future," *Analytical chemistry*, vol. 84, no. 2, pp. 487–515, 2011.

[190] C. M. Lehman, "Instrumentation for the coagulation laboratory," in *Laboratory Hemostasis*, pp. 33–43, Springer, 2015.

[191] B. Ramaswamy, Y.-T. T. Yeh, and S.-Y. Zheng, "Microfluidic device and system for point-of-care blood coagulation measurement based on electrical impedance sensing," *Sensors and Actuators B: Chemical*, vol. 180, pp. 21–27, 2013.

[192] T. Gronewold, S. Glass, E. Quandt, and M. Famulok, "Monitoring complex formation in the blood-coagulation cascade using aptamer-coated saw sensors," *Biosensors and bioelectronics*, vol. 20, no. 10, pp. 2044–2052, 2005.

[193] O. Cakmak, E. Ermek, N. Kilinc, S. Bulut, I. Baris, I. Kavakli, G. Yaralioglu, and H. Urey, "A cartridge based sensor array platform for multiple coagulation measurements from plasma," *Lab on a Chip*, vol. 15, no. 1, pp. 113–120, 2015.

[194] C.-H. Lin, C.-Y. Liu, C.-H. Shih, and C.-H. Lu, "A sample-to-result system for blood coagulation tests on a microfluidic disk analyzer," *Biomicrofluidics*, vol. 8, no. 5, p. 052105, 2014.

[195] M. M. Dudek, N. Kent, K. M. Gustafsson, T. L. Lindahl, and A. J. Killard, "Fluorescence-based blood coagulation assay device for measuring activated partial thromboplastin time," *Analytical chemistry*, vol. 83, no. 1, pp. 319–328, 2010.

[196] G. M. Whitesides, "The origins and the future of microfluidics," *Nature*, vol. 442, no. 7101, p. 368, 2006.

[197] C. Zhou, H. Zhang, Z. Li, and W. Wang, "Chemistry pumps: a review of chemically powered micropumps," *Lab on a Chip*, vol. 16, no. 10, pp. 1797–1811, 2016.

[198] T. R. Kline, W. F. Paxton, Y. Wang, D. Velegol, T. E. Mallouk, and A. Sen, "Catalytic micropumps: microscopic convective fluid flow and pattern formation," *Journal of the American Chemical Society*, vol. 127, no. 49, pp. 17150–17151, 2005.

[199] A. A. Farniya, M. J. Esplandiu, D. Reguera, and A. Bachtold, "Imaging the proton concentration and mapping the spatial distribution of the electric

field of catalytic micropumps," *Physical review letters*, vol. 111, no. 16, p. 168301, 2013.

[200] J. P. Esquivel, M. Castellarnau, T. Senn, B. Löchel, J. Samitier, and N. Sabaté, "Fuel cell-powered microfluidic platform for lab-on-a-chip applications," *Lab on a Chip*, vol. 12, no. 1, pp. 74–79, 2012.

[201] B. T. Good, C. N. Bowman, and R. H. Davis, "An effervescent reaction micropump for portable microfluidic systems," *Lab on a Chip*, vol. 6, no. 5, pp. 659–666, 2006.

[202] C. Schubert, M. C. Van Langeveld, and L. A. Donoso, "Innovations in 3d printing: a 3d overview from optics to organs," *British Journal of Ophthalmology*, vol. 98, no. 2, pp. 159–161, 2014.

[203] M. Ranucci, T. Laddomada, M. Ranucci, and E. Baryshnikova, "Blood viscosity during coagulation at different shear rates," *Physiological reports*, vol. 2, no. 7, 2014.

[204] E. Yeom, J. H. Park, Y. J. Kang, and S. J. Lee, "Microfluidics for simultaneous quantification of platelet adhesion and blood viscosity," *Scientific reports*, vol. 6, p. 24994, 2016.

Appendix A

Estimating Relaxation Time for Suspending Mediums

M_W: Molecular weight; N_A: Avagadro's constant; k_B: Boltzmann's constant; T: Absolute temperature; η_s: Solvent viscosity; $[\eta]$: Intrinsic viscosity; c^*: Polymer overlap concentration; c: Polymer concentration; λ_{Zimm}: Estimate Zimm relaxation time; λ_{eff}: Estimate effective relaxation time; F: Front factor

$$[\eta] = 0.072 \cdot {M_W}^{0.65} \tag{A.1}$$

$$[\eta]_{600kDa} = 0.072 \cdot 600000^{0.65} = 410 \ \frac{cm^3}{g} = 0.41 \ \frac{m^3}{kg} \tag{A.2}$$

$$c^* = \frac{0.77}{[\eta]} \tag{A.3}$$

$$c^* = \frac{0.77}{0.41} = 1.877 \ \frac{kg}{m^3} \tag{A.4}$$

$$\lambda_{Zimm} = \frac{[\eta] \cdot M_W \cdot \eta_s}{N_A \cdot k_B \cdot T} \tag{A.5}$$

$$\lambda_{Zimm} = \frac{0.41[\frac{m^3}{kg}]\cdot 600[\frac{kg}{m}]\cdot 8.9\cdot 10^{-4}[Pa\cdot s]}{6.022\cdot 10^{23}[\frac{1}{mol}]\cdot 1.3806\cdot 10^{-23}[\frac{kg\cdot m^2}{s^2\cdot K}]\cdot 298[K]} = 0.41\ \ ms \tag{A.6}$$

$$\lambda_{eff} = 18\cdot\lambda_{Zimm}\cdot(\frac{c}{c^*})^{0.65} \tag{A.7}$$

$$\lambda_{eff} = 18\cdot 0.041[ms]\cdot(\frac{c[\frac{kg}{m^3}]}{1.877[\frac{kg}{m^3}]})^{0.65} \tag{A.8}$$

Appendix B

Publication List

All license agreements between Ziya Isiksacan and the License Suppliers are made by means of Copyright Clearance Center.

1. Z. Isiksacan, M. T. Guler, B. Aydogdu, I. Bilican, and C. Elbuken, Rapid fabrication of microlfuidic pdms devices from reusable pdms molds using laser ablation, Journal of Micromechanics and Microengineering, vol. 26, no. 3, p. 035008, 2016.

2. Z. Isiksacan, O. Erel, and C. Elbuken, A portable microfluidic system for rapid measurement of the erythrocyte sedimentation rate, Lab on a Chip, vol. 16, no. 24, pp. 4682-4690, 2016.

3. Z. Isiksacan, M. Asghari, and C. Elbuken, A microfluidic erythrocyte sedimentation rate analyzer using rouleaux formation kinetics, Microfluidics and Nanofluidics, vol. 21, no. 3, p. 44, 2017.

4. Z. Isiksacan, M. T. Guler, A. Kalantarifard, M. Asghari, and C. Elbuken, Lab-on-a-chip platforms for disease detection and diagnosis, Biosensors and Nanotechnology: Applications in Health Care Diagnostics, pp. 155-181, 2018.

5. M. T. Guler, Z. Isiksacan, M. Serhatlioglu, and C. Elbuken, Self-powered

disposable prothrombin time measurement device with an integrated efervescent pump, Sensors and Actuators B: Chemical, vol. 273, pp. 350-357, 2018.

6. Z. Isiksacan, N. Hastar, O. Erel, and C. Elbuken, An optofuidic point-of-care device for quantitative investigation of erythrocyte aggregation during coagulation, Sensors and Actuators A: Physical, vol. 281, pp. 24-30, 2018.

7. Z. Isiksacan, M. Serhatlioglu, and C. Elbuken, Determination of hemorheological properties using red blood cell movements in a channel under damped oscillatory flow *(submitted)*

8. M. Serhatlioglu, Z. Isiksacan, and C. Elbuken, A unifying study on electro-viscoelastic migration under simultaneously applied microfluidic pressure-driven flow and electric field *(submitted)*



Figure B.1: Lab on a Chip cover [51]